

Copyright  
by  
Anthony Lucas Bonomo  
2014

The Thesis Committee for Anthony Lucas Bonomo  
Certifies that this is the approved version of the following thesis:

On the Use of the Finite Element Method for the  
Modeling of Acoustic Scattering from One-Dimensional  
Rough Fluid-Poroelastic Interfaces

APPROVED BY

SUPERVISING COMMITTEE:

---

Mark F. Hamilton, Supervisor

---

Nicholas P. Chotiros, Co-Supervisor

**On the Use of the Finite Element Method for the  
Modeling of Acoustic Scattering from One-Dimensional  
Rough Fluid-Poroelastic Interfaces**

by

**Anthony Lucas Bonomo, B.S.**

**THESIS**

Presented to the Faculty of the Graduate School of  
The University of Texas at Austin  
in Partial Fulfillment  
of the Requirements  
for the Degree of

**MASTER OF SCIENCE IN ENGINEERING**

THE UNIVERSITY OF TEXAS AT AUSTIN

May 2014

In loving memory of Thomas W. Lucas (1938–2008)

## Acknowledgments

I'd like to acknowledge several people for their support as I completed the work that has culminated with this thesis. First, I'd like to thank my mom, dad, and brothers Tom and Greg for their everlasting love and encouragement. Next, I'd like to thank the Four Pack (Ben "Goldsbe" Goldsberry, Stephanie "Trinity" Konarski, and Justin "The Everyman" Gorhum) for making these last two years the most fun and productive of my life thus far. I'd also like to thank Rob Cullen and Dr. Matt Craun, without whom I would not be in the fortunate position of studying acoustics at UT as a SMART Scholarship recipient today. Finally I'd like to thank my advisers Dr. Nick Chotiros and Dr. Marcia Isakson for always having their doors open to answer my questions, however inane, and Dr. Mark Hamilton for masterfully teaching me all I know about the ways of acoustics.

# **On the Use of the Finite Element Method for the Modeling of Acoustic Scattering from One-Dimensional Rough Fluid-Poroelastic Interfaces**

Anthony Lucas Bonomo, M.S.E.  
The University of Texas at Austin, 2014

Supervisors: Mark F. Hamilton  
Nicholas P. Chotiros

A poroelastic finite element formulation originally derived for modeling porous absorbing material in air is adapted to the problem of acoustic scattering from a poroelastic seafloor with a one-dimensional randomly rough interface. The developed formulation is verified through calculation of the plane wave reflection coefficient for the case of a flat surface and comparison with the well known analytical solution. The scattering strengths are then obtained for two different sets of material properties and roughness parameters using a Monte Carlo approach. These numerical results are compared with those given by three analytic scattering models—perturbation theory, the Kirchhoff approximation, and the small-slope approximation—and from those calculated using two finite element formulations where the sediment is modeled as an acoustic fluid.

# Table of Contents

<b>Acknowledgments</b>	<b>v</b>
<b>Abstract</b>	<b>vi</b>
<b>List of Tables</b>	<b>x</b>
<b>List of Figures</b>	<b>xi</b>
<b>Chapter 1. Introduction</b>	<b>1</b>
1.1 Research Questions . . . . .	3
1.2 Model Problem . . . . .	4
1.3 Organization . . . . .	5
<b>Chapter 2. Background</b>	<b>7</b>
2.1 Poroelasticity . . . . .	7
2.1.1 Biot Theory . . . . .	8
2.1.2 Beyond Biot . . . . .	9
2.1.3 Experimental Evidence . . . . .	18
2.1.4 Extensions to Biot Theory . . . . .	23
2.2 Roughness Scattering . . . . .	27
2.2.1 Analytic Scattering Models . . . . .	27
2.2.2 Scattering from the Seafloor (Theory) . . . . .	32
2.2.3 Scattering from the Seafloor (Model/Data Comparisons)	36
2.3 The Combined Problem . . . . .	40
2.3.1 Subcritical Penetration . . . . .	40
2.3.2 Theory . . . . .	42
2.3.3 Model/Data Comparisons . . . . .	45
2.4 The Finite Element Method . . . . .	49
2.4.1 Application to Poroelastic Media . . . . .	49
2.4.2 Application to Roughness Scattering . . . . .	51

<b>Chapter 3. Equations of Motion</b>	<b>55</b>
3.1 Poroelasticity Equations . . . . .	55
3.2 Weak Formulations . . . . .	61
3.3 Poroelastic-Acoustic Coupling Conditions . . . . .	63
<b>Chapter 4. Finite Element Implementation</b>	<b>65</b>
4.1 Finite Element Formulation . . . . .	65
4.2 Modeling Considerations . . . . .	70
4.2.1 Rough Surface Generation . . . . .	70
4.2.2 Perfectly Matched Layers . . . . .	72
4.2.3 Incident Field . . . . .	74
4.2.4 Mesh Criteria . . . . .	75
4.2.5 Scattering Strength Calculation . . . . .	76
<b>Chapter 5. Model Verification and Convergence</b>	<b>78</b>
5.1 Absolute Error Study (Flat Surface) . . . . .	78
5.2 Relative Error Study (Rough Surface) . . . . .	83
<b>Chapter 6. Numerical Results</b>	<b>88</b>
6.1 Study 1: Following Yang et al. (2002) . . . . .	89
6.1.1 Comparison with Analytic Scattering Models . . . . .	89
6.1.2 Comparison with FEM Fluid Models . . . . .	98
6.2 Study 2: Following Williams et al. (2001) . . . . .	106
6.2.1 Comparison with Analytic Scattering Models . . . . .	109
6.2.2 Comparison with FEM Fluid Models . . . . .	114
<b>Chapter 7. Conclusions and Future Work</b>	<b>120</b>
7.1 Conclusions . . . . .	120
7.2 Future Work . . . . .	128
<b>Appendices</b>	<b>130</b>
<b>Appendix A. Analytical Reflection Coefficient Calculation</b>	<b>131</b>



<b>Appendix B. Analytic Scattering Models</b>	<b>135</b>
B.1 Perturbation Theory . . . . .	135
B.2 Kirchhoff Approximation . . . . .	136
B.3 Small-Slope Approximation . . . . .	136
<b>Appendix C. FEM Fluid Models</b>	<b>138</b>
C.1 Simple Fluid Model . . . . .	138
C.2 EDFM . . . . .	139
<b>Appendix D. COMSOL Implementation</b>	<b>141</b>
<b>Bibliography</b>	<b>143</b>
<b>Vita</b>	<b>171</b>

## List of Tables

5.1	Material properties used for absolute error study . . . . .	79
5.2	Material properties used for relative error study . . . . .	85
5.3	Roughness parameters used for relative error study . . . . .	85
6.1	Material properties following [11] . . . . .	90
6.2	Roughness parameters following [11] . . . . .	90
6.3	Fluid model parameters for study 1 . . . . .	99
6.4	Material properties following [10] . . . . .	108
6.5	Roughness parameters adapted from [10] . . . . .	108
6.6	Fluid model parameters for study 2 . . . . .	114
7.1	Roughness parameters and analytic models that provided the best fit with the FEM monostatic scattering results for those parameters. . . . .	124
7.2	Roughness parameters and analytic models that provided the best fit with the FEM bistatic scattering results for those parameters. . . . .	125

## List of Figures

1.1	Scattering geometry. . . . .	5
2.1	Illustration of the three cases of pore alignment described in [31]. The open pore case is depicted in (a). The intermediate case is depicted in (b). The closed pore case is depicted in (c). . . . .	12
4.1	Model geometry (aspect ratio not preserved). . . . .	66
5.1	Comparison of the analytical and finite element reflection loss calculations for finite element meshes of varying element size. . . . .	81
5.2	Comparison of the analytical and finite element reflection coefficient phase calculations for finite element meshes of varying element size. . . . .	82
5.3	Absolute difference of analytical and finite element reflection loss calculations for finite element meshes of varying element size. . . . .	84
5.4	Geometry of model used for relative error study. . . . .	86
5.5	Relative SPL difference at five points located on the rough surface for increasing mesh refinement. . . . .	87
6.1	Comparison of finite element (FEM) monostatic scattering results with perturbation theory (PT), the Kirchhoff approximation (KA), and the small-slope approximation (SSA) for the following parameters: $f = 100$ Hz, $w_1 = 6.3662 \times 10^{-8}$ cm $^{3-\gamma_1}$ , $\gamma_1 = 4$ , $K_0 = 0.001$ cm $^{-1}$ ( $k_a h = 0.04$ ). . . . .	91
6.2	Comparison of finite element (FEM) monostatic scattering results with perturbation theory (PT), the Kirchhoff approximation (KA), and the small-slope approximation (SSA) for the following parameters: $f = 100$ Hz, $w_1 = 6.3662 \times 10^{-6}$ cm $^{3-\gamma_1}$ , $\gamma_1 = 4$ , $K_0 = 0.001$ cm $^{-1}$ ( $k_a h = 0.42$ ). . . . .	92
6.3	Comparison of finite element (FEM) monostatic scattering results with perturbation theory (PT), the Kirchhoff approximation (KA), and the small-slope approximation (SSA) for the following parameters: $f = 3$ kHz, $w_1 = 6.3662 \times 10^{-8}$ cm $^{3-\gamma_1}$ , $\gamma_1 = 4$ , $K_0 = 0.001$ cm $^{-1}$ ( $k_a h = 1.26$ ). . . . .	93

6.4	Comparison of finite element (FEM) monostatic scattering results with perturbation theory (PT), the Kirchhoff approximation (KA), and the small-slope approximation (SSA) for the following parameters: $f = 3$ kHz, $w_1 = 6.3662 \times 10^{-8}$ cm $^{3-\gamma_1}$ , $\gamma_1 = 4$ , $K_0 = 0.001$ cm $^{-1}$ ( $k_a h = 12.57$ ). . . . .	94
6.5	Comparison of finite element (FEM) bistatic scattering results with perturbation theory (PT), the Kirchhoff approximation (KA), and the small-slope approximation (SSA) for the following parameters: $\theta = 45^\circ$ , $f = 100$ Hz, $w_1 = 6.3662 \times 10^{-8}$ cm $^{3-\gamma_1}$ , $\gamma_1 = 4$ , $K_0 = 0.001$ cm $^{-1}$ ( $k_a h = 0.04$ ). . . . .	95
6.6	Comparison of finite element (FEM) bistatic scattering results with perturbation theory (PT), the Kirchhoff approximation (KA), and the small-slope approximation (SSA) for the following parameters: $\theta = 45^\circ$ , $f = 100$ Hz, $w_1 = 6.3662 \times 10^{-6}$ cm $^{3-\gamma_1}$ , $\gamma_1 = 4$ , $K_0 = 0.001$ cm $^{-1}$ ( $k_a h = 0.42$ ). . . . .	96
6.7	Comparison of finite element (FEM) bistatic scattering results with perturbation theory (PT), the Kirchhoff approximation (KA), and the small-slope approximation (SSA) for the following parameters: $\theta = 45^\circ$ , $f = 3$ kHz, $w_1 = 6.3662 \times 10^{-8}$ cm $^{3-\gamma_1}$ , $\gamma_1 = 4$ , $K_0 = 0.001$ cm $^{-1}$ ( $k_a h = 1.26$ ). . . . .	97
6.8	Comparison of finite element (FEM) bistatic scattering results with perturbation theory (PT), the Kirchhoff approximation (KA), and the small-slope approximation (SSA) for the following parameters: $\theta = 45^\circ$ , $f = 3$ kHz, $w_1 = 6.3662 \times 10^{-6}$ cm $^{3-\gamma_1}$ , $\gamma_1 = 4$ , $K_0 = 0.001$ cm $^{-1}$ ( $k_a h = 12.57$ ). . . . .	98
6.9	Comparison of full poroelastic finite element (FEM poro) monostatic scattering results with those of finite element models that consider the sediment to be an effective density fluid (FEM EDFM) and a simple fluid (FEM fluid) for the following parameters: $f = 100$ Hz, $w_1 = 6.3662 \times 10^{-8}$ cm $^{3-\gamma_1}$ , $\gamma_1 = 4$ , $K_0 = 0.001$ cm $^{-1}$ ( $k_a h = 0.04$ ). . . . .	100
6.10	Comparison of full poroelastic finite element (FEM poro) monostatic scattering results with those of finite element models that consider the sediment to be an effective density fluid (FEM EDFM) and a simple fluid (FEM fluid) for the following parameters: $f = 100$ Hz, $w_1 = 6.3662 \times 10^{-6}$ cm $^{3-\gamma_1}$ , $\gamma_1 = 4$ , $K_0 = 0.001$ cm $^{-1}$ ( $k_a h = 0.42$ ). . . . .	101

6.11	Comparison of full poroelastic finite element (FEM poro) monostatic scattering results with those of finite element models that consider the sediment to be an effective density fluid (FEM EDFM) and a simple fluid (FEM fluid) for the following parameters: $f = 3$ kHz, $w_1 = 6.3662 \times 10^{-8} \text{ cm}^{3-\gamma_1}$ , $\gamma_1 = 4$ , $K_0 = 0.001 \text{ cm}^{-1}$ ( $k_a h = 1.26$ ). . . . .	102
6.12	Comparison of full poroelastic finite element (FEM poro) monostatic scattering results with those of finite element models that consider the sediment to be an effective density fluid (FEM EDFM) and a simple fluid (FEM fluid) for the following parameters: $f = 3$ kHz, $w_1 = 6.3662 \times 10^{-6} \text{ cm}^{3-\gamma_1}$ , $\gamma_1 = 4$ , $K_0 = 0.001 \text{ cm}^{-1}$ ( $k_a h = 12.57$ ). . . . .	103
6.13	Comparison of full poroelastic finite element (FEM poro) bistatic scattering results with those of finite element models that consider the sediment to be an effective density fluid (FEM EDFM) and a simple fluid (FEM fluid) for the following parameters: $\theta = 45^\circ$ , $f = 100$ Hz, $w_1 = 6.3662 \times 10^{-8} \text{ cm}^{3-\gamma_1}$ , $\gamma_1 = 4$ , $K_0 = 0.001 \text{ cm}^{-1}$ ( $k_a h = 0.04$ ). . . . .	104
6.14	Comparison of full poroelastic finite element (FEM poro) bistatic scattering results with those of finite element models that consider the sediment to be an effective density fluid (FEM EDFM) and a simple fluid (FEM fluid) for the following parameters: $\theta = 45^\circ$ , $f = 100$ Hz, $w_1 = 6.3662 \times 10^{-6} \text{ cm}^{3-\gamma_1}$ , $\gamma_1 = 4$ , $K_0 = 0.001 \text{ cm}^{-1}$ ( $k_a h = 0.42$ ). . . . .	105
6.15	Comparison of full poroelastic finite element (FEM poro) bistatic scattering results with those of finite element models that consider the sediment to be an effective density fluid (FEM EDFM) and a simple fluid (FEM fluid) for the following parameters: $\theta = 45^\circ$ , $f = 3$ kHz, $w_1 = 6.3662 \times 10^{-8} \text{ cm}^{3-\gamma_1}$ , $\gamma_1 = 4$ , $K_0 = 0.001 \text{ cm}^{-1}$ ( $k_a h = 1.26$ ). . . . .	106
6.16	Comparison of full poroelastic finite element (FEM poro) bistatic scattering results with those of finite element models that consider the sediment to be an effective density fluid (FEM EDFM) and a simple fluid (FEM fluid) for the following parameters: $\theta = 45^\circ$ , $f = 3$ kHz, $w_1 = 6.3662 \times 10^{-6} \text{ cm}^{3-\gamma_1}$ , $\gamma_1 = 4$ , $K_0 = 0.001 \text{ cm}^{-1}$ ( $k_a h = 12.57$ ). . . . .	107
6.17	Comparison of finite element (FEM) monostatic scattering results with perturbation theory (PT), the Kirchhoff approximation (KA), and the small-slope approximation (SSA) for the following parameters: $f = 100$ Hz, $w_1 = 0.0078 \text{ cm}^{3-\gamma_1}$ , $\gamma_1 = 2.05$ , $K_0 = 0.008 \text{ cm}^{-1}$ ( $k_a h = 0.008$ ). . . . .	109

6.18	Comparison of finite element (FEM) monostatic scattering results with perturbation theory (PT), the Kirchhoff approximation (KA), and the small-slope approximation (SSA) for the following parameters: $f = 1$ kHz, $w_1 = 0.0078$ cm <sup>3-<math>\gamma_1</math></sup> , $\gamma_1 = 2.05$ , $K_0 = 0.008$ cm <sup>-1</sup> ( $k_a h = 0.081$ ). . . . .	110
6.19	Comparison of finite element (FEM) monostatic scattering results with perturbation theory (PT), the Kirchhoff approximation (KA), and the small-slope approximation (SSA) for the following parameters: $f = 10$ kHz, $w_1 = 0.0078$ cm <sup>3-<math>\gamma_1</math></sup> , $\gamma_1 = 2.05$ , $K_0 = 0.008$ cm <sup>-1</sup> ( $k_a h = 0.813$ ). . . . .	111
6.20	Comparison of finite element (FEM) monostatic scattering results with perturbation theory (PT), the Kirchhoff approximation (KA), and the small-slope approximation (SSA) for the following parameters: $f = 100$ kHz, $w_1 = 0.0078$ cm <sup>3-<math>\gamma_1</math></sup> , $\gamma_1 = 2.05$ , $K_0 = 0.008$ cm <sup>-1</sup> ( $k_a h = 8.134$ ). . . . .	112
6.21	Comparison of finite element (FEM) monostatic scattering results with perturbation theory (PT), the Kirchhoff approximation (KA), and the small-slope approximation (SSA) for the following parameters: $f = 12.295$ kHz, $w_1 = 0.0078$ cm <sup>3-<math>\gamma_1</math></sup> , $\gamma_1 = 2.05$ , $K_0 = 0.008$ cm <sup>-1</sup> ( $k_a h = 1$ ). . . . .	113
6.22	Comparison of full poroelastic finite element (FEM poro) monostatic scattering results with those of finite element models that consider the sediment to be an effective density fluid (FEM EDFM) and a simple fluid (FEM fluid) for the following parameters: $f = 100$ Hz, $w_1 = 0.0078$ cm <sup>3-<math>\gamma_1</math></sup> , $\gamma_1 = 2.05$ , $K_0 = 0.008$ cm <sup>-1</sup> ( $k_a h = 0.008$ ). . . . .	115
6.23	Comparison of full poroelastic finite element (FEM poro) monostatic scattering results with those of finite element models that consider the sediment to be an effective density fluid (FEM EDFM) and a simple fluid (FEM fluid) for the following parameters: $f = 1$ kHz, $w_1 = 0.0078$ cm <sup>3-<math>\gamma_1</math></sup> , $\gamma_1 = 2.05$ , $K_0 = 0.008$ cm <sup>-1</sup> ( $k_a h = 0.081$ ). . . . .	116
6.24	Comparison of full poroelastic finite element (FEM poro) monostatic scattering results with those of finite element models that consider the sediment to be an effective density fluid (FEM EDFM) and a simple fluid (FEM fluid) for the following parameters: $f = 10$ kHz, $w_1 = 0.0078$ cm <sup>3-<math>\gamma_1</math></sup> , $\gamma_1 = 2.05$ , $K_0 = 0.008$ cm <sup>-1</sup> ( $k_a h = 0.813$ ). . . . .	117

6.25 Comparison of full poroelastic finite element (FEM poro) mono-  
static scattering results with those of finite element models that  
consider the sediment to be an effective density fluid (FEM  
EDFM) and a simple fluid (FEM fluid) for the following param-  
eters:  $f = 100$  kHz,  $w_1 = 0.0078$  cm<sup>3- $\gamma_1$</sup> ,  $\gamma_1 = 2.05$ ,  $K_0 = 0.008$   
cm<sup>-1</sup> ( $k_a h = 8.134$ ) . . . . . 118

# Chapter 1

## Introduction

The interaction of acoustic waves with the ocean floor is a relevant and important topic in many fields of scientific research, including marine seismology, petroleum geophysics, and underwater acoustics [1]. In naval applications, acoustic scattering by the seafloor has long been recognized as an important source of interference with sonar systems; this interference is particularly prominent in shallow water environments [2]. Since more and more naval applications are focusing on littoral environments, accurate models that describe both the physics of the sediment and the interaction of acoustic waves with the bottom are of present necessity.

The acoustic behavior of sediments has been studied extensively. The earliest models assumed sediments behaved like fluids. Since sediments generally can support shear stresses, the assumptions made when using fluid models are tenuous at best and have been replaced with more robust models, such as those that model the sediment as an elastic or viscoelastic material [2]. However, it has recently been shown that the best fit with experimental reflection and backscattering data occurs when the sediment is assumed to behave as a poroelastic medium governed by the Biot model [3,4]. Even an effective



density fluid model (EDFM) developed in [5] that approximates a poroelastic medium does better than other models at matching measured reflection and backscattering data [4, 6]. Experimental results also indicate that the variation of sound speed with frequency is modeled fairly well by Biot theory [7]. For this reason, it will be assumed in this work that the sediments considered behave as poroelastic media.

Biot theory has also seen widespread application in the modeling of porous materials used for sound insulation and noise control in air. To meet this need, finite element models for sound absorbing materials assumed to be poroelastic have been developed [8]. Despite their robustness, these finite element formulations are rarely, if ever, applied to problems dealing with underwater acoustic scattering from the seabed; it is the primary goal of the present work to do just this.

In addition to the choice of sediment model employed, effects on the scattered field due to seafloor roughness are of particular importance, especially at higher acoustic frequencies, where seafloor roughness can be a dominant contributor [2]. Scattering by interface roughness is also postulated to be the dominant mechanism for subcritical penetration into sediments [9]. Therefore, roughness effects cannot be neglected if one hopes to model the acoustic interaction with the seafloor accurately. Scattering problems are typically studied using theoretical models that make various assumptions in approximating the Helmholtz-Kirchhoff integral. The three most common of these methods are perturbation theory, the Kirchhoff approximation, and the small-

slope approximation. Recently, perturbation theory and the small-slope approximation have been extended to scattering from rough poroelastic surfaces [10, 11]. Neither of these models as applied to scattering from poroelastic interfaces has been vetted against exact solutions so their validity is yet unknown. In this work, the finite element method, which converges to the exact solution provided the discretization of elements is sufficiently fine, will be used to assess the accuracy and validity of perturbation theory, the Kirchhoff approximation, and the small-slope approximation in modeling scattering from poroelastic surfaces. The finite element method is also capable of modeling high roughness cases where the aforementioned approximate models fail. Therefore, in addition to vetting the analytic models, the poroelastic finite element formulation will enable the modeling of scattering problems that have thus far been out of reach.

## 1.1 Research Questions

The purpose of this thesis is to study the acoustic scattering from one-dimensional rough poroelastic interfaces using the finite element method and to address the following research questions:

1. How should the poroelastic finite element formulations be adapted to the problem of acoustic scattering from the seabed?
2. What are the effects of roughness on the acoustic scattering from poroelastic interfaces?

3. Do the three most widely used analytic scattering models—perturbation theory, the Kirchhoff approximation, and the small-slope approximation—perform well when applied to scattering from rough poroelastic surfaces, and, if so, what are their regions of validity?
4. How does the scattering from media assumed to follow the effective density fluid model compare to the results obtained for the full poroelastic formulation?

## 1.2 Model Problem

In order to address the research questions enumerated above, a simple two half-space scattering problem will be adapted for the present work. The geometry of the problem is illustrated in Figure 1.1. As shown in the figure, a plane wave is obliquely incident on a rough interface separating two semi-infinite half-spaces. The upper half-space consists of a fluid while the lower half-space is assumed to be a poroelastic medium consisting of two components: a solid elastic frame and an interstitial fluid. It is also assumed that the fluid of the upper medium is the same fluid as the interstitial fluid of the lower medium. Scattered and transmitted waves result when the incident plane wave impinges on the rough interface. Following Biot theory, the transmitted energy is distributed into three different waves—two compressional waves (denoted as the “fast” and “slow” waves) and a shear wave [11].

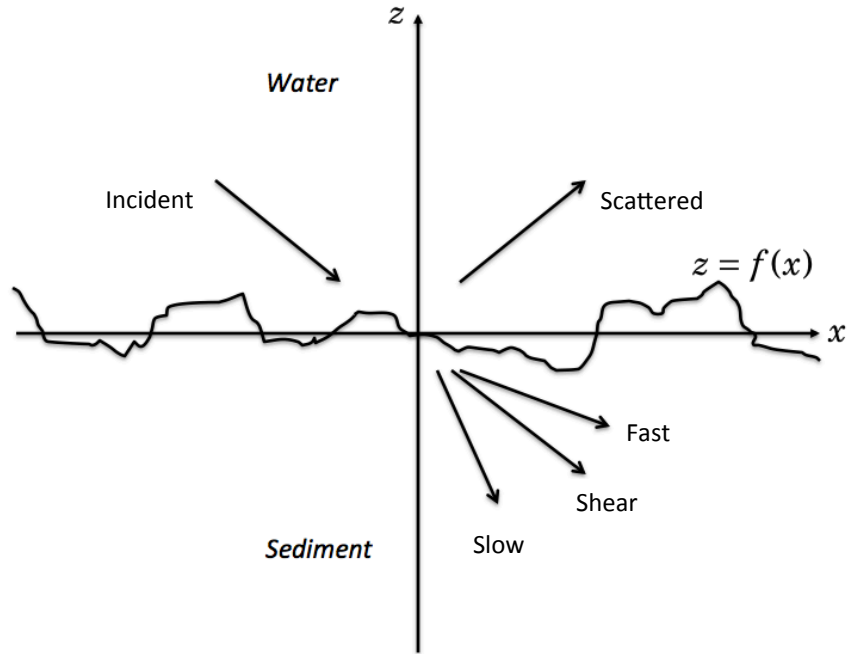


Figure 1.1: Scattering geometry.

### 1.3 Organization

This thesis has the following organization. Chapter 2 provides a review of the literature necessary to have an appropriate grasp of the context of the present work. Chapter 3 is devoted to discussing the equations of motion that govern poroelastic media and develops the form of these equations that will be used in the finite element implementation. Chapter 4 considers how the existing poroelastic finite element formulations can be adapted for the present work; this chapter also discusses considerations that need to be made when

truncating the scattering geometry of Figure 1.1 to a finite computational domain. Chapter 5 outlines the results of model verification and convergence studies. Chapter 6 presents the main numerical results. Finally, Chapter 7 gives conclusions and recommendations for future work.

# Chapter 2

## Background

The aim of this chapter is to review the literature relevant to the present work and to provide necessary background and context. The first section discusses the development of the theory of poroelasticity and its applications. The second section deals with the considerations needed to study acoustic scattering from rough surfaces and the models most frequently used. The third section discusses the literature dealing with the combined problem of scattering from rough poroelastic surfaces. Finally, a section is devoted to the finite element method.

### 2.1 Poroelasticity

This section is intended to provide background on the theory of poroelasticity as developed by Biot and worked on by others. First, Biot's foundational work on the subject is discussed. Next, the contributions of other researchers to theoretical development relevant to the present work is dealt with. After that, the experimental evidence confirming the utility of Biot theory is summarized. Finally, extensions and alternatives to Biot theory are briefly described.

### 2.1.1 Biot Theory

Although the study of porous media can be traced back earlier to the work of Fillunger in 1913 and von Terzaghi in 1923, the theory of porous media most widely accepted today was created principally—and almost exclusively—by Maurice Biot in a series of classic papers that introduce what is now known as the theory of poroelasticity or Biot theory [12, 13]. Biot theory models the porous material as a skeletal elastic frame coupled to a fluid which completely fills its pores; in total, the theory describes the physics governing the static and dynamic response of such materials [14]. Of particular interest to the present work are the equations of wave propagation given by the theory.

The foundation of poroelasticity relies heavily on Biot’s early work dealing with consolidation, the process through which soil under load settles gradually at a variable rate. In [15], Biot formulates the field equations describing consolidation under the assumption of isotropy, which give the stresses and displacements of an elastic matrix with voids filled with a viscous fluid obeying Darcy’s law [12]. Biot follows with [16–18], which show specific applications of the methods given in [15]. The formulation of [15] is generalized to the case of anisotropy in [19]. Returning to isotropy, general solutions to the equations of elasticity and consolidation for a poroelastic material are given by Biot in [20].

Perhaps the most pivotal papers in the development of the Biot theory of porous media are [21] and [22]. It is in these two papers where the equations governing elastic wave propagation in a poroelastic solid are developed. In [21],

the analysis is restricted to the low frequency range where the Poiseuille flow assumption is valid while [22] deals with the extension to higher frequencies. These two papers are also where the existence of a second compressional wave with slower sound speed and high attenuation, now known as the “slow wave,” is first predicted.

Biot’s remaining papers on the subject serve to further polish and extend his theory. In [23], the formulation of [21] and [22] are extended to the case of anisotropic solids with viscoelastic properties [12]. In a paper co-authored by Willis, Biot discusses measurement methods to determine the elastic coefficients needed for the theory and the physical interpretation of these coefficients [24]. This paper is also where the so-called Biot-Willis coefficient and Biot modulus are codified. The theory is further generalized and its nomenclature made more concise and systematic in [25] and [26]. While he would continue to develop his theory for over a decade past the publication of [26], these two papers are generally considered the culmination of Biot’s development of the theory of poroelasticity.

### **2.1.2 Beyond Biot**

While Biot almost single-handedly formulated the theory of poroelasticity that bears his name, many other researchers have since contributed to the study of poroelastic materials, both in further development of Biot’s theory and in the theory’s application. Perhaps the most important contributor to the development of the theory of poroelasticity after Biot in the field of



geophysics and sediment acoustics was Robert Stoll. Stoll's first contribution is [27], in which Stoll and Bryan study the wave attenuation predicted by Biot theory and extend the theory to include losses due to the inelasticity of the frame by allowing the bulk and shear moduli of the frame to be complex. This article also explicitly puts forth the thirteen parameters required as inputs to the Biot model and shows the effects on the expected attenuation when several of these parameters are varied individually. These thirteen parameters are as follows:

1. bulk modulus of grains
2. bulk modulus of fluid
3. mass density of grains
4. mass density of fluid
5. bulk modulus of frame
6. log decrement for bulk vibrations of frame
7. shear modulus of skeletal frame
8. log decrement for shear vibrations of frame
9. viscosity of fluid
10. porosity
11. permeability
12. structure constant (or tortuosity)
13. pore-size parameter

In [28], Stoll presents what is perhaps the most succinct derivation of Biot's equations, further discusses the relationship between the input parameters,

computes the attenuation for a number of measured parameter sets, and compares these calculations with the limited measured data that was available to him. Applications of the theory described by [27] and [28] are discussed in [29]; this paper is also where Stoll gives the sand parameter set most frequently employed in the subsequent literature on the subject. In [30], his most cited paper and one of the seminal articles dealing with the theory of poroelasticity, Stoll and Kan study the reflection and refraction of acoustic plane waves impinging on a fluid-poroelastic interface. This work discusses the application of what is now referred to as the “open pore” interface coupling conditions at length, numerically calculates the reflection coefficients for two parameter sets, and studies how the reflection coefficients change when the permeability, frequency, and angle of incidence are varied. Stoll’s theoretical work on the subject culminates with [14], his monograph that includes chapters on the derivation of Biot’s equations, parametric studies, the physics of idealized granular media, laboratory measurements and how these measurements can be used to determine the input parameters, and how the theory can be applied to geoacoustic models. Finally, an appendix expands upon the work of [30] and explicitly outlines how the fluid-poroelastic reflection coefficients can be evaluated analytically.

In addition to Stoll, many other researchers have contributed to the theoretical development and application of poroelastic theory. One topic that has received particular attention is the derivation of the conditions needed to ensure proper coupling of two poroelastic media, a fluid and a poroelastic

medium, and a poroelastic medium and an elastic solid. In a seminal paper [31], Deresiewicz and Skalak derive the necessary conditions to ensure proper coupling of two poroelastic media for three cases. The first case is the so-called “open pore” case, where all the pores of the two media are completely connected. The second case is the situation where some pores are properly aligned and others are not. The third case is the so-called “closed pore” case, where none of the pores are aligned. Fig. 2.1 reproduced from [31] illustrates these three cases. In addition, Deresiewicz and Skalak also derive the conditions required to properly couple a poroelastic medium to an elastic solid and a fluid.

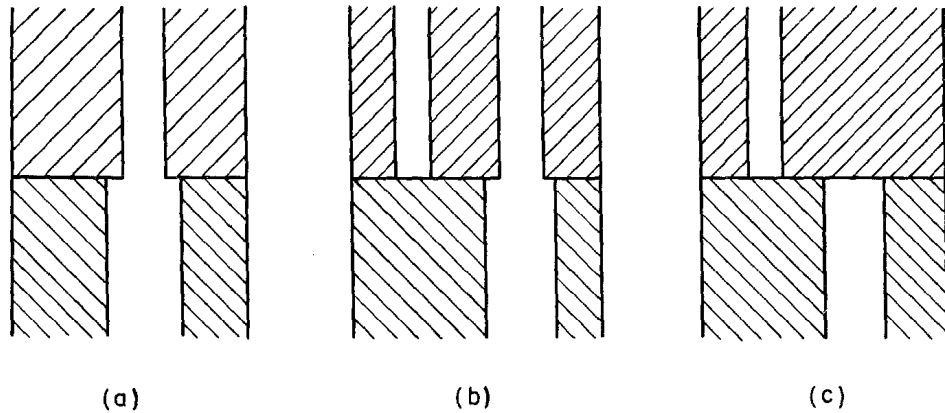


Figure 2.1: Illustration of the three cases of pore alignment described in [31]. The open pore case is depicted in (a). The intermediate case is depicted in (b). The closed pore case is depicted in (c).

The open pore coupling conditions for two distinct porous media are independently derived by Lovera in [32]. Here the conditions are expressed purely in terms of the stress tensors and displacement vectors allowing for ease

of application to contact surfaces of arbitrary shape and to anisotropic media. Lovera also uses the asymptotic behavior of these conditions to independently derive the coupling conditions for poroelastic-elastic and poroelastic-fluid interfaces.

Despite the widespread use of the coupling conditions for two poroelastic media given by [31], their validity is challenged by de la Cruz and Spanos in [33]. This controversy is addressed by Gurevich and Schoenberg in [34], where it is shown that only the conditions given in [31] for the open pore case are valid and that the conditions for the remaining cases do not properly satisfy Biot's equations at the interface. However, Gurevich and Schoenberg show that these cases can be properly modeled by allowing for the existence of an intermediate thin layer with small permeability proportional to its thickness. In [35], Sharma derives a set of coupling conditions for the case of partially connected pores at a welded poroelastic-poroelastic interface. Sharma also considers the case of loose contact at the interface.

A related problem that has received considerable attention is the determination of the reflection and transmission coefficients of a wave (usually assumed planar) incident on a poroelastic surface. Early treatment of the subject is given by Deresiewicz in a series of classic papers. In [36], Deresiewicz considers the propagation of plane waves in a non-dissipative poroelastic medium and their reflection from a plane, stress-free boundary. It is determined that, in general, reflection from the free surface gives rise to waves of all three types supported by poroelastic media regardless of which type is incident. It is also

concluded in [36] that “while there always exists a critical angle of incidence of the [slow] and [shear] waves beyond which the reflected [fast] wave is localized as a surface motion, there may occur, in addition, critical angles for total reflection of either the [shear] or the [slow] wave, their existence depending on material properties.” Deresiewicz and Rice expand upon this work in [37], where the general case including dissipation is considered. In addition to the angles of reflection and reflection coefficients, expressions are found for the phase velocities and attenuation coefficients of the reflected waves. It is determined that the reflected waves are both dispersive and dissipative and that critical reflection of the compressional waves does not occur for an incident shear wave. In [38], Deresiewicz and Rice consider the problem of wave transmission between two poroelastic media for the case of normal incidence and develop expressions for the transmission coefficients and phase shifts that result for both an incident fast wave and an incident shear wave. Although no shear waves result when a fast wave is normally incident on the boundary, it is found that a fast wave can generate a slow wave and vice versa. One final paper by Deresiewicz relevant to the problem of reflection and transmission is [39] coauthored by Levy. Here reflection and transmission coefficients are calculated in terms of recursion relations for fast and shear waves normally incident on a system of poroelastic layers of arbitrary number terminating in poroelastic half-spaces.

Since the work of Deresiewicz, considerably more research has been done to address the problem of reflection from and transmission through a

poroelastic boundary. In an important paper [40], Hajra and Mukhopadhyay study the reflection and refraction of elastic waves obliquely incident on an elastic-poroelastic interface and obtain expressions for the reflection and transmission coefficients for both incident compressional waves and incident shear waves. In [41], Dutta and Odé study the reflection and transmission of plane waves that occurs at the interface of two poroelastic media with the same elastic properties but distinct pore fluids and derives the reflection and transmission coefficients for this case. The paper states two important conclusions: (1) the transfer of energy at the interface into highly attenuated slow waves is the most significant loss mechanism and (2) in addition to the expected energy fluxes carried by the three waves, there is a nonzero interference flux that must be considered, especially at high frequencies. Following [40] and [41], Allard et al. expand upon [39] in [42] and use transfer matrices to calculate the input impedance and reflection and transmission coefficients for the case of waves obliquely incident upon a system of layered poroelastic media.

Following the classic paper of Stoll and Kan [30], many other researchers have considered the problem of the reflection and transmission that occurs when a plane wave impinges on a fluid-poroelastic interface. Expanding on [30], Wu, Xue, and Adler [43] use the Poynting energy flux vector to find not only the reflection coefficients but also the transmission coefficients for a plane wave obliquely incident from the fluid. Furthermore, Wu, Xue, and Adler consider the case when the incident wave originates in the poroelastic medium and compare calculations of the transmission coefficients of sound through

a fluid-poroelastic-fluid system to experiment, finding reasonable agreement. Wu, Xue, and Adler also apply the closed pore condition described in [31] to calculate the reflection and transmission coefficients and find considerable differences from the open pore case. However, these authors seem unaware of the work cited above discrediting the physical validity of the closed pore condition of [31] so this part of their work should be regarded with skepticism. In [44], Santos et al. analyze the effect of Biot's high-frequency correction factor on the reflection and transmission coefficients for both fluid-poroelastic and poroelastic-poroelastic interfaces and find the reflection and transmission coefficients calculated with the correction included differ significantly from those calculated without it. Albert [45] compared the plane wave transmission that occurs at an air-air-saturated poroelastic interface and a water-water-saturated poroelastic interface, finding major differences and concluding that the transmitted slow wave is far more important in the air-saturated case. In [46], Denneman et al. derive new closed-form expressions for the fluid-poroelastic reflection and transmission coefficients and compare the case of a water-water-saturated poroelastic interface to the case of a water-air-saturated poroelastic interface. This work is extended to the case of a general anisotropic poroelastic medium by Sharma in [47].

Research dealing with the coupling of poroelastic media to fluids and elastic solids and the reflection and transmission that results when a plane wave impinges upon the interfaces along which this coupling occurs remains a topic of interest to this day. Recently, Nandal and Saini have considered the

reflection and transmission at an imperfectly bonded poroelastic-cracked elastic solid interface [48] and Wang et al. derived the reflection and transmission coefficients for plane waves at a fluid-poroelastic interface with an underlying elastic solid substrate [1].

Although not fitting neatly into the topics of interface coupling or reflection and transmission, a few other papers were found to be useful to the present work and will now be discussed briefly. In [49], Berryman develops a new identification of the coefficients present in Biot's strain energy functional that depends only on the frame bulk and shear moduli, the fluid bulk modulus, and the porosity; this new identification is found to be exact for the case of fully consolidated frames. Berryman also discusses how many of the required input parameters (such as the frame parameters and the tortuosity) can be determined theoretically from quantities that are more easily known (such as the porosity and the grain parameters). In a particularly important paper [50], Yamamoto determines the acoustic normal modes of an isovelocity ocean overlying a poroelastic half-space. This paper also gives a closed form expression for the calculation of the phase speeds and attenuations of the three waves supported by a poroelastic medium. One last paper that is essential to the present work is [5], in which Williams develops an effective density fluid model to approximate the behavior of a poroelastic medium. Finally, it should be noted that, while the majority of the work discussed in this section deals with the application of Biot theory to geophysics, seismology, and sediment acoustics, much work has also been done toward using the theory to predict



the behavior of porous sound absorbing material in air; see, for instance, [51] and [52].

### 2.1.3 Experimental Evidence

Although Biot theory makes several predictions that are directly testable, experimental confirmation of the theory did not occur until over twenty years after the theory's conception. The earliest and most frequently cited experimental evidence is reported by Plona in [53]. In this work, Plona used an ultrasonic measurement technique based on mode conversion occurring at the boundary of an immersed water-saturated porous solid consisting of sintered glass spheres. Through measurement of the arrival times of the received pulses, Plona not only identified a compressional wave with sound speed much less than the normal compressional wave but directly observed the mode conversion between these two compressional waves at the boundaries. Berryman further analyzed Plona's measurements in [54] and found that the slow wave speeds predicted by Biot theory lie within 10% of the experimental values and increase when the porosity is increased, as predicted by the theory. Expanding upon the measurements put forth in [53], Johnson and Plona reported similar measurements of the wave speeds of both unconsolidated (i.e., loose) and consolidated (i.e., sintered) glass beads immersed in water [55]. In the case of the unconsolidated beads, a single compressional wave and no shear waves is observed. However, once the beads were fused into a porous medium, two distinct compressional waves (fast and slow) and a shear wave are observed. It is

interesting to note that neither of the compressional wave speeds measured for the consolidated case correspond to the wave speed measured when the beads were kept loose. It should also be noted that both measurements reported by Plona were taken under carefully controlled laboratory conditions and using broadband pulses with the rather high center frequency of 500 kHz.

In addition to the work of Plona and Johnson, a good portion of the other attempts at experimentally verifying Biot theory have dealt with slow wave observation and measurement. In [56], Nagy, Adler, and Bonner present a technique utilizing the transmission of airborne ultrasound through air-saturated porous samples to measure the phase speed and attenuation of the slow wave. Since their technique causes all the incident wave energy to either be reflected or transmitted via the slow wave, slow wave propagation is readily observed in air-saturated natural rocks at 150 kHz. Also, the slow wave speed and attenuation in a sintered glass bead sample are measured over the wide frequency range of 30 to 500 kHz and the measured data are found to agree closely with the values predicted by Biot theory.

In [57], Boyle and Chotiros describe the measurement of the speeds of waves supported by unconsolidated sand underlying a water column in a laboratory tank and report observation of a slower compressional wave when the sand is insonified at shallow grazing angles. While the researchers speculate that this slower compressional wave may be explained by Biot theory, they are unable to accurately predict a slow wave with the measured speed using the poroelastic parameters most frequently cited for sand.

One measurement set particularly relevant to the present work but not often cited is reported by Nakagawa, Soga, and Mitchell in [58]. Using very sensitive transducers, Nakagawa, Soga, and Mitchell observe the slow compressional wave in granular soils and find the measured phase speeds to agree with theoretical calculations to within less than 10%. The researchers also find the slow wave to be highly frequency dependent and have phase opposite of that of the fast and shear waves, which is consistent with theory.

Another highly pertinent paper reporting evidence of slow wave propagation is [59] by Kelder and Smeulders. Using an experimental setup similar to that used by Plona in [53], Kelder and Smeulders observe a slow wave consistent with Biot theory in water-saturated Nivelsteiner sandstone and find the measured velocity to be of the same order as reported for sintered glass beads in [53].

Relatively recently, Bouzidi and Schmitt refined the experimental procedure of Plona with a newly developed ultrasonic transmitter-receiver pair and report their findings in [60]. Again, the measured properties of the slow wave are found to be consistent with Biot theory. Bouzidi and Schmitt also conclude that models using the open pore coupling conditions best match experiment.

In addition to observation of the slow wave, other predictions made by Biot theory have been experimentally verified. In [61], Turgut and Yamamoto report the results of acoustic pulse transmission experiments in saturated beach sediments where the fast and shear wave speeds and intrinsic

attenuations are measured. The data collected show the dispersive nature of the fast wave velocities, as predicted by Biot theory. This finding demonstrates that viscous effects due to the relative motion of the pore fluid with respect to the frame is the main damping mechanism in the frequency range of 1–30 kHz. Turgut and Yamamoto also find consistency between directly measured porosity and permeability values and those predicted by Biot theory using the measured wave speeds and attenuations.

King, Marsden, and Dennis report the results of several ultrasonic measurements of the fast and shear speeds of many sandstone samples of various levels of salt water saturation in [62]. First, the researchers measured the wave speeds for many dry and fully-saturated samples and find excellent agreement with the values predicted by Biot theory. Next, they measured the wave speeds for eight of the sandstones at different saturation levels and find that the shear wave speeds follow Biot theory closely while the fast wave speeds are higher than expected. The researchers attribute this disparity of the fast wave speeds to small heterogeneities in pore size not accounted for in their calculations.

A good deal of data collected as part of the SAX99 series of field experiments conducted in the Gulf of Mexico have been offered as verification of the predictions made by Biot theory. In [63], Stoll compares compressional (fast) wave velocities measured at high and low frequencies in a uniform sand layer below the seafloor and finds a significant amount of velocity dispersion in the interval lying between these frequency extremes. Stoll attributes this dispersion to the motion of the pore fluid relative to the sediment's elastic frame as

described by Biot theory. In [7], Williams et al. analyze the sound speed and attenuation measurements made by several researchers during SAX99 spanning the extensive frequency range of 125 Hz–400 kHz. In comparing these measurements to the sound speeds and attenuations predicted by Biot theory, Williams et al. conclude that both the full Biot model and the effective density fluid model described in [5] capture the dispersion and attenuation variation for low frequencies but deviate from the measured values as frequency increases. The researchers speculate that a porous medium model that includes both random volume heterogeneity and the effects of the shearing at grain contacts may perform better. One final work related to SAX99 and relevant to experimental verification of Biot theory is [64]. In a brief letter, Ohkawa compares attenuation calculations following Biot theory to measurement and finds the two to be in excellent agreement.

Poroelastic models based on Biot theory and viscoelastic models, which are a simpler alternative frequently employed, make different predictions concerning the expected reflection coefficient of a water-sandy sediment interface. At least two studies have tried to use measured reflection loss data as a means to determine the efficacy of these two types of models. In [65], Chotiros et al. describe measurements taken of the reflection loss at normal incidence from a sandy sediment near the island of Elba, Italy and find the measured values to be inconsistent with the viscoelastic models above expected experimental error. Chotiros et al. put forth poroelastic models as an alternative since the slow wave is a loss mechanism that can account for the higher levels of reflec-

tion loss that were determined experimentally. In a related study [6], Camin and Isakson use plane wave decomposition to compute the reflection coefficients from measurements collected using a spherical source and receiver and compare these experimentally determined values to three plane wave reflection coefficient models—a viscoelastic model, the effective density fluid model from [5], and a grain shearing model based on the work of Buckingham [66]. Camin and Isakson find that the reflection coefficients predicted by the viscoelastic and grain shearing models are not within the 95% confidence interval for low frequencies and that, in general, the Biot-based effective density fluid model provides the best fit with experiment.

One final paper putting forth experimental evidence in support of Biot theory is [67] by Zhou, Zhang, and Knobles. This paper compiles and analyzes low frequency measurements taken in shallow water at various locations and finds the frequency dependence of the sound attenuation of sandy seabottoms to be nonlinear. The researchers compare these measurements of attenuation and sound speed to the values predicted by Biot theory and conclude that poroelastic models describe the sound speeds and attenuation values well.

#### **2.1.4 Extensions to Biot Theory**

Despite its success and predictive power, many researchers have worked to extend Biot theory or to introduce alternative theories governing the physics of poroelastic media. An early attempt at coming to a more general theory of porous media is made by Burridge and Keller in [68]. Starting with the

equation of linear elasticity to describe the solid frame, the linearized Navier-Stokes equations to describe the pore fluid, and the needed conditions to couple the two phases, Burridge and Keller analyze the microstructure of poroelastic media and use the two-space method of homogenization to derive general macroscopic equations of motion. The researchers find that if the medium is macroscopically uniform and the viscosity of the pore fluid is small, their equations reduce to those given by Biot theory. Their equations are also seen to reduce to those of a viscoelastic solid when the viscosity is not small and the medium is still assumed uniform. However, when the viscosity is assumed small and the medium is not uniform, Burridge and Keller find their equations to have terms not seen in either Biot’s equations or those of viscoelasticity.

One common avenue for extending Biot theory has been inclusion of the effects of the so-called “squirt-flow mechanism,” where the pore fluid squirts out of the cracks as they are deformed by passing waves. Biot-based models that include squirt flow effects are often referred to as Biot-squirt or BISQ models [69]. In [70], Dvorkin and Nur introduce a heuristic BISQ model to describe the dynamics of saturated rocks and find their model to give attenuation that is much higher than what is predicted by Biot theory. The researchers also find velocity dispersion to be strongly affected by the inclusion of squirt flow effects. The BISQ model of Dvorkin and Nur is extended in [71], where Jakobsen and Chapman present a more generalized theory describing the behavior of cracked anisotropic poroelastic media derived using a T-matrix approach.

Following the approach of [70], Chotiros and Isakson develop a Biot

model that includes the effects of both grain contact squirt flow and viscous drag in [72]. Dubbed BICSQS, the theory proposed by Chotiros and Isakson models the compressive response of the solid in much the same way as in [70] and assumes the shear response to be dominated by the elastic behavior at the grain contacts and the viscous behavior of the fluid film that lies between any two adjacent grains. Chotiros and Isakson show that the BICSQS model can successfully model the sound speeds and attenuations as previously measured and discussed in the literature.

In the geophysics community, many researchers have attempted to extend Biot theory by including fractures and cracks. In [73], Berryman and Wang incorporate these features by generalizing Biot theory to allow for double-porosity dual-permeability media. By double-porosity dual-permeability it is meant that the medium has both the large-volume low-permeability porosity as described by Biot theory and low-volume high-permeability porosity associated with cracks and fractures. In addition to increasing the number of parameters, this generalization also increases the number of coupled equations from two to three. Another attempt at including cracks in Biot theory is made by XiaoMing in [74]. Here, XiaoMing takes the BISQ model of [70] and incorporates two parameters needed for proper modeling of cracked media—crack density and aspect ratio.

Another promising area of research is the extension of Biot theory to include more than one pore fluid such as in the case of a petroleum reservoir. Though several attempts at this extension to Biot theory were made before



them, Lo, Sposito, and Majer derive general equations of motion describing a two-fluid porous system following a similar procedure as that of Biot [75]. The researchers demonstrate that their equations reduce to those developed by previous researchers in special cases. For the two-fluid case, their work predicts the existence of yet another compressional wave in addition to the fast and slow waves of Biot theory.

One of the most widely acknowledged alternatives to Biot theory for the modeling of the acoustic behavior of unconsolidated sediments is the grain-shearing (GS) theory proposed by Buckingham in [66]. Unlike Biot theory, this model assumes that there is no elastic frame and that the translational and radial grain shearing occurring at the grain contacts when a wave passes is the main mechanism responsible for the sediment's acoustic properties. To ensure a better fit with the dispersion and frequency dependent attenuation behavior found by experiment and well described by Biot theory, Buckingham subsequently modified the GS theory and proposed another model including the effects of the pore fluid viscosity called the viscous grain shearing (VGS) theory in [76]. The physical validity of both the GS and VGS theories is called into question in [77], where Chotiros and Isakson argue that neither model adequately matches the wave speeds and attenuations observed during the SAX99 experiments and those experimentally measured by Prasad and Messner in [78]. Buckingham attempts to resolve one issue brought up by Chotiros and Isakson, the disagreement of the VGS theory with measured shear wave attenuations, by proposing another modification to his model in

[79].

## **2.2 Roughness Scattering**

Background on the extensively-studied problem of wave scattering from rough surfaces is provided in this section. First, a brief overview of the analytic models most commonly utilized to theoretically treat rough surface scattering is given. Then, the manner in which these models are extended to the specific application of acoustic scattering from seafloor roughness is described. This section concludes with a survey of the work comparing the predictions of scattering theories to experimental measurement.

### **2.2.1 Analytic Scattering Models**

Wave scattering by random rough surfaces is a topic that has received extensive theoretical treatment in electromagnetics and acoustics. Such a surface is considered to be a random process [80] and is most frequently characterized in terms of its roughness spectrum, the power spectral density of its height deviations with respect to a reference surface [2]. While a number of numerical methods have been and are being developed to treat this problem more exactly [81], the preferred method of studying wave scattering from rough surfaces has been through the use of analytic models that approximate the scattered field given by the Helmholtz-Kirchhoff integral formulation. A somewhat exhaustive survey of these analytic approximations is given by Elfouhaily and Guérin in [82]; it is this survey that has largely guided what will be discussed here.

Small roughness perturbation theory, or just perturbation theory, is the oldest roughness scattering model and remains to this day to be one of the two most widely used. First introduced by Lord Rayleigh for his study of acoustic scattering from corrugated sinusoidal surfaces [83], the theory relies on the fact that, for surfaces with small roughness compared to an acoustic wavelength and small slopes, scattering problems can be recast as the combination of reflection from a smooth surface and the contribution of perturbative terms arising from the surface's slight deviation from the mean plane [80]. Following Rayleigh, Rice developed explicit first- and second-order perturbation theory expressions for electromagnetic scattering from one-dimensional conducting randomly rough surfaces [84]. Due to their contributions, the early form of perturbation theory is often referred to as the Rayleigh-Rice method. The Rayleigh-Rice method uses the so-called Rayleigh hypothesis as a starting point, which states that all waves scattered from the surface are outgoing, even at those points lower than the surface's maximum deviation above the mean plane [82].

To avoid appeal to the Rayleigh hypothesis, a newer, more rigorous form of perturbation theory has been derived based on the extinction theorem, which states that, for a surface of infinite extent, the scattered field must vanish below the surface. First applied to scattering from a periodic surface by Waterman in [85], it has since been applied to scattering from randomly rough surfaces by Agarwal [86], Lopez et al. [87], and Nieto-Vesperinas and García [88], among others. Despite its increased rigor, Jackson et al. show

that perturbation theory derived using the extinction theorem gives identical results to those obtained using the Rayleigh-Rice method when both are carried out to high order [89]. The validity of perturbation theory when used to calculate acoustic scattering from a rough pressure release boundary following a Gaussian roughness spectrum is studied by Thorsos and Jackson in [90]. Perturbation theory's validity when applied to scattering from surfaces following other roughness spectrum types remains an open question of research.

The second oldest and most frequently employed roughness scattering model is the Kirchhoff approximation. Also known as the tangent plane approximation, Kirchhoff theory calculates the scattered field on the surface of a rough interface by treating each surface point as if it is part of a flat tangent plane of infinite extent [80]. The scattered field is therefore the superposition of the reflections from each of these tangent planes. A boundary integral is then used to calculate the far-field scattered field. The Kirchhoff approximation is often used in complement with perturbation theory as it is most accurate near specular while perturbation theory has its greatest utility far from specular [2].

The Kirchhoff approximation was first developed by Brekhovskikh in [91] and applied to the case of a random rough surface by Isakovich in [92]. Both of these articles are only available in Russian. The model was first introduced to the English-speaking acoustics community some time later by Eckart in [93]. This early work often relies on physical intuition of the tangent plane concept. In order to provide a more rigorous justification for the scat-

tering theory's utility, a systematic mathematical derivation of the Kirchhoff approximation is given by [94], where the scattering theory is recognized to be equivalent to the first term in the iterative solution of an integral equation that determines the normal derivative of the scattered field on the surface. This iterative solution is investigated further by Litzka and McCoy in [95]. In general, the surface height distribution is assumed to be Gaussian. This assumption is not necessary for the Kirchhoff approximation and some work has been done toward addressing the case of a non-Gaussian distribution [96, 97]. At high frequencies, the Kirchhoff approximation's formulation is greatly simplified, as discussed by Barrick [98], among others.

Due to the assumptions made in its conception, the Kirchhoff approximation as developed by Brekhovskikh is limited in its utility by its neglect of shadowing effects. An early attempt at correcting for this defect is given in [99], where Wagner calculates a corrective shadowing function that is still employed to this day. Another attempt at including shadowing effects is made by Lynch in [100] through the use of a curvature correction found using a variational principle. Through Monte Carlo calculations, the validity of the Kirchhoff approximation when applied to surfaces following a Gaussian roughness spectrum and the accuracy of Wagner's shadowing correction are studied by Thorsos in [101]. As in the case of perturbation theory, the validity of the Kirchhoff approximation when applied to surfaces following other spectral forms remains an open question.

As mentioned above, perturbation theory and the Kirchhoff approxi-

mation have complementary regions of validity. Since it is rare for a given rough surface to fall completely within one of these regions, the two scattering theories are often used in tandem; models that combine the theories are often referred to as composite-roughness models [2]. Composite-roughness models have been developed in both *ad hoc* fashion [102] and with more rigor [103]. However, despite the existence of composite-roughness models, it is often desirable to have a scattering theory that works in both regions of validity. While many attempts at unifying theories have been made [82], one such theory that has seen considerable usage is the small-slope approximation. Originally proposed by Voronovich in [104], the small-slope approximation utilizes transformation properties of the scattering amplitude with respect to vertical shifts to construct a series for the T matrix in generalized surface slope [105, 106]. As intended, the small-slope approximation reduces to the Kirchhoff approximation near specular and to perturbation theory away from specular provided the surface slopes are sufficiently small. A detailed derivation of the small-slope approximation for the case of a Dirichlet boundary is given by Thorsos and Broschat in [106]. The same authors assess the accuracy of the small-slope approximation through comparison with exact results for the Dirichlet problem when the surface is assumed to follow a Gaussian roughness spectrum in [107].

### 2.2.2 Scattering from the Seafloor (Theory)

In order to properly treat the problem of acoustic scattering due to seafloor roughness, the analytic models described above have been adapted from the Dirichlet or Neumann type boundary problem to the case of a penetrable bottom. Although in reality the seafloor can consist of several layers of heterogeneous media resting upon a substrate, in some instances the ocean bottom can be successfully modeled as an infinite half-space consisting solely of a homogeneous medium for low frequencies, where the wavelength is much greater than the thickness of any one layer. Since early models assumed ocean sediments behaved as acoustic fluids, that was the natural starting point for studies of rough surface scattering. In [108], perturbation theory is applied by Miles to study the reflection from a rough two-fluid boundary. This work is extended to the case of bistatic scattering by Kuo in [109]. Clay adapts the Kirchhoff approximation as developed in [93] by Eckart to the two-fluid case in [110]. Clay, Medwin, and Wright extend this work further in [111] to include the effects of shadowing at shallow grazing angles. In [112], Kuperman uses perturbation theory to calculate the bottom forward reflection from a rough interface separating two fluid half-spaces and shows the equivalence of his results to those obtained from the Kirchhoff approximation as developed by Clay in the appropriate region of validity.

One of the most widely cited and employed models of the backscattering from a rough two-fluid boundary is the composite-roughness model developed by Jackson, Winebrenner, and Ishimaru in [113]. Here the fluid sediment is

allowed to have finite attenuation. A simpler and more general version of this model which includes sound absorption in the interface boundary condition is put forth by Mourad and Jackson in [114]. The model is extended to the case of bistatic scattering by Williams and Jackson in [115].

Since they support shear waves, it is often more physically accurate to model ocean sediments as elastic solids rather than as acoustic fluids. In [116], the more rigorous form of perturbation theory based on the extinction theorem is applied to the problem of scattering from a rough fluid-elastic interface by Dacol and Berman. Along similar lines, Jackson and Ivakin develop a perturbation model that includes both roughness scattering from the seabed and volume scattering from included inhomogeneities in [117]. The Kirchhoff approximation is adapted to the fluid-elastic case by Dacol in [118].

In addition to the use of perturbation theory and the Kirchhoff approximation, many researchers have treated the problem of acoustic scattering from a rough fluid-elastic interface using the small-slope approximation. The first development of the small-slope approximation for the fluid-elastic case is made by Berman in [119]. In this paper, Berman also compares the numerical results obtained using the small-slope approximation to those from perturbation theory, the Kirchhoff approximation, and an exact solution found using the Rayleigh-Fourier method. Berman finds the small-slope approximation to perform the best and notes that the Kirchhoff approximation misses some key physics. Distinct formulations of the small-slope approximation for the fluid-elastic scattering problem are also developed by Yang and Broschat in [120]



and Gragg, Wurmser, and Gauss in [121].

Efforts have been made to adapt the models that assume the sediment consists solely of a half-space to the more realistic case of layering. In [122], Kuo extends his early perturbation model to study the reflection loss from a seabed consisting of an elastic sediment layer overlying an elastic solid basement. Both interfaces are allowed to be rough, with the sediment-basement interface assumed to have greater roughness than the fluid-sediment interface. Similarly, McDaniel uses perturbation theory to study the backscattering from a thin rough sediment layer overlying a rough homogeneous half-space in [123]. However, here the layer and half-space roughnesses must be correlated and both the layer and half-space are modeled as acoustic fluids. In [124], Essen applies first-order perturbation theory to the case of scattering from a fluid sediment layer overlying an elastic half-space. Roughness is only considered at the seafloor in this model. Lyons, Anderson, and Dwan adapt the composite-roughness model of [113] to allow for scattering from a rough sub-bottom interface in [125]. As in [113], the effects of shear waves are neglected in this work. In [126], first-order perturbation theory based on the Rayleigh-Rice method is applied to study the effects of gradients on rough surface scattering. In this model, a small homogeneous fluid sediment layer borders the rough surface; below this layer, the sediment can contain shear and its properties can be modeled as a function of depth.

While the work described in the preceding paragraph deals with scattering from a seabed consisting of a single layer overlying a substrate, researchers

have also worked toward developing models that allow for an arbitrary number of sediment layers. Kuperman and Schmidt extend Kuperman's boundary perturbation method described in [112] to treat scattering from a stratified system of homogeneous layers separated with rough interfaces in [127]. Each layer can be modeled as either an acoustic fluid or an elastic solid and the network of layers can be terminated with either a fluid or elastic half-space. In [128], Tang uses first-order perturbation theory and develops Green's functions for the calculation of the scattered field due to the roughness present at the interfaces of an arbitrary number of fluid layers. Ivakin studies a similar problem using perturbation theory in [129] but allows for the substrate to be an elastic solid and accounts for the contribution of volume scattering due to inhomogeneities in each layer.

A particularly attractive model for the calculation of backscattering from seafloors containing arbitrary stratification that combines much of the theory pertaining to scattering from layers described above is the geoacoustic bottom interaction model (GABIM) described by Jackson et al. in a recent publication [130]. This model allows for rough interfaces between the water and the first sediment layer and between the last sediment layer and the basement. The sediment layers are assumed to be acoustic fluids with only the bottom permitting shear. It should be noted that the GABIM model, along with the models for scattering from layers described above, does not utilize the small-slope approximation. Despite its advantages over perturbation theory and the Kirchhoff approximation for half-space problems, the small-slope

approximation as derived by Voronovich is not applicable to layered seabeds due to inconsistencies with perturbation theory that arise for problems of this type. An alternative approach to the small-slope approximation that can be applied to scattering from layers is currently being devised by Jackson [131].

### **2.2.3 Scattering from the Seafloor (Model/Data Comparisons)**

Although one can assess the mathematical validity of the scattering models described above through comparisons with exact solutions to the Helmholtz-Kirchhoff integral, the only true way to determine a given model's physical validity is through comparison with experiment. Due to its widespread adoption, a number of researchers have compared the scattering strengths found using the composite-roughness model of [113] to measured data. In the original paper introducing the model, Jackson, Winebrenner, and Ishimaru compare their composite-roughness model to backscatter data measured at three sites—one in the Puget Sound (US) with a soft, silty bottom and two near Falmouth (UK) with sand bottoms [113]. For all three sites, the researchers find that the composite roughness model greatly underpredicts the measured backscattering strengths in the region calculated using perturbation theory. In the case of the first site, this disparity is found to be the result of neglecting volume scattering; when it is included, the calculated backscattering strengths are in much closer agreement with the data. In the region calculated using the Kirchhoff approximation, the effects of volume scattering are less important and there is reasonable agreement between the model and the data.

Further comparisons between the composite-roughness model and measured data are made by Stanic and coworkers and Lyons and coworkers. In [132], Stanic et al. compare high frequency backscattering measurements made near Panama City, Florida to the predictions of the composite roughness model and find reasonable agreement at 90 kHz. Stanic et al. report similar measurements taken in a coarse shelly area near Jacksonville, Florida in [133]. The researchers find good agreement between the model and data taken at 40 kHz for all grazing angles and at 60 kHz for grazing angles greater than  $23^\circ$ . However, there is found to be poor agreement between the model and data taken at 20 kHz; again, the model's neglect of volume scattering is thought to account for most of the disparity. In [125], Lyons, Anderson, and Dwan extend the composite-roughness model to include volume scattering and scattering from subbottom interfaces and compare calculated scattering strengths with those obtained from backscattering data taken off the coast of California. They find the extended model to be in good agreement with the collected data. Additional model/data comparison is made by Pouliquen and Lyons in [134] for high-frequency backscattering measurements taken at four sites in the Gulf of La Spezia, Italy. The model used here is based on the composite-roughness model but includes volume scattering and the effects of vertical gradients. The researchers note general agreement between the model and measurement but speculate that the model may not be accurate for very low grazing angles.

The composite-roughness model as modified in [114] to include volume scattering is compared with high-frequency backscattering data from three

sites by Jackson and Briggs in [135]. The first site, located off the coast of Washington state, is characterized by a fine-sand bottom with directional ripples. The second site, west of Cape Arnhem, Australia, has a smooth silt-clay bottom with many embedded shell fragments. The third site, near San Francisco, has a silt bottom of moderate roughness. It is found that roughness scattering dominates the first site while volume scattering is more prominent at the second and third sites, and, in general, the modified model is in good accord with the measured data at all three sites.

In [136], Jackson and coworkers compare the modified composite-roughness model and first-order perturbation theory to data from three experiments. Comparison of the models with the first data set, collected from a coarse sand sediment near Panama City, shows excellent agreement between perturbation theory and measurement while the composite-roughness model overpredicts the scattering strength for shallow grazing angles. The second data set was taken from a site near Key West characterized by substantial sediment gradients. When using surficial properties instead of averaged properties, both the composite-roughness and perturbation models are in good agreement with the backscattering measurements. The third set of backscattering measurements were taken from a soft, water-like sediment near Eckernförde. Neither model is found to agree with the data from this site and an observed methane bubble layer is thought to account for the measured backscattering.

Williams and Jackson further modify the composite-roughness model to the case of bistatic scattering and conduct model/data comparison using

measurements from two different sites in [115]. The first site had a bottom consisting of coarse-grained sand and the model is found to agree well with the data collected. The second site had a gassy-mud bottom and the model/data agreement is found to not be as good due to the presence of gas bubbles within the sediment. This bistatic model is used as the baseline for the model/data comparisons made by Briggs et al. in [137]. While they find good general agreement between the model and bistatic bottom scattering data taken in the Florida Keys at 40 kHz, the researchers note small discrepancies that reveal themselves upon close inspection.

In addition to those of the composite-roughness model, the predictions of other seafloor roughness scattering models have been compared with measured data. In [138], Thorne and Pace compare laboratory measurements of near-vertical scattering from a model rough surface to the Kirchhoff approximation and find good agreement over a wide range of frequencies. Further laboratory measurements are described by Thorne, Pace, and Al-Hamdani in [139]. Here, the researcher again find good agreement between the backscattering data and the Kirchhoff approximation near vertical incidence but only find moderate agreement for shallower grazing angles. More model/data comparison involving the Kirchhoff approximation is made by de Moustier and Alexandrou in [140]. This work shows good agreement between the scattering predicted by the Kirchhoff approximation and measurements made with a Sea Beam echo-sounder at 12 kHz for incident angles ranging from  $5^\circ$  to  $20^\circ$ , but, curiously, they could not get a good fit with their model for incident angles

less than  $5^\circ$ . One final comparison between model and data of note is made by Soukup and Gragg in [141]. Here, the researchers compare backscatter measurements from a limestone seafloor over a frequency range of 2-3.5 kHz to the small-slope approximation formulated in [121]. The small-slope approximation is found to not only fit the measured data but is able to be used for inversion purposes, demonstrating the model's great utility.

## **2.3 The Combined Problem**

This section discusses the limited research that has been performed thus far concerning acoustic scattering from a rough poroelastic interface, a problem which combines the subjects of the two preceding sections in this chapter. The first part discusses how controversy surrounding observed anomalous subcritical acoustic penetration into ocean sediments motivated much of the work dealing with the combined problem. Next, three journal articles concerning the theory for the combined problem are discussed. Finally, comparisons that have been made between measurements and various models, both published and unpublished, are outlined.

### **2.3.1 Subcritical Penetration**

The impetus for the study of the combined problem of acoustic scattering from rough poroelastic surfaces can be directly attributed to attempts at determining the primary mechanism responsible for anomalous subcritical acoustic penetration into ocean sediments observed by Chotiros and cowork-

ers in a series of experiments [57, 142, 143]. Many competing explanations were put forth to explain this anomaly. In [144], Chotiros proposes that the refraction of a Biot slow wave is the best explanation. However, the input parameters used by Chotiros to match the Biot model with experiment deviate significantly from those accepted as valid by most researchers [145]. An alternative theoretical explanation posited that scattering due to roughness at the water-sediment interface is the main mechanism responsible; this hypothesis is supported by the modeling work of Thorsos, Jackson, and Williams [9] and Pouliquen, Lyons, and Pace [146] and the experimental results of Maguer et al. [147], Simpson and Houston [148] and Lim, Paustian, and Lopes [149]. Additional explanations include the effect of using a narrow beamwidth and scattering of the evanescent wave by volume heterogeneities [147].

In order to resolve the subcritical penetration controversy, it was decided that one of the main goals of the high-frequency acoustic experiment SAX99 would be to assess the contribution of the slow wave, roughness scattering, and evanescent wave mechanisms [150]. During SAX99, penetration measurements were conducted by research groups from the Applied Physics Laboratory, University of Washington (APL-UW) and the Applied Research Laboratories, The University of Texas at Austin (ARL:UT). The measurements, model/data comparisons, and conclusions made by the APL-UW group are reported by Jackson et al. in [151]. The APL-UW researchers conclude that their measurements support the hypothesis that roughness scattering is the dominant mechanism responsible for subcritical penetration. The exper-



imental design and results of the ARL:UT group are presented by Chotiros, Smith, and Piper in [152]. The ARL:UT researchers find that the waves penetrating the sediment can be divided into at least four categories: (1) an initial refracted wave, (2) a dominant nonrefracted wave, (3) an evanescent wave, and (4) acoustic energy packets with later arrivals than the previous three categories. The researchers note that, while models exist that qualitatively describe the contributions of the roughness scattering and evanescent wave mechanisms to the phenomenon of subcritical penetration, no model that is quantitatively accurate exists and models that account for the porous nature sediments may prove to increase quantitative accuracy.

### **2.3.2 Theory**

As far as the present author is aware, there are only three journal articles dealing with theory for the combined problem of scattering from a rough poroelastic boundary. Two of these articles are relatively recent, explicitly concern seafloor roughness scattering, and directly stem from the subcritical penetration controversy described in some detail above. However, it is somewhat surprising to find the first work combining roughness scattering and poroelastic media was performed by Deresiewicz and Wolf only two years after Biot made his final major contribution to his theory. In their paper [153], Deresiewicz and Wolf apply Rayleigh's method for calculating the acoustic scattering from a corrugated pressure release surface [83] to the scattering of poroelastic waves from a free irregular boundary. Although the formulation

presented can be generalized to the case of oblique incidence by any of the three waves supported by the medium, the researchers specifically focus on normally incident fast and shear waves. The researchers note that, while most of what is observed is not surprising when compared to the elastic half-space problem, a few points of interest emerge. First, roughness and porosity cause waves of all three kinds to be scattered. Furthermore, for both incident fast and shear waves, there is one value of their wavelengths relative to the surface roughness that causes no mode conversion and one value where there is complete mode conversion. Finally, the work predicts resonances due to the standing Rayleigh waves produced that had been previously observed and initially considered to be spurious.

As mentioned above, the remaining two articles on the combined problem deal specifically with seafloor roughness scattering. In the first of these [10], Williams, Grochocinski, and Jackson extend the formulation of perturbation theory for scattering from a rough elastic seafloor found in [117] to the case of a rough poroelastic seafloor. As in [117], the scattering theory is developed using the matrix method of Ivakin [154]. The researchers assume that the sediment is a homogeneous, isotropic, poroelastic half-space governed by the form of Biot theory following Stoll and Kan [30] with a two-dimensional interface described by a power law roughness spectrum. When comparing the results of their model with those of perturbation theory for a simple fluid sediment, the researchers find that the poroelastic model predicts lower backscattering strengths than the fluid model for frequencies of 1 kHz and greater and note a

discrepancy as much as 3 dB at 100 kHz for grazing angles less than  $20^\circ$ . The researchers comment that there is “concern in the use of perturbation theory for unconsolidated sediments...[since] the roughness relief may not be small compared to the slow- and shear wavelengths.”

In the third article on theory for the combined problem [11], Yang, Broschat, and Galea extend their small-slope approximation model for one-dimensional rough fluid-elastic interfaces [120] to the case of a rough fluid-poroelastic interface and compare their results to a one-dimensional perturbation theory model based on [10]. Here, a small-slope expansion of the transition, or T-, matrix is used to develop an expression for the bistatic scattering cross section. As in [10], the sediment is assumed to be a homogeneous, isotropic, poroelastic half-space following the Biot-Stoll model of [30]. The one-dimensional interface is assumed to follow a modified power law roughness spectrum. The researchers compare their small-slope model with perturbation theory for frequencies of 100 Hz and 3 kHz and *rms* heights of 0.1 and 1 m. For backscattering, the researchers find that the two models agree for grazing angles less than  $45^\circ$  for all cases considered. Closer to normal incidence, discrepancies between the models do arise as  $kh$ , the product of the acoustic wavenumber and the *rms* surface height, is increased. For bistatic scattering for a grazing angle of  $45^\circ$ , the scattering strengths predicted by the two models diverge near specular for increasing  $kh$ , as expected. At the conclusion of their article, the researchers note that “while it is speculated that the [small-slope approximation] results are more accurate [than those of perturbation theory],

exact results are needed for comparison for the accuracy to be determined.” It is this statement that has provided motivation for much of the work described in this thesis.

### **2.3.3 Model/Data Comparisons**

In addition to the experimental work performed to resolve the sub-critical penetration controversy, some experimental results dealing with scattering from rough seafloors assumed to consist of poroelastic sediments have been reported in the literature and compared with theory. In [155], Stanic et al. presents backscattering data measured in the Gulf of Mexico over the frequency range of 40-180 kHz. The researchers compare these data to the predictions from the composite roughness model of [113], which assumes a fluid sediment, and the BOGGART model, an unpublished model formulated by Boyle and Chotiros that combines the roughness scattering from the Kirchhoff approximation for a poroelastic sediment with other models they developed for calculating the acoustic backscatter from trapped gas bubbles [156] and sediment grains [157]. Both models are found to agree with measurement at 40 kHz for grazing angles greater than  $17^\circ$ . The composite roughness model’s predictions at 110, 130, and 150 kHz are seen to be closer to measurement than those of the BOGGART model. Neither model is seen to agree with the measured data at 180 kHz. The researchers also conclude that the data show frequency-dependent variabilities in reverberation level that cannot be predicted by either model.

SAX99 provided Williams and coworkers the opportunity to thoroughly examine the backscattering from a well-characterized sand sediment over the substantial frequency range of 20 to 300 kHz for grazing angles from 10° to 40°. In [4], Williams et al. compare the backscattering measurements from SAX99 to the predictions of three different seafloor scattering models: a fluid model that uses the average density of the sediment and follows [115], the full poroelastic roughness perturbation model put forth in [10], and a perturbation model using the effective density fluid formulation described in [5]. Only the average density fluid model accounts for scattering from volume heterogeneities in addition to roughness scattering. The water-sediment surface is assumed to be described by a power law roughness spectrum and all the input parameters needed for the three models were obtained as part of the experiment. In the 20-50 kHz frequency range, roughness is concluded to be the dominant backscattering mechanism and the poroelastic and effective density fluid models are seen to be in closer agreement with the data. In the 50-150 kHz range, the poroelastic and effective density fluid models again outperform the simple fluid model. However, in this frequency range, none of the models adequately account for a drop in backscattering strength seen above 30° grazing; the authors speculate that volume scattering different than what is included in the fluid model based on [115] may explain the model/data discrepancy. For frequencies above 150 kHz, the researchers note disagreement between the predictions of all three models and measurement for grazing angles less than the critical angle and suggest that, somewhere between 150 and

300 kHz, the dominant backscattering mechanism transitions from roughness scattering to some other mechanism. It has been suggested to the present author that this other mechanism may be the multiple scattering that occurs at the grain level (see [158]).

Following the success of SAX99, a similarly structured experiment called SAX04 was performed within a kilometer of the SAX99 site. Despite their proximity, the sediment characteristics of SAX04 were rather different than those of SAX99 due to Hurricane Ivan and Tropical Storm Matthew [159]. In [160], Williams et al. compare backscattering measurements made over a similar frequency range to those of SAX99 to the predictions made by four seafloor scattering models of increasing complexity: (1) a roughness scattering model assuming the sediment to be a sand half-space, (2) a sand half-space model that includes both roughness and volume scattering mechanisms, (3) a combined roughness and volume scattering model that assumes the sediment to be a mud layer overlying a sand half-space and doesn't account for scattering of the upward traveling waves within the mud layer, and (4) a combined model that assumes the sediment to be a mud layer overlying a sand half-space and does account for scattering of upward traveling waves. All four models either follow or extend the formulation given in [115] and use experimentally determined values as inputs. The mud layer is modeled as a fluid while the sand half-space follows the Biot-based effective density fluid model of [5]. Unlike the results of SAX99, the model/data comparisons indicate roughness scattering was not a prominent contributor to backscattering

in SAX04 and volume scattering played a much larger role at all but the lowest frequency studied. Of the four models, both mud layer models show the best agreement with measurement for frequencies between 20 and 150 kHz with little difference between the two. As for SAX99, the authors note that the dominant mechanism responsible for backscattering seems to change above 150 kHz. The unpublished work of Ivakin suggests that scattering from shells may best explain the measured backscattering strengths above 200 kHz [161].

Accompanying the model/data comparisons performed for backscattering, work has been done dealing with how rough surface scattering affects forward scattering and reflection. In another paper related to SAX04 [162], Williams demonstrates that ensemble averaging of forward scattering measurements from a rippled sand seafloor can be used to estimate the flat surface plane wave reflection coefficients and that the effective density fluid model is in better accord with the measurements than a simple fluid model. In [3], Isakson et al. compare reflection loss measurements for grazing angles of  $7^\circ$  to  $77^\circ$  and frequencies of 5 to 8 kHz made using spherical waves with three models: a flat interface elastic model, a flat interface poroelastic model following the Biot-Stoll formulation of [30], and a rough interface poroelastic model accounting for scattering loss using the Kirchhoff approximation. For lower frequencies, roughness scattering is not prominent and the flat poroelastic model best matches the data. For higher frequencies, roughness scattering is significant and the predictions of the rough poroelastic model are most consistent with the data. In general, the elastic model is found to overpredict the

measured reflection loss.

## **2.4 The Finite Element Method**

The finite element method (FEM) is a numerical technique for approximating solutions to boundary-value problems. FEM requires that the domain of a given problem be discretized into a finite number of subdomains, called elements. A weak or variational formulation of a given partial differential equation is derived, solved in each element, and assembled to generate the global solution [163]. The method is particularly powerful in that a FEM solution converges to the exact solution provided the discretization of elements is sufficiently fine. FEM has been adapted to a myriad of problems in engineering and physics. Of particular relevance to the present work is how the method has been applied to acoustics problems involving poroelastic materials and to the study of wave scattering from rough surfaces; both of these applications will be discussed below.

### **2.4.1 Application to Poroelastic Media**

As far as the present author is aware, no work has been done to date toward developing a finite element formulation of Biot's poroelasticity equations for modeling the acoustic interaction of sound with the seabed. However, finite element formulations of Biot's equations have been derived for the modeling of sound absorbing porous materials used in many noise control applications [52]; many of these formulations are general enough to be directly used in un-



derwater acoustics modeling though they have seemingly not yet been applied in such a way. The first finite element formulation based on Biot's theory of poroelasticity is developed by Kang and Bolton in [164]. In this paper, weak forms of Biot's equations in two dimensions expressed in terms of the frame and fluid displacement fields are derived and coupled with acoustic finite elements using both open- and closed-pore interface conditions. This formulation is made more efficient and extended to three dimensions by Panneton and Atalla in [165] and to the axisymmetric case by Kang, Gardner, and Bolton in [166]. The convergence of poroelastic finite element formulations derived in terms of the frame and fluid displacement fields for one-dimensional and three-dimensional applications is studied by Dauchez, Sahraoui, and Atalla in [167]. The authors find that reliable results can be obtained for the mesh criterion of six linear elements per slow-wave wavelength except in the case of three-dimensional deformation problems, where the minimal number of elements required is difficult to predict.

While the finite element formulation based on the displacement fields has been shown to be accurate, the fact that there are six degrees of freedom per node can make its implementation difficult and calculations cumbersome. To overcome these limitations, Atalla and coworkers have derived a different formulation in terms of the frame displacement and pore fluid pressure hereafter referred to as the mixed formulation. The mixed formulation has the advantages of requiring only four degrees of freedom per node and coupling easily with acoustic media [52]. The mixed formulation is first introduced by

Atalla, Panneton, and Debergue in [8]. In this paper, the authors recast Biot's equations in terms of frame displacement and pore fluid pressure and develop weak integral forms for FEM implementation. It should be noted that, while the equations of motion themselves are exact, the weak forms developed require that the frame bulk modulus be much less than the bulk modulus of the grains. This requirement is always satisfied if air is the pore fluid and can be shown to remain valid for the conventional parameter sets employed for sandy sediments. A follow-up paper by the same authors [168] discusses poroelastic-elastic, poroelastic-acoustic, and poroelastic-poroelastic coupling conditions for the mixed formulation in detail. In [169], Atalla, Hamdi, and Panneton develop alternative weak forms for the mixed formulation that require no approximation and couple more readily with elastic and poroelastic media.

#### **2.4.2 Application to Roughness Scattering**

Despite the robustness of the FEM, surprisingly little has been done toward applying the method to wave scattering from random rough interfaces. As with most research areas related to waves, the first treatment of such problems using FEM was made by the electromagnetics community. In [170], Lou and coworkers use FEM to conduct Monte Carlo simulations of electromagnetic scattering from random rough surfaces following Gaussian power spectra with an imposed Dirichlet boundary condition. The researchers use a periodic boundary condition to truncate the domain and compare the

ensemble-averaged Monte Carlo results of one hundred surface realizations to the Kirchhoff approximation and perturbation theory. Good agreement is found between FEM and the Kirchhoff approximation for rough surfaces of small slope. Similarly good agreement is seen between FEM and perturbation theory for surfaces with small roughness. Krause et al. extend the work of [170] to the case of rough surfaces with Neumann boundary conditions in [171]. Again, the rough surfaces are assumed to follow Gaussian statistics and good agreement is found between FEM, perturbation theory, and the Kirchhoff approximation in their respective regions of validity. This work is further extended by Lou, Tsang, and Chan to the case of penetrable rough boundaries in [172].

Currently, the only research applying the FEM to seabed roughness scattering of which the present author is aware is being performed by the Texas Sediment and Ocean Acoustics Research (TEXSOAR) group of which the present author is a member. In [173], Isakson, Yarbrough, and Chotiros apply Monte Carlo FEM to calculate the scattering strength from two-dimensional randomly rough pressure release surfaces and compare the ensemble averaged results to an exact integral solution, perturbation theory, and the Kirchhoff approximation. Three rough surface cases are considered—two following Gaussian power spectra and one following a measured non-Gaussian spectrum. For all three cases, the incident angle is set to  $45^\circ$  and the bistatic scattering strengths are calculated using formally averaged perturbation theory and the Kirchhoff approximation and the ensemble average of one hundred surface

realizations for the FEM and exact integral formulation. The FEM computational domain is truncated using perfectly matched layers following [174] and a modified Gaussian-tapered plane wave is utilized to further guard against edge effects. It is found that the FEM and exact integral solutions agree for all three cases and FEM agrees with perturbation theory for the first Gaussian case and with the Kirchhoff approximation for the second Gaussian case. For the non-Gaussian measured spectrum, neither the Kirchhoff approximation nor perturbation theory are in particularly good agreement with FEM. It should be noted that for this case, the approximation methods are calculated following a Gaussian roughness spectrum that approximates the measured non-Gaussian spectrum; this approximation most likely accounts for most of the disparities. This work has been extended to three dimensions by Joshi [175] and Tran [176].

In a recent paper [177], Isakson and Chotiros apply FEM to study acoustic scattering from two-dimensional randomly rough fluid-fluid and fluid-elastic interfaces. As in [173], perfectly matched layers are used to truncate the FEM domain and the incident field is modeled as a modified Gaussian-tapered plane wave. The rough surfaces are now assumed to follow the more physical von Karman power spectrum. Forward scattering, multistatic scattering, and backscattering strengths are calculated using the Monte Carlo approach for seventy-five surface realizations for the fluid-fluid case and forty realizations for the fluid-elastic case. For forward scattering, the FEM results are compared with the Kirchhoff approximation and Eckart model. For both the fluid

and elastic bottoms, the Kirchhoff approximation is in generally good agreement with FEM for angles greater than the critical angle and the Eckart model does well when only considering the coherent reflection loss. For multistatic scattering, the FEM results are compared with perturbation theory and the Kirchhoff approximation for grazing angles of  $10^\circ$ ,  $22^\circ$ ,  $50^\circ$ , and  $82^\circ$ . For both the fluid and elastic bottoms, FEM is found to agree with perturbation theory for all grazing angles and shown to agree with the Kirchhoff approximation as the grazing angle approaches normal incidence. For backscattering, FEM is again compared with perturbation theory and the Kirchhoff approximation with FEM and perturbation theory in generally good agreement for both bottom types and the Kirchhoff approximation in good agreement with FEM for all grazing angles for the fluid bottom and only for grazing angles greater than critical for the elastic bottom.

# Chapter 3

## Equations of Motion

This chapter is devoted to the equations governing the physics of the model problem shown in Figure 1.1. In the first section, the Biot equations are discussed and formulated in a manner conducive to finite element implementation. In the second section, the weak formulations needed to study the model problem with the finite element method are considered. The final section deals with the conditions needed to properly couple poroelastic and acoustic media.

### 3.1 Poroelasticity Equations

As discussed in length in Chapter 2, Biot developed the equations of motion governing wave propagation in porous media over a series of classic papers. For the low frequency case of Poiseuille flow, Biot's equations of motion can be written [26]

$$\rho \frac{\partial^2 \mathbf{u}}{\partial t^2} + \rho_f \frac{\partial^2 \mathbf{w}}{\partial t^2} - \nabla \cdot \sigma_t = 0, \quad (3.1)$$

$$\rho_f \frac{\partial^2 \mathbf{u}}{\partial t^2} + \bar{Y} \frac{\partial \mathbf{w}}{\partial t} + \nabla p_f = 0, \quad (3.2)$$

where  $\mathbf{u}$  is the displacement of the solid frame,  $\mathbf{w}$  is the pore fluid displacement with respect to the frame,  $\sigma_t$  is the total stress tensor,  $\rho_f$  is the pore fluid

density, and  $p_f$  is the pore fluid pressure.  $\rho$  is the average density of the medium and is given by

$$\rho = (1 - \beta) \rho_s + \beta \rho_f, \quad (3.3)$$

where  $\rho_s$  is the density of the grains and  $\beta$  is the porosity. The viscodynamic operator  $\bar{Y}$  is defined as [178]

$$\bar{Y} = \frac{\eta}{\kappa} + \rho_f \frac{\tau}{\beta} \frac{\partial}{\partial t}, \quad (3.4)$$

where  $\eta$  is pore fluid viscosity,  $\kappa$  is the permeability, and  $\tau$  is the tortuosity.

In order for Eq. 3.2 to be valid for higher frequencies, the viscodynamic operator must be modified to include the complex correction factor developed in [22]. The modified viscodynamic operator  $\tilde{Y}$  can be written

$$\tilde{Y} = \frac{\eta F(\Theta)}{\kappa} + \rho_f \frac{\tau}{\beta} \frac{\partial}{\partial t}. \quad (3.5)$$

Here,  $F(\Theta)$  is the complex correction factor and is defined as [29]

$$F(\Theta) = \frac{1}{4} \left[ \frac{\Theta T(\Theta)}{1 + 2iT(\Theta)/\Theta} \right], \quad (3.6)$$

where

$$T(\Theta) = \frac{\text{Ber}'(\Theta) + i\text{Bei}'(\Theta)}{\text{Ber}(\Theta) + i\text{Bei}(\Theta)} \quad (3.7)$$

and

$$\Theta = \sqrt{\frac{a^2 \omega \rho_f}{\eta}}. \quad (3.8)$$

In Eq. 3.7,  $\text{Ber}(z)$  and  $\text{Bei}(z)$  are the real and imaginary parts of the zeroth-order Kelvin function and  $\text{Ber}'(z)$  and  $\text{Bei}'(z)$  are their first derivatives with

respect to their arguments [22]. Using the relationship between Kelvin and Bessel functions outlined in [179], Eq. 3.7 can be rewritten

$$T(\Theta) = \frac{-e^{3\pi i/4} J_1(e^{3\pi i/4}\Theta)}{J_0(e^{3\pi i/4}\Theta)}, \quad (3.9)$$

where  $J_0(z)$  and  $J_1(z)$  are zeroth- and first-order Bessel functions of the first kind. In Eq. 3.8,  $a$  is the pore size parameter and  $\omega$  is the angular frequency [14]. The transition from the low- to the high-frequency regime as defined in [21] and [22] occurs when  $\Theta = 1$ . A characteristic frequency defining the point at which this transition occurs can be defined as

$$f_c = \frac{\eta}{2\pi\rho_f a^2}. \quad (3.10)$$

Letting  $\mathbf{u} = \mathbf{u}(\mathbf{x})e^{i\omega t}$  and  $\mathbf{w} = \mathbf{w}(\mathbf{x})e^{i\omega t}$  and incorporating the modified viscodynamic operator, Eqs. 3.1 and 3.2 can be rewritten [180]

$$\omega^2 \rho \mathbf{u} + \omega^2 \rho_f \mathbf{w} + \nabla \cdot \sigma_t = 0, \quad (3.11)$$

$$-\omega^2 \rho_f \mathbf{u} - \omega^2 \rho_c(\omega) \mathbf{w} + \nabla p_f = 0, \quad (3.12)$$

where

$$\rho_c(\omega) = \rho_f \frac{\tau}{\beta} + \frac{\eta F(\Theta)}{i\omega\kappa}. \quad (3.13)$$

While weak forms of Eqs. 3.11 and 3.12 have been developed and successfully implemented in finite element modeling [164, 165], it is often convenient to recast these equations solely in terms of the frame displacement  $\mathbf{u}$  and pore fluid pressure  $p_f$  in order to reduce the number of degrees of freedom



required to be solved and allow for easier coupling with acoustic media [52].

To eliminate  $\mathbf{w}$  from Eq. 3.11, Eq. 3.12 can be rewritten [180]

$$\mathbf{w} = \frac{1}{\omega^2 \rho_c(\omega)} (\nabla p_f - \omega^2 \rho_f \mathbf{u}) \quad (3.14)$$

and substituted into Eq. 3.11 to yield

$$\omega^2 \left( \rho - \frac{\rho_f^2}{\rho_c(\omega)} \right) \mathbf{u} + \frac{\rho_f}{\rho_c(\omega)} \nabla p_f + \nabla \cdot \sigma_t = 0. \quad (3.15)$$

Noting that  $\sigma_t = \sigma_t(\mathbf{u}, \mathbf{w})$ , it is now necessary to separate the total stress tensor into its components due to the frame and the pore fluid. From [25], the total stress tensor can be defined as

$$\sigma_t(\mathbf{u}, \mathbf{w}) = \sigma_s(\mathbf{u}, \mathbf{w}) - \beta p_f \mathbf{I}, \quad (3.16)$$

where  $\sigma_s(\mathbf{u}, \mathbf{w})$  is the stress tensor of the saturated frame and  $\mathbf{I}$  is the identity matrix. Following [8],  $\sigma_s$  can be redefined in terms of  $\mathbf{u}$  and  $p_f$  as follows:

$$\sigma_s(\mathbf{u}, \mathbf{w}) = \sigma_s(\mathbf{u}, p_f) = \hat{\sigma}_s(\mathbf{u}) - (\alpha - \beta) p_f \mathbf{I}. \quad (3.17)$$

Here,  $\hat{\sigma}_s(\mathbf{u})$  is the stress tensor of the frame *in vacuo* with components defined in terms of the frame bulk and shear moduli  $K_b$  and  $\mu$  according to the following relation:

$$\hat{\sigma}_{s,ij} = \delta_{ij} \left( K_b - \frac{2}{3} \mu \right) \nabla \cdot \mathbf{u} + \mu \left( \frac{\partial u_i}{\partial x_j} + \frac{\partial u_j}{\partial x_i} \right), \quad (3.18)$$

where  $\delta_{ij}$  is the Kronecker delta and  $\alpha$  is the Biot-Willis coefficient defined as

$$\alpha = 1 - \frac{K_b}{K_r}, \quad (3.19)$$

where  $K_r$  is the bulk modulus of the grains. It should be noted that often the real moduli  $K_b$  and  $\mu$  are replaced with complex moduli  $\tilde{K}_b$  and  $\tilde{\mu}$  in order to account for attenuation. These complex moduli can be calculated from the real moduli using the relations [14]

$$\tilde{K}_b = K_b \left( 1 + i \frac{\delta_K}{\pi} \right) \quad (3.20)$$

and

$$\tilde{\mu} = \mu \left( 1 + i \frac{\delta_\mu}{\pi} \right), \quad (3.21)$$

where  $\delta_K$  and  $\delta_\mu$  are the frame bulk and shear log decrements, respectively. Substituting Eq. 3.17 into Eq. 3.16, the total stress tensor can now be written as

$$\sigma_t(\mathbf{u}, \mathbf{w}) = \sigma_t(\mathbf{u}, p_f) = \hat{\sigma}_s(\mathbf{u}) - \alpha p_f \mathbf{I}, \quad (3.22)$$

and Eq. 3.15 becomes

$$\omega^2 \left( \rho - \frac{\rho_f^2}{\rho_c(\omega)} \right) \mathbf{u} + \nabla \cdot \hat{\sigma}_s(\mathbf{u}) + \left( \frac{\rho_f}{\rho_c(\omega)} - \alpha \right) \nabla p_f = 0. \quad (3.23)$$

To obtain Eq. 3.12 in terms of  $\mathbf{u}$  and  $p_f$ , a similar procedure will be followed to that used in both [8] and [180]. First, the divergence of Eq. 3.12 is taken to produce

$$-\omega^2 \rho_f \nabla \cdot \mathbf{u} - \omega^2 \rho_c(\omega) \nabla \cdot \mathbf{w} + \nabla^2 p_f = 0. \quad (3.24)$$

From [26],  $\nabla \cdot \mathbf{u}$  and  $\nabla \cdot \mathbf{w}$  can be related to  $p_f$  by

$$p_f = -\alpha M \nabla \cdot \mathbf{u} - M \nabla \cdot \mathbf{w}, \quad (3.25)$$

which can be rearranged to produce

$$\nabla \cdot \mathbf{w} = -\alpha \nabla \cdot \mathbf{u} - \frac{p_f}{M}. \quad (3.26)$$

Here,  $M$  is the so-called Biot modulus, which is defined as [69]

$$M = \frac{K_r}{\alpha + \beta (K_r/K_f - 1)}, \quad (3.27)$$

where  $K_f$  is the bulk modulus of the pore fluid. Substituting Eq. 3.26 into Eq. 3.24 yields

$$-\omega^2 \rho_c(\omega) \left( \frac{\rho_f}{\rho_c(\omega)} - \alpha \right) \nabla \cdot \mathbf{u} + \omega^2 \frac{\rho_c(\omega)}{M} p_f + \nabla^2 p_f = 0. \quad (3.28)$$

Defining  $\rho_{\text{eff}}$ ,  $k_{\text{eff}}$ , and  $\boldsymbol{\Psi}_c$  as

$$\rho_{\text{eff}}(\omega) = \rho - \frac{\rho_f^2}{\rho_c(\omega)}, \quad (3.29)$$

$$k_{\text{eff}}(\omega) = \omega \sqrt{\frac{\rho_c(\omega)}{M}}, \quad (3.30)$$

and

$$\boldsymbol{\Psi}_c(\omega) = \frac{\rho_f}{\rho_c(\omega)} - \alpha, \quad (3.31)$$

Eqs. 3.23 and 3.28 can now be written in terms of  $\mathbf{u}$  and  $p_f$ :

$$\nabla \cdot \hat{\sigma}_s(\mathbf{u}) + \omega^2 \rho_{\text{eff}}(\omega) \mathbf{u} + \boldsymbol{\Psi}_c(\omega) \nabla p_f = 0, \quad (3.32)$$

$$\nabla^2 p_f + k_{\text{eff}}^2(\omega) p_f - \omega^2 \rho_c(\omega) \boldsymbol{\Psi}_c(\omega) \nabla \cdot \mathbf{u} = 0. \quad (3.33)$$

When arranged in this way, the physical representation of the equations of motion become abundantly clear. Neglecting the third term, Eq. 3.32 is of the

same form as the elastodynamic equation of motion for the case of no body forces, where  $\rho_{\text{eff}}(\omega)$  is an effective density [181]. Similarly, Eq. 3.33 is of the same form as the Helmholtz equation, the equation of motion of an acoustic fluid, when the third term is neglected, and  $k_{\text{eff}}(\omega)$  behaves as an effective wavenumber [182]. The third term in each equation are thus coupling terms and  $\boldsymbol{\psi}_c(\omega)$  can therefore be referred to as the poroelastic coupling factor.

### 3.2 Weak Formulations

Weak integral forms of the equations of motion describing the physics of the problem depicted in Figure 1.1 are needed for finite element implementation. The acoustic fluid domain is governed by the Helmholtz equation [182],

$$\nabla^2 p_a + k_a^2 p_a = 0, \quad (3.34)$$

where  $p_a$  is the acoustic pressure and  $k_a$  is the acoustic wavenumber. Following the standard procedure for obtaining weak integral forms [183], Eq. 3.34 is multiplied by an admissible variation of  $p_a$ ,  $\delta p_a$ , and the divergence theorem is applied to yield [184],

$$-\int_{\Omega_a} (\nabla p_a \cdot \nabla \delta p_a - k_a^2 p_a \delta p_a) \, d\Omega_a + \int_{\Gamma} \delta p_a (\nabla p_a \cdot \hat{n}) \, d\Gamma = 0, \quad (3.35)$$

where  $\Omega_a$  denotes the acoustic domain and  $\Gamma$  refers to the rough interface.

The weak integral form of the poroelastic equations of motion can be obtained in a similar fashion. Following [8], Eq. 3.32 is multiplied by admissible

variation  $\delta \mathbf{u}$  and Eq. 3.33 is multiplied by admissible variation  $\delta p_f$ . Applying the divergence theorem, one obtains [184]

$$- \int_{\Omega_p} (\hat{\sigma}_{s,i} \cdot \nabla \delta u_i - \omega^2 \rho_{\text{eff}} \mathbf{u} \cdot \delta \mathbf{u} - \boldsymbol{\zeta}_c \nabla p_f \cdot \delta \mathbf{u}) \, d\Omega_p + \int_{\Gamma} (\hat{\sigma}_{s,i} \cdot \hat{n}) \delta u_i \, d\Gamma = 0, \quad (3.36)$$

$$- \int_{\Omega_p} (\nabla p_f \cdot \delta p_f - k_{\text{eff}}^2 p_f \delta p_f - \omega^2 \rho_c \boldsymbol{\zeta}_c \mathbf{u} \cdot \nabla \delta p_f) \, d\Omega_p + \int_{\Gamma} [\delta p_f (\nabla p_f \cdot \hat{n}) - \omega^2 \rho_c \boldsymbol{\zeta}_c \delta p_f (\mathbf{u} \cdot \hat{n})] \, d\Gamma = 0, \quad (3.37)$$

where  $\Omega_p$  specifies the poroelastic domain,  $\hat{\sigma}_{s,i}$  represents the  $i^{\text{th}}$  row of the drained stress tensor and  $\delta u_i$  is the  $i^{\text{th}}$  component of the vector  $\delta \mathbf{u}$ . Finally, correcting for the sign of the normal vector  $\hat{n}$ , multiplying Eq. 3.36 by  $\omega^2 \rho_f$ , and multiplying Eq. 3.37 by  $\rho_f / \rho_c$ , Eqs. 3.35, 3.36, and 3.37 can be added to obtain

$$\begin{aligned} & - \int_{\Omega_a} (\nabla p_a \cdot \nabla \delta p_a - k_a^2 p_a \delta p_a) \, d\Omega_a - \int_{\Gamma} \delta p_a (\nabla p_a \cdot \hat{n}) \, d\Gamma - \\ & \quad \omega^2 \rho_f \int_{\Omega_p} (\hat{\sigma}_{s,i} \cdot \nabla \delta u_i - \omega^2 \rho_{\text{eff}} \mathbf{u} \cdot \delta \mathbf{u} - \boldsymbol{\zeta}_c \nabla p_f \cdot \delta \mathbf{u}) \, d\Omega_p + \\ & \quad \omega^2 \rho_f \int_{\Gamma} (\hat{\sigma}_{s,i} \cdot \hat{n}) \delta u_i \, d\Gamma - \\ & \quad \frac{\rho_f}{\rho_c} \int_{\Omega_p} (\nabla p_f \cdot \nabla \delta p_f - k_{\text{eff}}^2 p_f \delta p_f - \omega^2 \rho_c \boldsymbol{\zeta}_c \mathbf{u} \cdot \nabla \delta p_f) \, d\Omega_p + \\ & \quad \frac{\rho_f}{\rho_c} \int_{\Gamma} [\delta p_f (\nabla p_f \cdot \hat{n}) - \omega^2 \rho_c \boldsymbol{\zeta}_c \delta p_f (\mathbf{u} \cdot \hat{n})] \, d\Gamma = 0. \quad (3.38) \end{aligned}$$

### 3.3 Poroelastic-Acoustic Coupling Conditions

For proper coupling between the acoustic and poroelastic domains, the following three conditions must be satisfied on the interface  $\Gamma$ :

$$\sigma_t \hat{n} = -p_a \hat{n}, \quad (3.39)$$

$$\mathbf{u} \cdot \hat{n} + \mathbf{w} \cdot \hat{n} = \frac{1}{\rho_a \omega^2} \nabla p_a \cdot \hat{n}, \quad (3.40)$$

$$p_f = p_a, \quad (3.41)$$

where  $\rho_a$  is the density of the acoustic medium and  $\hat{n}$  is the normal acting outward from the poroelastic domain into the acoustic domain. Eq. 3.39 ensures continuity of normal stresses. Eq. 3.40 enforces continuity of normal displacement. Eq. 3.41 invokes pressure continuity.

In order to enforce these condition, some manipulation of Eq. 3.38 is required. Using Eqs. 3.22, 3.14, and 3.31, Eq. 3.38 can be rewritten [168]

$$\begin{aligned} & - \int_{\Omega_a} (\nabla p_a \cdot \nabla \delta p_a - k_a^2 p_a \delta p_a) d\Omega_a - \int_{\Gamma} \delta p_a (\nabla p_a \cdot \hat{n}) d\Gamma - \\ & \quad \omega^2 \rho_f \int_{\Omega_p} (\hat{\sigma}_{s,i} \cdot \nabla \delta u_i - \omega^2 \rho_{\text{eff}} \mathbf{u} \cdot \delta \mathbf{u} - \boldsymbol{\zeta}_c \nabla p_f \cdot \delta \mathbf{u}) d\Omega_p + \\ & \quad \omega^2 \rho_f \int_{\Gamma} [(\sigma_{t,i} \cdot \hat{n}) \delta u_i + \alpha p_f \delta u_i \hat{n}] d\Gamma - \\ & \quad \frac{\rho_f}{\rho_c} \int_{\Omega_p} (\nabla p_f \cdot \nabla \delta p_f - k_{\text{eff}}^2 p_f \delta p_f - \omega^2 \rho_c \boldsymbol{\zeta}_c \mathbf{u} \cdot \nabla \delta p_f) d\Omega_p + \\ & \quad \frac{\rho_f}{\rho_c} \int_{\Gamma} [\omega^2 \alpha \rho_c (\mathbf{u} \cdot \hat{n}) \delta p_f + \omega^2 \rho_c (\mathbf{w} \cdot \hat{n}) \delta p_f] d\Gamma = 0. \quad (3.42) \end{aligned}$$

Setting  $\rho_f = \rho_a$ , substitution of Eqs. 3.39, 3.40, and 3.41 into Eq. 3.42 yields

$$\begin{aligned}
& - \int_{\Omega_a} (\nabla p_a \cdot \nabla \delta p_a - k_a^2 p_a \delta p_a) \, d\Omega_a - \\
& \quad \frac{\rho_a}{\rho_c} \int_{\Omega_p} (\nabla p_f \cdot \nabla \delta p_f - k_{\text{eff}}^2 p_f \delta p_f - \omega^2 \rho_c \boldsymbol{\varpi}_c \mathbf{u} \cdot \nabla \delta p_f) \, d\Omega_p - \\
& \quad \omega^2 \rho_a \int_{\Omega_p} (\hat{\sigma}_{s,i} \cdot \nabla \delta u_i - \omega^2 \rho_{\text{eff}} \mathbf{u} \cdot \delta \mathbf{u} - \boldsymbol{\varpi}_c \nabla p_f \cdot \delta \mathbf{u}) \, d\Omega_p + \\
& \quad \int_{\Gamma} \omega^2 \rho_a (\alpha - 1) (\mathbf{u} \cdot \hat{n}) \delta p_a \, d\Gamma + \\
& \quad \int_{\Gamma} \omega^2 \rho_a (\alpha - 1) (\delta \mathbf{u} \cdot \hat{n}) p_f \, d\Gamma = 0. \quad (3.43)
\end{aligned}$$

Eq. 3.43 shows that acoustic-poroelastic coupling is achieved through a symmetrical coupling term on the boundary. In addition, the condition  $p_f = p_a$  must be explicitly imposed on  $\Gamma$  [168].

## Chapter 4

### Finite Element Implementation

The purpose of this chapter is to describe how to approach addressing the model problem shown in Figure 1.1 using the finite element method (FEM). The first section outlines how to truncate the infinite domain of Figure 1.1 into a finite computational domain and discusses how to use the weak integral form developed in Chapter 3 to create a suitable FEM formulation of the model problem. The second section discusses further considerations needed to adequately adapt the model problem to one that can be solved using the FEM.

#### 4.1 Finite Element Formulation

The finite element method is applied to the model problem depicted in Figure 1.1 by truncating the two half-spaces into finite computational domains. Both domains have heights equal to two acoustic wavelengths and are surrounded by perfectly matched layers (PMLs) one acoustic wavelength thick in order to enforce the Sommerfeld radiation condition (see Section 4.2.2). The length of the computational domains requires further explanation and is discussed in Section 4.2.3. Figure 4.1 depicts the truncated model geom-



etry. Both the acoustic and poroelastic domains are divided into triangular

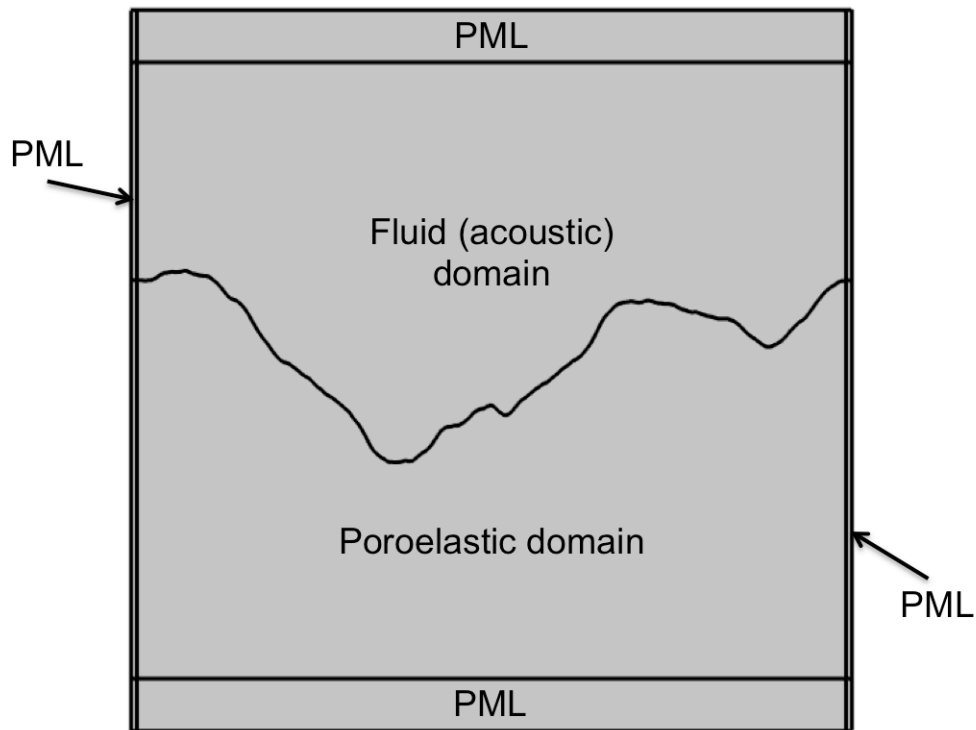


Figure 4.1: Model geometry (aspect ratio not preserved).

elements with the exception of the perfectly matched layers, which are divided into quadrilateral elements. Since the present work deals only in two dimensions, each element in the poroelastic domain has three degrees of freedom per node (the two frame displacement vector components and the pore fluid pressure) while the elements in the acoustic domain only have one degree of freedom per node (the acoustic pressure).

In accordance with typical finite element procedure [185], it is assumed

that the frame displacement, pore fluid pressure, and acoustic pressure of a given element can be approximated as

$$\mathbf{u}^e \approx [N_s] \{u_n\}^e, \quad (4.1)$$

$$p_f^e \approx [N_f] \{p_n^f\}^e, \quad (4.2)$$

and

$$p_a^e \approx [N_a] \{p_n^a\}^e, \quad (4.3)$$

where  $[N_s]$ ,  $[N_f]$ , and  $[N_a]$  are the element's shape functions (here assumed to be Lagrange polynomials of second order) used to approximate the frame displacement, pore fluid pressure, and acoustic pressure within element "e," and  $\{u_n\}^e$ ,  $\{p_n^f\}^e$ , and  $\{p_n^a\}^e$  are the element nodal values of the frame displacement, pore fluid pressure, and acoustic pressure, respectively [8]. Similarly, the permissible variations of Eq. 3.43 for a given element can be expressed as

$$\delta \mathbf{u}^e = [N_s] \{\delta u_n\}^e, \quad (4.4)$$

$$\delta p_f^e = [N_f] \{\delta p_n^f\}^e, \quad (4.5)$$

and

$$\delta p_a^e = [N_a] \{\delta p_n^a\}^e. \quad (4.6)$$

Before proceeding further, it is necessary to note that the plane wave impinging on the rough interface in Figure 1.1 is modeled by imposing a pressure field  $p_i$  on the acoustic domain  $\Omega_a$  and the interface  $\Gamma$ . Thus, the total acoustic pressure  $p_a$  can be written

$$p_a = p_i + p_{sc}, \quad (4.7)$$

where  $p_{sc}$  is the scattered pressure field, or the pressure left when the incident field  $p_i$  is subtracted from the total field  $p_a$ . Setting  $p_a = p_f$  on  $\Gamma$ , dividing by  $-\omega^2$ , and substituting Eq. 4.7 into Eq. 3.43 yields

$$\begin{aligned}
& \int_{\Omega_a} \left( \frac{1}{\omega^2} \nabla p_{sc} \cdot \nabla \delta p_a - \frac{1}{c_a^2} p_{sc} \delta p_a \right) d\Omega_a + \\
& \frac{\rho_a}{\rho_c} \int_{\Omega_p} \left( \frac{1}{\omega^2} \nabla p_f \cdot \nabla \delta p_f - \frac{\rho_c}{M} p_f \delta p_f - \rho_c \boldsymbol{\varpi}_c \mathbf{u} \cdot \nabla \delta p_f \right) d\Omega_p + \\
& \rho_a \int_{\Omega_p} \left( \hat{\sigma}_{s,i} \cdot \nabla \delta \mathbf{u}_i - \omega^2 \rho_{\text{eff}} \mathbf{u} \cdot \delta \mathbf{u} - \boldsymbol{\varpi}_c \nabla p_f \cdot \delta \mathbf{u} \right) d\Omega_p - \\
& \int_{\Gamma} \rho_a (\alpha - 1) (\mathbf{u} \cdot \hat{\mathbf{n}}) \delta p_a d\Gamma - \int_{\Gamma} \rho_a (\alpha - 1) (\delta \mathbf{u} \cdot \hat{\mathbf{n}}) p_{sc} d\Gamma \\
& = \int_{\Gamma} \rho_a (\alpha - 1) (\delta \mathbf{u} \cdot \hat{\mathbf{n}}) p_i d\Gamma, \quad (4.8)
\end{aligned}$$

where  $c_a$  is the acoustic sound speed.

Now the finite element implementation proceeds by substituting Eqs. 4.1–4.6 into Eq. 4.8. Through assembly, the following matrix expressions are obtained [8]:

$$\int_{\Omega_a} \nabla p_{sc} \cdot \nabla \delta p_a d\Omega_a \rightarrow \{\delta p_n^a\}^T [H_a] \{p_n^{sc}\}, \quad (4.9)$$

$$\int_{\Omega_a} \frac{1}{c_a^2} p_{sc} \delta p_a d\Omega_a \rightarrow \{\delta p_n^a\}^T [Q_a] \{p_n^{sc}\}, \quad (4.10)$$

$$\int_{\Omega_p} \frac{\rho_a}{\rho_c} \nabla p_f \cdot \nabla \delta p_f d\Omega_p \rightarrow \{\delta p_n^f\}^T [\tilde{H}_p] \{p_n^f\}, \quad (4.11)$$

$$\int_{\Omega_p} \frac{\rho_c}{M} p_f \delta p_f d\Omega_p \rightarrow \{\delta p_n^f\}^T [\tilde{Q}_p] \{p_n^f\}, \quad (4.12)$$

$$\int_{\Omega_p} \rho_a \hat{\sigma}_{s,i} \cdot \delta u_i d\Omega_p \rightarrow \{\delta u_n\}^T [K_p] \{u_n\}, \quad (4.13)$$

$$\int_{\Omega_p} \rho_a \rho_{\text{eff}} \mathbf{u} \cdot \delta \mathbf{u} d\Omega_p \rightarrow \{\delta u_n\}^T [\widetilde{M}_p] \{u_n\}, \quad (4.14)$$

$$\int_{\Omega_p} \rho_a \boldsymbol{\Psi}_c \nabla p_f \cdot \delta \mathbf{u} d\Omega_p \rightarrow \{\delta u_n\}^T [\widetilde{C}_p] \{p_n^f\}, \quad (4.15)$$

$$\int_{\Gamma} \rho_a (\alpha - 1) (\delta \mathbf{u} \cdot \hat{n}) p_{sc} d\Gamma \rightarrow \{\delta u_n\}^T [C_a] \{p_n^{sc}\}, \quad (4.16)$$

$$\int_{\Gamma} \rho_a (\alpha - 1) (\delta \mathbf{u} \cdot \hat{n}) p_i d\Gamma \rightarrow \{\delta u_n\}^T [C_a] \{p_n^i\}, \quad (4.17)$$

where  $\{u_n\}$ ,  $\{p_n^f\}$ ,  $\{p_n^{sc}\}$ , and  $\{p_n^i\}$  are the global vectors containing the nodal values of the frame displacement, pore fluid pressure, scattered pressure, and incident pressure, respectively. Likewise,  $\{\delta u_n\}$ ,  $\{\delta p_n^f\}$ ,  $\{\delta p_n^a\}$  are the global vectors corresponding to the permissible variations. Eq. 4.8 can now be written in matrix form:

$$\begin{bmatrix} [K_p] - \omega^2 [\widetilde{M}_p] & -[\widetilde{C}_p] & -[C_a] \\ -[\widetilde{C}_p]^T & [\widetilde{H}_p]/\omega^2 - [\widetilde{Q}_p] & 0 \\ -[C_a]^T & 0 & [H_a]/\omega^2 - [Q_a] \end{bmatrix} \begin{Bmatrix} u_n \\ p_n^f \\ p_n^{sc} \end{Bmatrix} = \begin{Bmatrix} F_i \\ 0 \\ 0 \end{Bmatrix}, \quad (4.18)$$

where

$$\{F_i\} = [C_a] \{p_n^i\}. \quad (4.19)$$

In Eq. 4.18,  $[K_p]$  and  $[\widetilde{M}_p]$  are the stiffness and mass matrices of the frame,  $[\widetilde{H}_p]$  and  $[\widetilde{Q}_p]$  are the kinetic and compression energy matrices of the pore fluid,  $[H_a]$  and  $[Q_a]$  are the kinetic and compression energy matrices of the

acoustic medium,  $[\tilde{C}_p]$  is a matrix coupling the solid and fluid phases of the porous medium, and  $[C_a]$  is the acoustic-poroelastic coupling matrix [52]. The tildes denote matrices that are frequency dependent. Eq. 4.18 can be solved using any number of available matrix solvers; MUMPS is used in the present work.

## 4.2 Modeling Considerations

This section deals with the particulars on how to go about properly modeling various aspects of the model problem not yet discussed. First, the method used to generate randomly rough surfaces is outlined. Second, the technique used to enforce the Sommerfeld radiation condition is described. Third, the incident field used to model a plane wave impinging on the rough surface is considered. Fourth, the mesh criteria needed to converge to the exact solution within sufficient accuracy is discussed. Finally, the manner in which the scattering strengths are calculated is reviewed.

### 4.2.1 Rough Surface Generation

Random rough surfaces, like those found on the ocean bottom, are generally described statistically in terms of their deviation from a smooth reference surface [80]. The most commonly employed statistical measure of this kind used to describe seafloor roughness is the power spectral density. One simple and commonly used model assumes the seafloor roughness follows

power-law spectra, formally described as [2]

$$W(\mathbf{K}) = \frac{w_1}{K^{\gamma_1}}, \quad (4.20)$$

where  $\mathbf{K}$  is the spatial wave vector,  $K$  is the spatial wavenumber, and  $w_1$  and  $\gamma_1$  are parameters referred to as the spectral strength and the spectral exponent, respectively.

While power law spectra have been found to agree closely with experimentally measured seafloor roughness in many cases, the fact that the power-law spectral form behaves pathologically when the spatial wavenumber approaches zero or infinity limits its utility. To address this limitation, the von Karman spectral form is often used instead. While behaving similarly to the power law in general, the von Karman spectral form approaches a constant value as the wavenumber approaches zero, and the spectral form approaches zero as the wavenumber approaches infinity [2]. Formally, it is given as

$$W(\mathbf{K}) = \frac{w_1}{(K^2 + K_0^2)^{\gamma_1/2}}, \quad (4.21)$$

where the parameter  $K_0$  is referred to as the cutoff wavenumber. For given von Karman roughness parameters, the *rms* height  $h$  can be determined using the following expression from [2]:

$$h = \sqrt{\frac{2\pi w_2}{(\gamma_2 - 2) K_0^{(\gamma_2-2)}}}. \quad (4.22)$$

In Eq. 4.22,

$$\gamma_2 = \gamma_1 + 1, \quad (4.23)$$

and

$$w_2 = w_1 \frac{\Gamma(\frac{\gamma_2}{2})}{\sqrt{\pi}\Gamma(\frac{\gamma_2-1}{2})}, \quad (4.24)$$

where  $\Gamma(z)$  is the gamma function [179].

Once a spectral form is chosen, surface realizations can then be created for a set of  $N$  points with spacing  $\Delta x$  over length  $L = N\Delta x$ . The realizations of the surface height function are generated as follows for points  $x_n = n\Delta x$  ( $n = 1, \dots, N$ ) [101]:

$$f(x_n) = \frac{1}{L} \sum_{j=-N/2}^{N/2-1} F(K_j) e^{iK_j x_n}, \quad (4.25)$$

where, for  $j \geq 0$ ,

$$F(K_j) = [2\pi L W(K_j)]^{1/2} \begin{cases} \frac{N(0,1) + iN(0,1)}{\sqrt{2}}, & j \neq 0, N/2 \\ N(0, 1), & j = 0, N/2 \end{cases} \quad (4.26)$$

and, for  $j < 0$ ,

$$F(K_j) = F(K_{-j})^*. \quad (4.27)$$

In the above expressions,  $K_j = 2\pi j/L$  and  $N(0, 1)$  represents an independent sample of a zero mean, unit variance Gaussian distribution. For the present work, an ensemble of fifty different surface realizations are created for each parameter set studied.

#### 4.2.2 Perfectly Matched Layers

In order to facilitate the modeling of infinite domains using the finite element method, a way to properly truncate the computational domain while still enforcing the Sommerfeld radiation condition must be implemented. One

such technique is the use of perfectly matched layers (or PMLs). Originally formulated by Bérenger [174], PMLs simulate absorbing layers made of an anisotropic damping material that surround the domain of interest and absorb the scattered field present at the boundary. While first formulated for problems in electromagnetism, PMLs have successfully been used in problems dealing with acoustic scattering [186, 187] and wave propagation in elastic [188] and poroelastic [189] media.

As done by Zampolli et al. in [187], the acoustic wavelength thick layers surrounding the computational domains are converted to PMLs by applying a coordinate transformation that amounts to a scaling to complex coordinates. This transformation makes the PML selectively dissipative in the direction corresponding to the transformed coordinate. For 2-D Cartesian coordinates, this transformation is as follows [180]:

$$x' = \operatorname{sgn}(x - x_0) |x - x_0| \frac{\lambda_{\text{ref}}}{D} (1 - i), \quad (4.28)$$

$$z' = \operatorname{sgn}(z - z_0) |z - z_0| \frac{\lambda_{\text{ref}}}{H} (1 - i), \quad (4.29)$$

where  $x'$  and  $z'$  are the transformed coordinates,  $x_0$  and  $z_0$  are the x- and z-coordinates of the inner PML boundary, and  $D$  and  $H$  are the PML's actual thickness and height, respectively. For this work,  $D$  is one acoustic wavelength and  $H$  is two acoustic wavelengths. The reference wavenumber  $\lambda_{\text{ref}}$  is defined

$$\lambda_{\text{ref}} = \frac{2\pi f}{c_{\text{ref}}}, \quad (4.30)$$

where  $f$  is the frequency and  $c_{\text{ref}}$  is chosen to be the fastest wave speed supported by the adjacent medium. For true truncation, the exterior boundary



of the PML must have a specified boundary condition; for the present problem, a Neumann condition is prescribed. The appropriate interface coupling conditions are enforced on the portion of the interior PML boundary that lies on the acoustic-poroelastic interface.

### 4.2.3 Incident Field

When modeling infinite domains, it is important to minimize scattering from the ends of surface realization. This goal is accomplished by tapering incident plane waves such that they are of negligible strength when they reach the edge PMLs. One such tapered plane wave is created by applying a Gaussian taper function, producing the following formulation of the incident pressure field [101]:

$$p_i(\mathbf{r}) = \exp [i\mathbf{k}_i \cdot \mathbf{r} - (x - z \cot \theta)^2 / g^2], \quad (4.31)$$

where  $\mathbf{k}_i$  is the incident wave vector,  $\mathbf{r}$  is the position vector,  $\theta$  is the mean grazing angle, and  $g$  is a parameter that controls the tapering.

It should be noted that the Gaussian tapered plane wave given above is not a solution of the Helmholtz equation. In [101], Thorsos gives a modified form of Eq. 4.31 that better approximates a solution:

$$p_i(\mathbf{r}) = \exp\{i\mathbf{k}_i \cdot \mathbf{r} [1 + w(\mathbf{r})] - (x - z \cot \theta)^2 / g^2\}, \quad (4.32)$$

where

$$w(\mathbf{r}) = \frac{2(x - z \cot \theta)^2 / g^2 - 1}{(kg \sin \theta)^2}, \quad (4.33)$$

and  $k$  is the wavenumber of the material through which the incident field propagates (water, in this case). Eq. 4.32 satisfies the Helmholtz equation to order  $(kg \sin \theta)^{-2}$  for  $kg \sin \theta \gg 1$ .

For the present work, a value of  $g = L/4$  is employed. In order to ensure that the condition  $kg \sin \theta \gg 1$  is sufficiently met, the length of the computational domain is chosen such that it obeys the Kapp criterion [190]

$$L \geq \frac{4A\sqrt{2}}{k\theta \sin \theta}, \quad (4.34)$$

with a value of  $A = 6.64$  used in this work. In practice, the computational domain length is chosen such that

$$L = \max \left( \frac{4A\sqrt{2}}{k\theta \sin \theta}, 80\lambda_a \right), \quad (4.35)$$

where  $\lambda_a$  is the acoustic wavelength.

#### 4.2.4 Mesh Criteria

When attempting to resolve wave motion using quadratic shape functions (such as the second order Lagrange polynomials used here), a good rule of thumb is to have elements be relatively uniform and sized no larger than  $\lambda/5$ , where  $\lambda$  is the wavelength corresponding to the slowest wave in the medium [180]. However, such a rule can lead to excessive computational cost for domains consisting of poroelastic materials, since the slow and shear wave speeds can often be more than an order of magnitude less than that of the fast wave. As the focus of the present work is on the acoustic scattering from rough fluid-poroelastic interfaces and not on the displacement and pressure fields inside

the poroelastic sediment, the mesh of the poroelastic computational domain only needs to be sufficiently fine such that there is no pollution error; that is to say, exact solution convergence below the fluid-poroelastic interface is currently not of particular importance. Since both the slow and shear waves are quite lossy and there is minimal coupling into the slow wave when the pore fluid is water, a mesh that becomes gradually coarser as it gets further from the rough interface is sufficient for scattering calculations as long as the maximum element size does not exceed the above rule of thumb for the fast wave. For very rough surfaces, a finer mesh may be required on the rough interface.

#### 4.2.5 Scattering Strength Calculation

For a given parameter set, the scattering strength is calculated using a Monte Carlo approach. For each rough surface realization, Eq. 4.18 is solved and the scattered pressure and its normal derivative are calculated on the interface  $\Gamma$ . As described in [177], the scattered pressure at a receiver in the far field is computed using the two-dimensional form of the Helmholtz-Kirchhoff integral [180]:

$$p_{sc}^{\text{ff}}(\mathbf{R}) = -\frac{i}{4} \int_{\Gamma} [H_0^{(2)}(k_a|\mathbf{r} - \mathbf{R}|) \nabla p_{sc}(\mathbf{r}) + kp_{sc}(\mathbf{r}) \frac{H_1^{(2)}(k_a|\mathbf{r} - \mathbf{R}|)}{|\mathbf{r} - \mathbf{R}|} (\mathbf{r} - \mathbf{R})] \cdot \hat{n} d\Gamma, \quad (4.36)$$

where  $H_0^{(2)}(z)$  and  $H_1^{(2)}(z)$  are the zeroth- and first-order Hankel functions of the second kind [179]. Taking the limit of Eq. 4.36 as  $|\mathbf{R}| \rightarrow \infty$  yields

$$p_{sc}^{\text{ff}}(\mathbf{R}) \approx \frac{1-i}{4\sqrt{\pi k_a}} \int_{\Gamma} \left[ \exp(ik_a \frac{\mathbf{r} \cdot \mathbf{R}}{|\mathbf{R}|}) \left( \nabla p_{sc}(\mathbf{r}) - ik_a p_{sc}(\mathbf{r}) \frac{\mathbf{R}}{|\mathbf{R}|} \right) \right] \cdot \hat{n} d\Gamma. \quad (4.37)$$

Once the far-field scattered pressure has been calculated for a number of realizations, the incoherent scattering cross section can be calculated using the following expression:

$$\sigma_s(\theta, \theta_s) = \frac{R [\langle |p_{sc}^{\text{ff}}(\mathbf{R})|^2 \rangle - |\langle p_{sc}^{\text{ff}}(\mathbf{R}) \rangle \langle \bar{p}_{sc}^{\text{ff}}(\mathbf{R}) \rangle|]}{E_f}, \quad (4.38)$$

where  $\langle \cdot \rangle$  denotes the ensemble average over all realizations,  $\theta_s$  is the scattering angle,  $\bar{p}_{sc}^{\text{ff}}$  is the complex conjugate of the far-field scattered pressure,  $\mathbf{R} = \mathbf{R}(\theta_s)$ ,  $R = |\mathbf{R}|$ , and the incident energy flux  $E_f$  is determined by the form of the incident beam. A value of  $R = 1000\lambda_a$  is used in the present work. For Eq. 4.32,  $E_f$  is given by [177]

$$E_f = \sqrt{\frac{\pi}{2}} g. \quad (4.39)$$

Finally, the scattering strength can be calculated using the following:

$$SS = 10 \log_{10} \sigma_s(\theta, \theta_s). \quad (4.40)$$

## Chapter 5

### Model Verification and Convergence

This chapter presents the results of the numerical studies performed to assess the validity of the finite element formulation given in Chapter 4 and determine the necessary mesh criteria for sufficient convergence to the exact solution. The first study calculates the absolute error of the finite element method as compared to the exact solution for the canonical problem of reflection from a flat fluid-poroelastic interface following [30] for meshes with different element sizes. The second study determines the relative error between finite element solutions of varying degrees of mesh refinement for the pressure field scattered from a single rough surface realization. Both studies are performed by implementing the finite element formulation from Chapter 4 in the commercial modeling code COMSOL Multiphysics version 4.3b.

#### 5.1 Absolute Error Study (Flat Surface)

In order to assess the absolute error of the finite element formulation outlined in Chapter 4, the calculated solution for the reflection from a fluid-poroelastic interface is compared to the analytical solution developed by Stoll and Kan in [30] and detailed in Appendix B of [14]. A somewhat more stream-

Table 5.1: Material properties used for absolute error study

<b>Parameter</b>	<b>Value</b>
Porosity ( $\beta$ )	0.47
Sediment grain density ( $\rho_s$ )	2650 kg/m <sup>3</sup>
Pore fluid density ( $\rho_f$ )	1000 kg/m <sup>3</sup>
Sediment grain bulk modulus ( $K_r$ )	36 GPa
Pore fluid bulk modulus ( $K_f$ )	2 GPa
Permeability ( $\kappa$ )	99.5 $\mu\text{m}^2$
Pore fluid viscosity ( $\eta$ )	0.001 kg/m-s
Tortuosity ( $\tau$ )	1.25
Pore size parameter ( $a$ )	39 $\mu\text{m}$
Frame shear modulus ( $\mu$ )	26.1 MPa
Shear log decrement ( $\delta_\mu$ )	0.15
Frame bulk modulus ( $K_b$ )	43.6 MPa
Frame log decrement ( $\delta_K$ )	0.15
Acoustic fluid density ( $\rho_a$ )	1000 kg/m <sup>3</sup>
Acoustic fluid sound speed ( $c_a$ )	1414 m/s

lined way to calculate the reflection coefficient analytically is presented in Appendix A of this thesis. The material properties used for this study also follow [30] and are stated in Table 5.1.

Using these material properties and a frequency value of 10 kHz, a finite element model is created in COMSOL Multiphysics following the formulation of Chapter 4 with the exception of the interface being left flat and thus only one realization being needed. The acoustic domain is discretized using a free triangular mesh with maximum element size  $\lambda_a/n$ , where  $n = 2, 4, 6, 8, 10, 12$ . The poroelastic domain is also discretized using a free triangular mesh. In accordance with the content of Section 4.2.4, the acoustic-poroelastic interface is set to have elements not exceeding  $\lambda/n$  with the element size allowed

to gradually increase in the poroelastic computational domain to a size not exceeding  $\lambda_{\text{fast}}/n$ . The PML regions are discretized using a mapped mesh of quadrilateral elements sized  $\lambda_{\text{ref}}/10$  in all cases. After solving Eq. 4.18 for all mesh cases, the reflection coefficient is determined for a given grazing angle  $\theta$  through use of the following expression:

$$RC(\theta) = \frac{1}{L} \int_{-L/2}^{L/2} \frac{p_{sc}(x, 0)}{p_i(x, 0)} dx. \quad (5.1)$$

After solving Eq. 5.1 for  $\theta$  values every  $5^\circ$  from  $10^\circ$  to  $90^\circ$ , the reflection loss (or bottom loss) can be easily calculated using the following expression [191]:

$$RL(\theta) = -20 \log_{10}|RC(\theta)|. \quad (5.2)$$

Grazing angles shallower than  $10^\circ$  are not considered due to the excessive computational cost.

Figures 5.1 and 5.2 show the analytical reflection loss and reflection coefficient phase plotted versus grazing angle as compared with the finite element results for computational domains consisting of elements of various sizes. It is immediately apparent that the finite element model agrees very well with the analytical phase calculation at all angles and with the analytical reflection loss calculation for all but the most shallow angles considered regardless of the level of mesh refinement.

To further quantify the discrepancy between the results of the different meshes and the disagreement with the analytical solution for shallow grazing

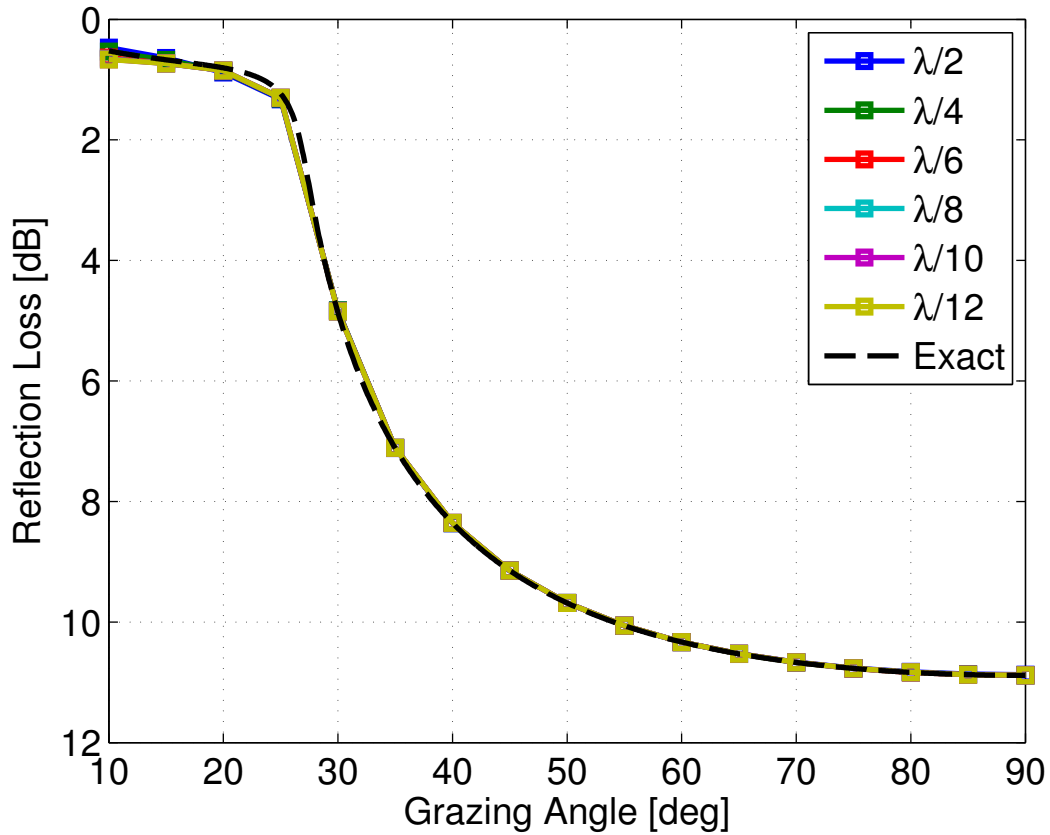


Figure 5.1: Comparison of the analytical and finite element reflection loss calculations for finite element meshes of varying element size.

angles, the absolute difference between the analytical and finite element reflection loss has been plotted as shown in Figure 5.3. Due to the nature of domain truncation and the fact that longer computational domains are needed for shallower grazing angles, it is not at all surprising that the largest error occurs at the shallowest grazing angle considered. However, upon initial inspection of this figure, it may seem curious that the error at this angle is worse for finer meshes and that, for all but the coarsest mesh considered, there is



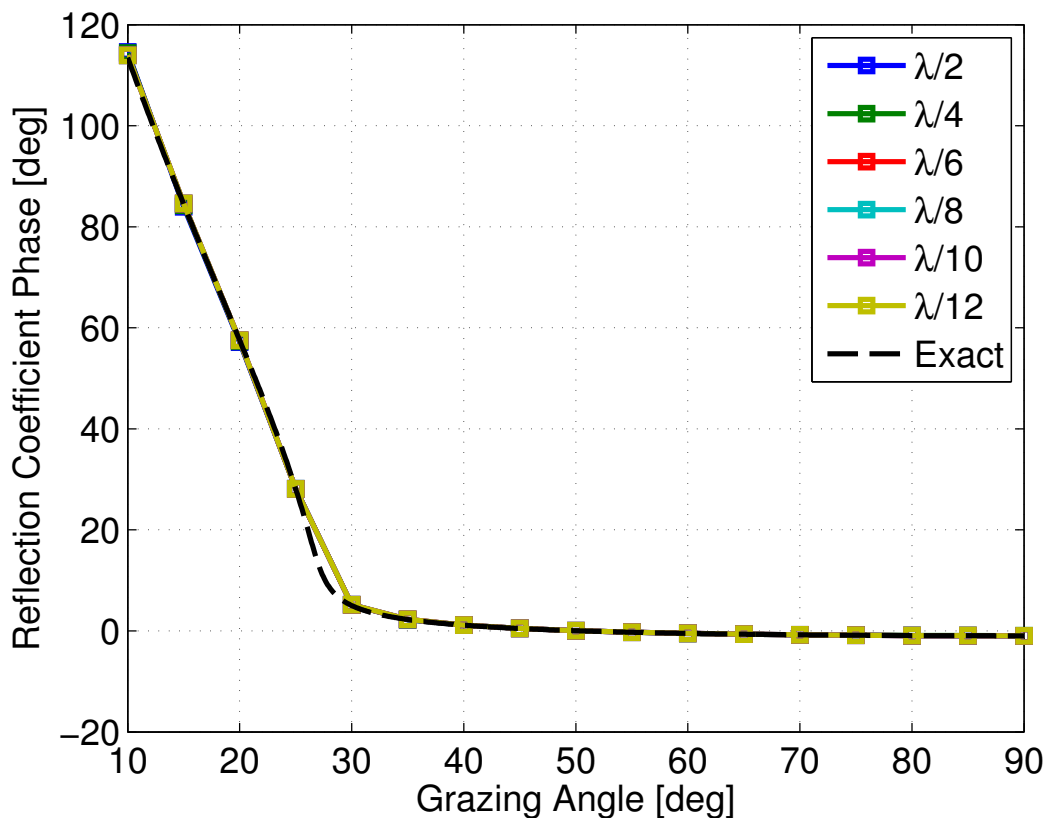


Figure 5.2: Comparison of the analytical and finite element reflection coefficient phase calculations for finite element meshes of varying element size.

virtually no difference between the analytical and finite element results until the grazing angle is less than the critical angle (approximately  $30^\circ$  in this case). While not yet quantified empirically, it is the present author's conjecture that the failure of Eq. 5.1 to account for the lateral displacement of the reflected field that occurs when the incident field is bounded may be responsible, as the amount of this displacement at a particular grazing angle is known to be directly related to the slope of the reflection coefficient phase at that angle

(see Section 14 of the first chapter of [192]). A cursory comparison of Figures 5.2 and 5.3 lends more credence to this conjecture. Discounting the error at the shallowest grazing angle and taking the possible error introduced by beam displacement into account, it is clear that the absolute error does in fact decrease as the element size is reduced and that only minimal reduction of error occurs when elements are sized less than  $\lambda/6$ . Furthermore, when using the mesh with elements sized  $\lambda/6$  or less, the absolute error is considerably less than 0.1 dB everywhere except the shallowest grazing angle considered; it is most likely that this error would be reduced even further if compensation was made for beam displacement. Perhaps the higher disparity at  $10^\circ$  shows the limitation of the  $A$  value chosen for the Kapp criterion but further study would be needed before making this conclusion.

## 5.2 Relative Error Study (Rough Surface)

As the rough interface in the model problem is statistical in nature, there is no exact solution available to assess the accuracy of the finite element method. However, since good agreement is found for the case of a flat interface and the formulation used is general as far as geometry is concerned, the only thing left to determine is if a rough interface affects the mesh criteria needed for adequate convergence. To check how the level of mesh refinement affects the convergence rate, a relative error study is performed in which a single rough surface realization is generated and the change in the scattered pressure values at five points on the interface as the mesh is refined is calculated. The model

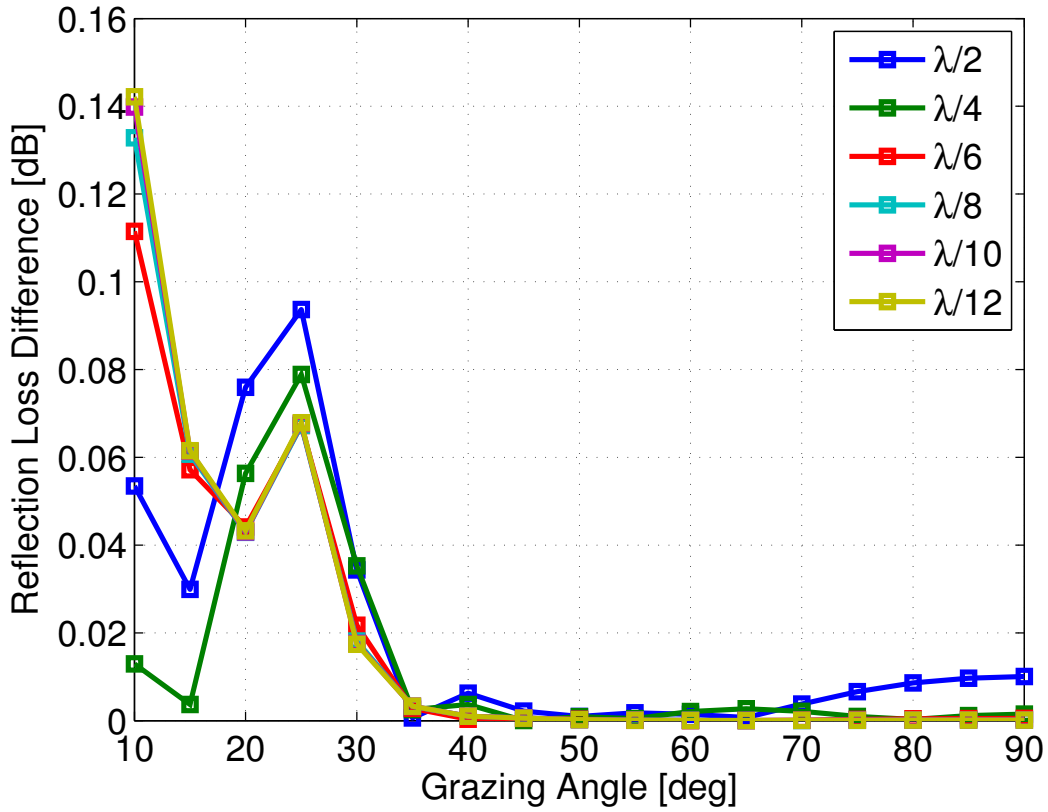


Figure 5.3: Absolute difference of analytical and finite element reflection loss calculations for finite element meshes of varying element size.

geometry used in this study is shown in Figure 5.4, where the points of interest are located in each of the annotated circles. The reason all five points used in this study are located on the interface is that, as described in Section 4.2.5, the scattered pressure on the interface is all that is used to evaluate the quantity of interest, the scattering strength. The material properties and roughness parameters used in this study are listed in Tables 5.2 and 5.3. Using Eq. 4.22 and the fact that the frequency is again set to 10 kHz in this study, the rough

Table 5.2: Material properties used for relative error study

<b>Parameter</b>	<b>Value</b>
Porosity ( $\beta$ )	0.38
Sediment grain density ( $\rho_s$ )	2690 kg/m <sup>3</sup>
Pore fluid density ( $\rho_f$ )	1023 kg/m <sup>3</sup>
Sediment grain bulk modulus ( $K_r$ )	25.5 GPa
Pore fluid bulk modulus ( $K_f$ )	2.3947 GPa
Permeability ( $\kappa$ )	30 $\mu\text{m}^2$
Pore fluid viscosity ( $\eta$ )	0.001 kg/m-s
Tortuosity ( $\tau$ )	1.2
Pore size parameter ( $a$ )	19.47 $\mu\text{m}$
Frame shear modulus ( $\mu$ )	29.2 MPa
Shear log decrement ( $\delta_\mu$ )	0.415
Frame bulk modulus ( $K_b$ )	43.6 MPa
Frame log decrement ( $\delta_K$ )	0.150
Acoustic fluid density ( $\rho_a$ )	1023 kg/m <sup>3</sup>
Acoustic fluid sound speed ( $c_a$ )	1530 m/s

Table 5.3: Roughness parameters used for relative error study

<b>Parameter</b>	<b>Value</b>
Spectral strength ( $w_1$ )	0.0037 cm <sup>3-<math>\gamma_1</math></sup>
Spectral exponent ( $\gamma_1$ )	3.28
Cutoff wavenumber ( $K_0$ )	0.01 cm <sup>-1</sup>

surface can be characterized by a  $k_a h$  value of 6.47, meaning that the roughness is rather large compared to an acoustic wavelength. The majority of the rough surfaces considered in the next chapter have considerably smaller  $k_a h$  values, making the roughness used here a good limiting case for a convergence study.

Again, COMOL Multiphysics is used to solve the problem corresponding to Figure 5.4 following the formulation outlined in Chapter 4 for a variety of meshes of different sized triangular elements. After obtaining the scattered

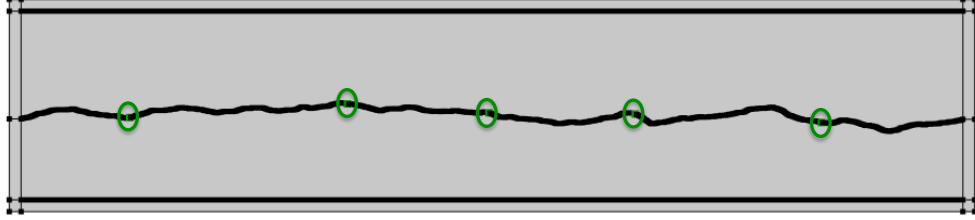


Figure 5.4: Geometry of model used for relative error study.

pressure field for all mesh cases, the sound pressure level (SPL) of the scattered pressure at point  $j$  for mesh characterized by element size  $\lambda/n$  is found using the following [193]:

$$\text{SPL}_j^n = 20 \log_{10} \frac{p_{sc}(x_j, 0)}{1 \mu\text{Pa}}. \quad (5.3)$$

The relative error in dB is then obtained by the following expression:

$$\text{dSPL}_j^n = \text{SPL}_j^n - \text{SPL}_j^{n-1}. \quad (5.4)$$

The results of this study are shown in Figure 5.5. For all five points, the SPL difference mostly plateaus after  $\lambda/6$ , corroborating the absolute error study's conclusion concerning mesh density. Therefore, the computational domain mesh used in the numerical studies of the next chapter are characterized by a maximum element size of  $\lambda/6$ .

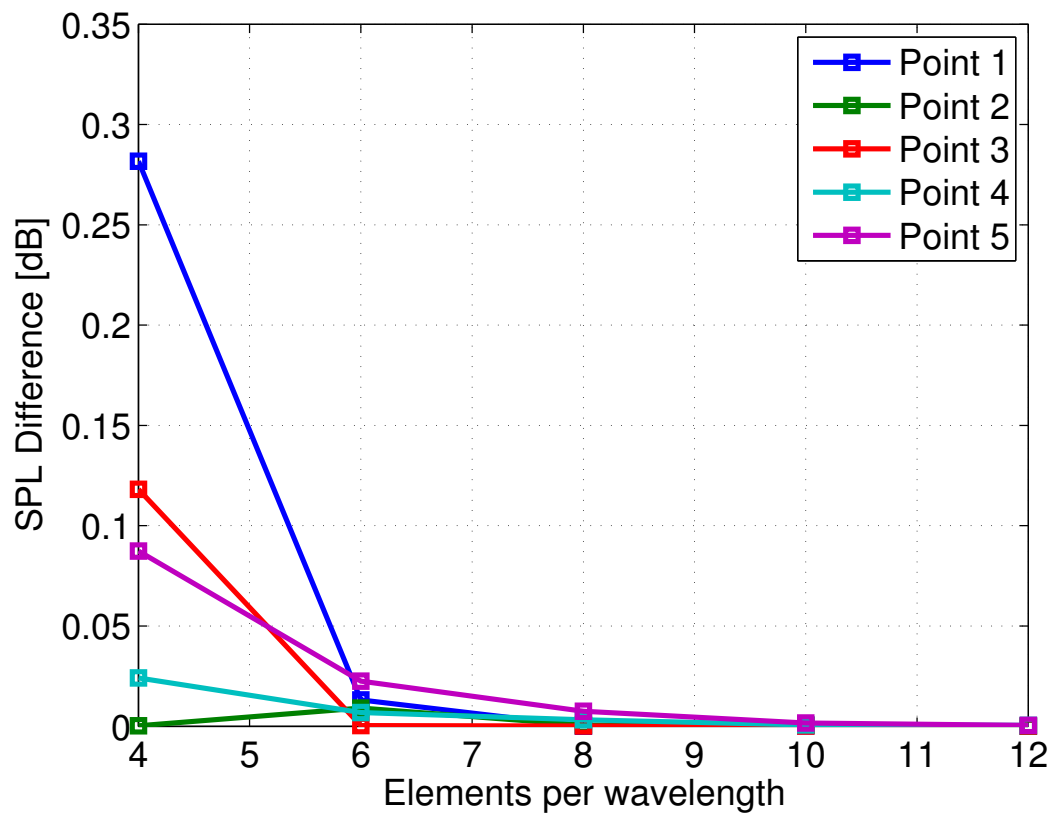


Figure 5.5: Relative SPL difference at five points located on the rough surface for increasing mesh refinement.

## Chapter 6

### Numerical Results

This chapter presents the main numerical results demonstrating the application of the finite element method to the problem of acoustic scattering from one-dimensional rough fluid-poroelastic interfaces. Using the formulation and modeling considerations given in Chapter 4, the model problem shown in Figure 1.1 is solved for material properties and roughness parameters following the papers by Yang, Broschat, and Galea [11] and Williams, Grochocinski, and Jackson [10]. For each parameter set, the finite element results are compared with the scattering strengths calculated using three analytic scattering models: perturbation theory (PT), the Kirchhoff approximation (KA), and the small-slope approximation (SSA); a brief overview of these scattering models is presented in Appendix B. The scattering strengths obtained using the full poroelastic finite element formulation are also compared with those found using finite element models that consider the bottom half-space to be a simple fluid and an effective density fluid that approximates a poroelastic medium following [5]; more information on these fluid models can be found in Appendix C.

## 6.1 Study 1: Following Yang et al. (2002)

The parameters used in the first numerical study follow those used by Yang, Broschat, and Galea in [11]. The material properties and roughness parameters are listed in Tables 6.1 and 6.2. As in [11], both monostatic and bistatic scattering strengths are calculated and compared. All combinations of frequencies and spectral strengths are considered. Finite element models of fifty rough surface realizations are solved for each combination. For the monostatic case, the finite element backscattering strengths are calculated every  $5^\circ$  for grazing angles ranging from  $10^\circ$  to  $90^\circ$ . For the bistatic case, the finite element scattering strengths are calculated every  $1^\circ$  for scattering angles ranging from  $1^\circ$  to  $180^\circ$ . All angles are measured with respect to the positive x-axis. It should be noted that for the properties given in Table 6.1, 100 Hz falls in Biot's low-frequency regime while 3 kHz is in Biot's high-frequency regime (the characteristic frequency is approximately 410 Hz).

### 6.1.1 Comparison with Analytic Scattering Models

The backscattering strengths found using the finite element method are compared with those calculated using perturbation theory, the Kirchhoff approximation, and the small-slope approximation in Figures 6.1 through 6.4. For the cases shown in Figures 6.1 and 6.2,  $k_a h$  is less than 1 and all three analytic models can be considered to be within their expected regions of validity. In Figure 6.1,  $k_a h = 0.04$  and PT, KA, and SSA are all in excellent agreement with FEM except at very shallow grazing angles, where KA is expected to per-



Table 6.1: Material properties following [11]

<b>Parameter</b>	<b>Value</b>
Porosity ( $\beta$ )	0.38
Sediment grain density ( $\rho_s$ )	2690 kg/m <sup>3</sup>
Pore fluid density ( $\rho_f$ )	1023 kg/m <sup>3</sup>
Sediment grain bulk modulus ( $K_r$ )	25.5 GPa
Pore fluid bulk modulus ( $K_f$ )	2.3947 GPa
Permeability ( $\kappa$ )	30 $\mu\text{m}^2$
Pore fluid viscosity ( $\eta$ )	0.001 kg/m-s
Tortuosity ( $\tau$ )	1.2
Pore size parameter ( $a$ )	19.47 $\mu\text{m}$
Frame shear modulus ( $\mu$ )	29.2 MPa
Shear log decrement ( $\delta_\mu$ )	0.415
Frame bulk modulus ( $K_b$ )	43.6 MPa
Frame log decrement ( $\delta_K$ )	0.150
Acoustic fluid density ( $\rho_a$ )	1023 kg/m <sup>3</sup>
Acoustic fluid sound speed ( $c_a$ )	1530 m/s

Table 6.2: Roughness parameters following [11]

<b>Parameter</b>	<b>Value(s)</b>
Frequencies ( $f$ )	100 Hz and 3 kHz
Spectral strengths ( $w_1$ )	$6.3662 \times 10^{-8}$ and $6.3662 \times 10^{-6} \text{ cm}^{3-\gamma_1}$
Spectral exponent ( $\gamma_1$ )	4
Cutoff wavenumber ( $K_0$ )	$0.001 \text{ cm}^{-1}$
Bistatic grazing angle ( $\theta$ )	$45^\circ$

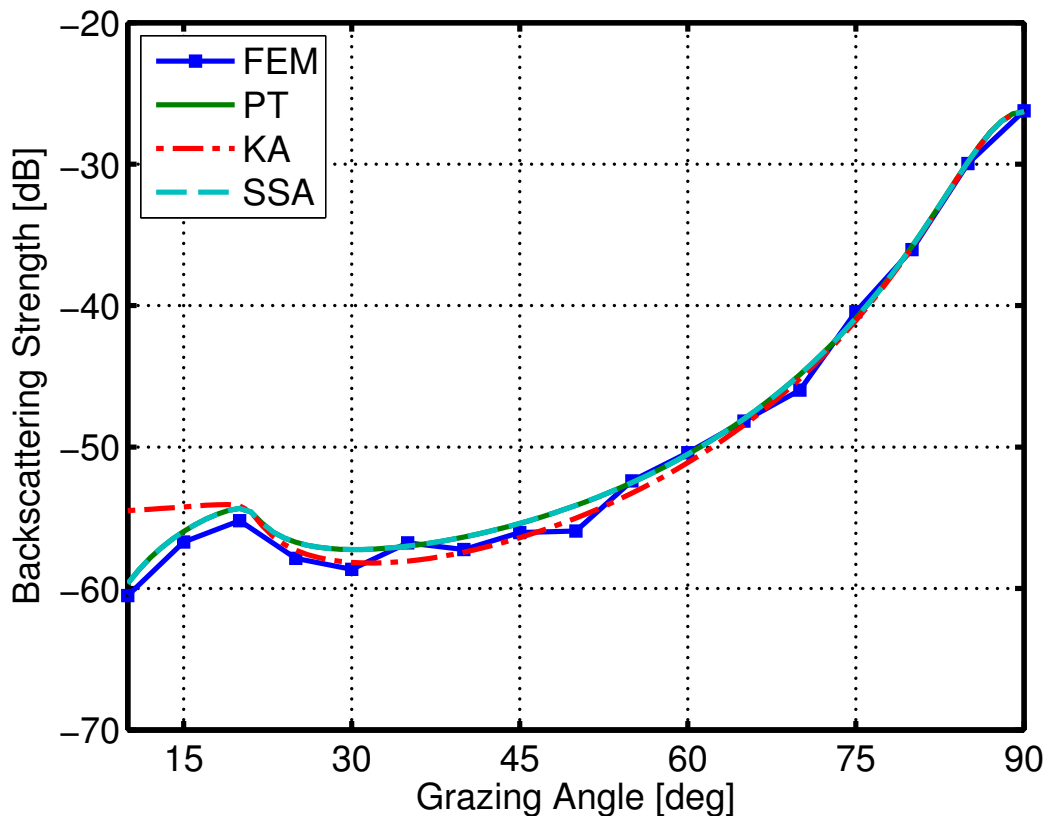


Figure 6.1: Comparison of finite element (FEM) monostatic scattering results with perturbation theory (PT), the Kirchhoff approximation (KA), and the small-slope approximation (SSA) for the following parameters:  $f = 100$  Hz,  $w_1 = 6.3662 \times 10^{-8} \text{ cm}^{3-\gamma_1}$ ,  $\gamma_1 = 4$ ,  $K_0 = 0.001 \text{ cm}^{-1}$  ( $k_a h = 0.04$ ).

form poorly. In Figure 6.2,  $k_a h = 0.42$  and the analytic models are in similarly good agreement with FEM with the exception of KA near grazing incidence and PT near normal incidence. For backscattering, the specular direction is  $\theta = 90^\circ$ ; PT is supposed to be accurate off specular and KA near specular, so the discrepancies seen in Figure 6.2 are expected. SSA, which converges to PT away from specular and to KA approaching specular for small surface

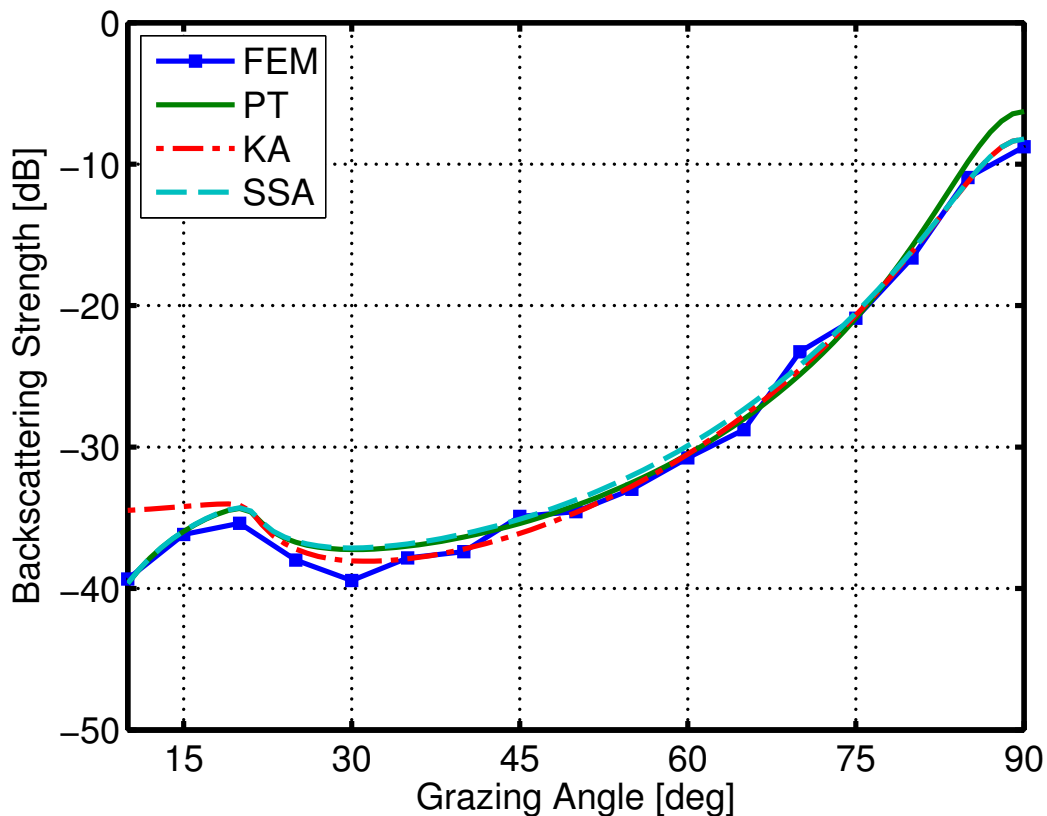


Figure 6.2: Comparison of finite element (FEM) monostatic scattering results with perturbation theory (PT), the Kirchhoff approximation (KA), and the small-slope approximation (SSA) for the following parameters:  $f = 100$  Hz,  $w_1 = 6.3662 \times 10^{-6} \text{ cm}^{3-\gamma_1}$ ,  $\gamma_1 = 4$ ,  $K_0 = 0.001 \text{ cm}^{-1}$  ( $k_a h = 0.42$ ).

slopes, does a good job matching the FEM results at all grazing angles, with a maximum deviation of about 2 dB at  $30^\circ$ .

For the cases shown in Figures 6.3 and 6.4,  $kh$  is greater than 1 and all three analytic models are thus outside their expected regions of validity. In Figure 6.3,  $k_a h = 1.26$  and there is considerable disagreement between FEM and all three scattering models at all angles, especially for grazing angles less

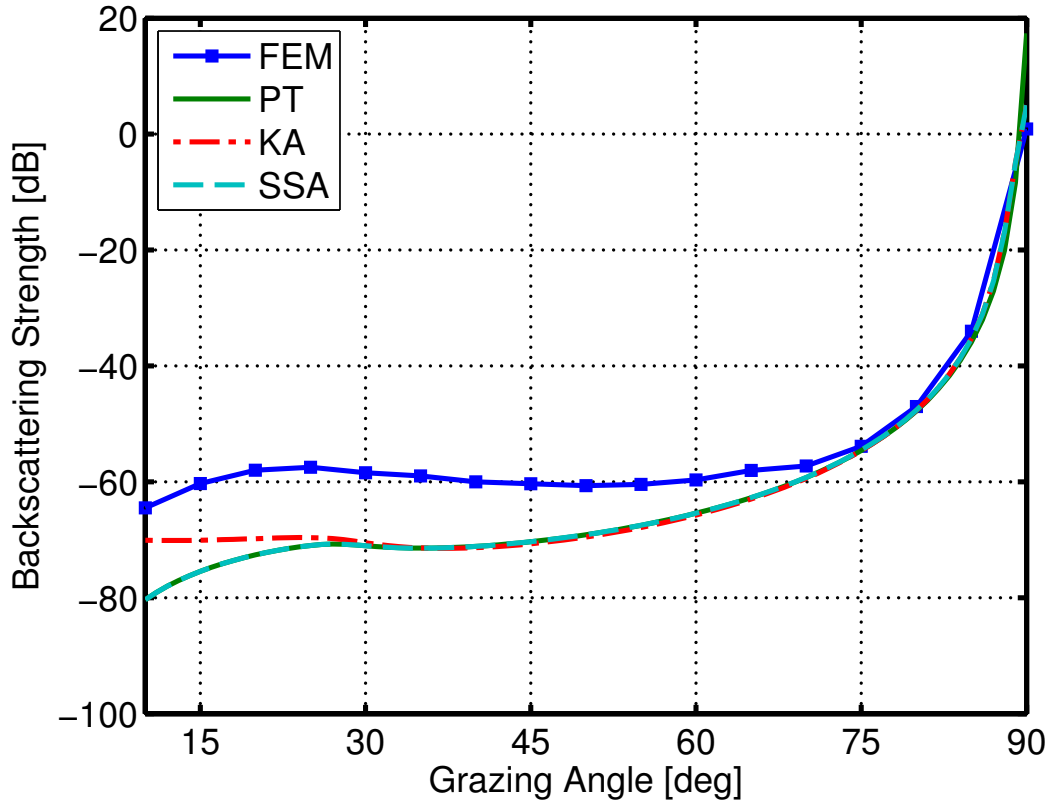


Figure 6.3: Comparison of finite element (FEM) monostatic scattering results with perturbation theory (PT), the Kirchhoff approximation (KA), and the small-slope approximation (SSA) for the following parameters:  $f = 3$  kHz,  $w_1 = 6.3662 \times 10^{-8} \text{ cm}^{3-\gamma_1}$ ,  $\gamma_1 = 4$ ,  $K_0 = 0.001 \text{ cm}^{-1}$  ( $k_a h = 1.26$ ).

than  $75^\circ$ , with the deviation between FEM and SSA reaching as much as 15 dB. In Figure 6.3,  $k_a h = 12.57$  and, despite the high  $k_a h$  value, SSA and KA do a very good job tracking the FEM results, with KA agreeing with FEM at all grazing angles. In fact, the only major discrepancy between FEM and KA occurs at  $\theta = 25^\circ$ , with the results of the two models differing by just under 2.5 dB; the results of the two models are within about 1 dB at all other

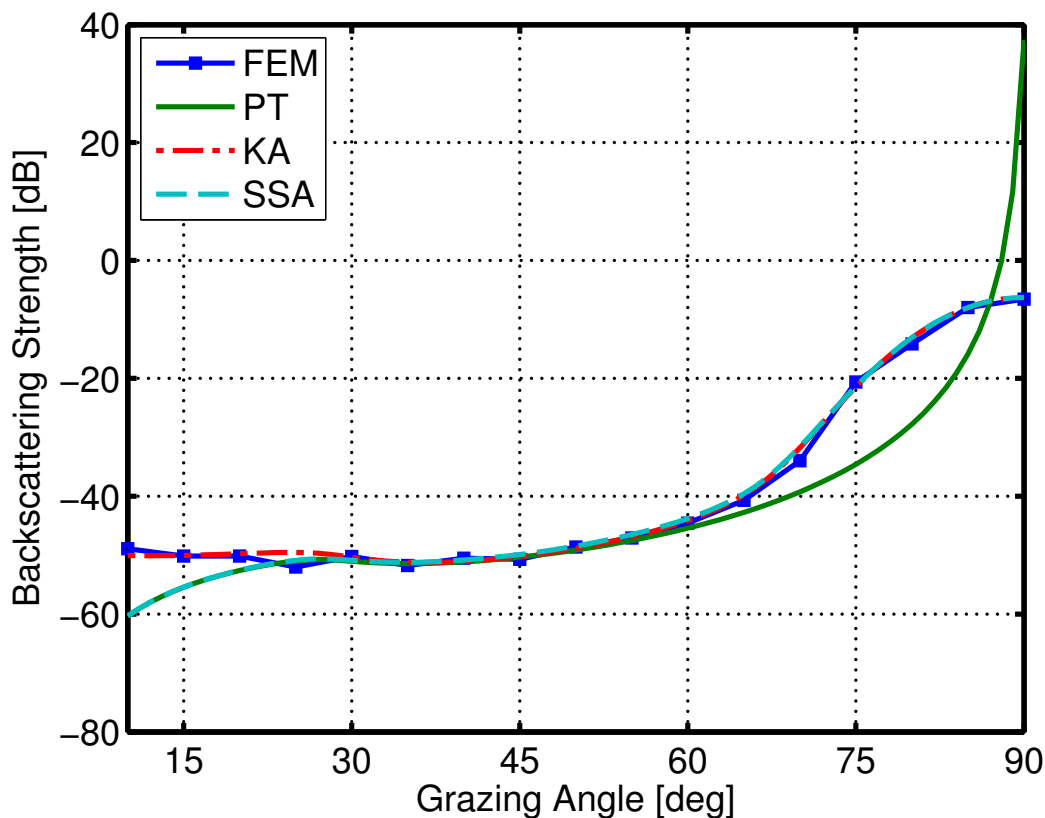


Figure 6.4: Comparison of finite element (FEM) monostatic scattering results with perturbation theory (PT), the Kirchhoff approximation (KA), and the small-slope approximation (SSA) for the following parameters:  $f = 3$  kHz,  $w_1 = 6.3662 \times 10^{-8} \text{ cm}^{3-\gamma_1}$ ,  $\gamma_1 = 4$ ,  $K_0 = 0.001 \text{ cm}^{-1}$  ( $k_a h = 12.57$ ).

grazing angles. It is unknown at this time why the agreement between the finite element and analytic models is better in Figure 6.4 than in Figure 6.3 despite  $k_a h$  being considerably lower in Figure 6.3; more work is needed to investigate the reason for this result.

Figures 6.5 through 6.8 compare the bistatic scattering strengths found using the finite element method with those calculated using perturbation the-

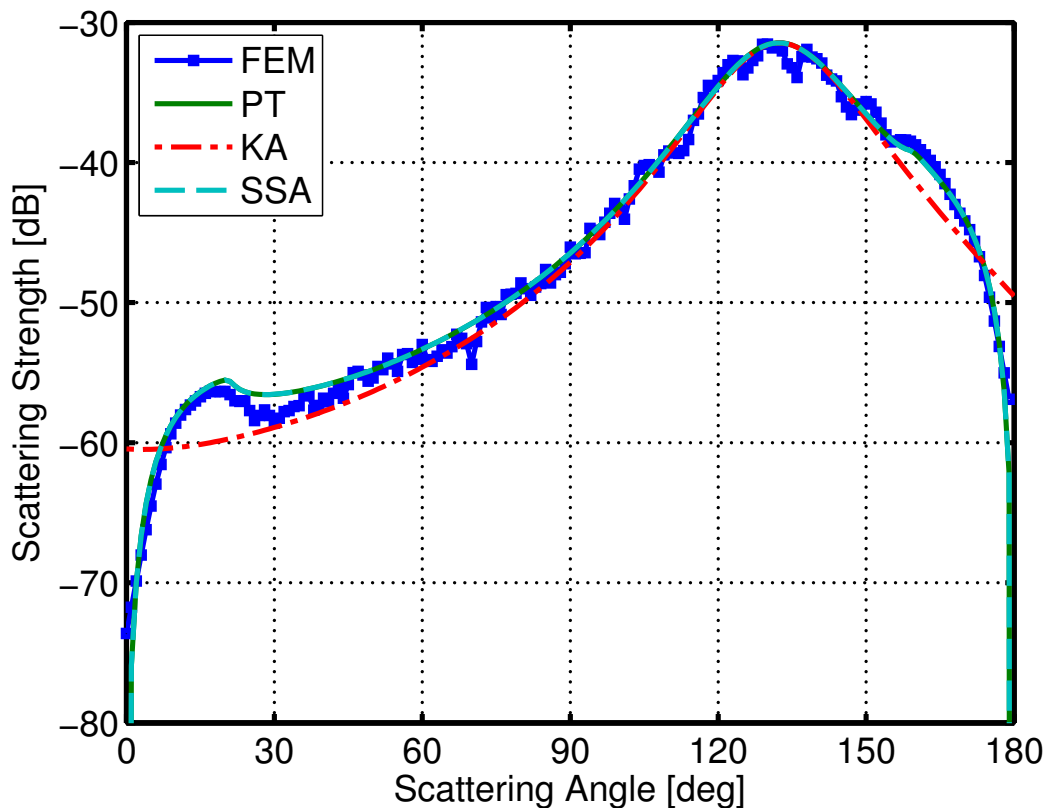


Figure 6.5: Comparison of finite element (FEM) bistatic scattering results with perturbation theory (PT), the Kirchhoff approximation (KA), and the small-slope approximation (SSA) for the following parameters:  $\theta = 45^\circ$ ,  $f = 100$  Hz,  $w_1 = 6.3662 \times 10^{-8} \text{ cm}^{3-\gamma_1}$ ,  $\gamma_1 = 4$ ,  $K_0 = 0.001 \text{ cm}^{-1}$  ( $k_a h = 0.04$ ).

ory, the Kirchhoff approximation, and the small-slope approximation. Following [11], the incident grazing angle is set to  $\theta = 45^\circ$  for all cases. In Figure 6.5,  $k_a h = 0.04$  and all three models are in excellent agreement with FEM excepting KA away from specular ( $\theta_s = 135^\circ$ ). SSA and PT are in exact agreement and match FEM within 2 dB at all scattering angles except  $\theta_s = 70^\circ$ , where the difference between the two analytic models and FEM reaches about 3 dB.

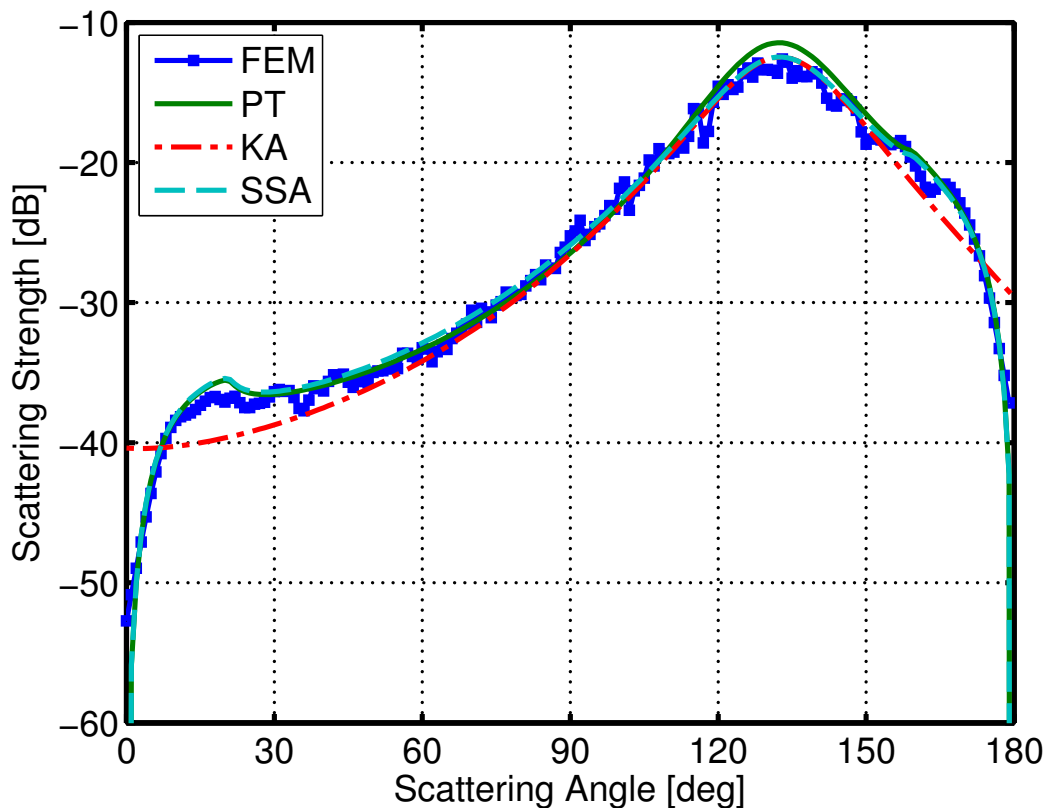


Figure 6.6: Comparison of finite element (FEM) bistatic scattering results with perturbation theory (PT), the Kirchhoff approximation (KA), and the small-slope approximation (SSA) for the following parameters:  $\theta = 45^\circ$ ,  $f = 100$  Hz,  $w_1 = 6.3662 \times 10^{-6} \text{ cm}^{3-\gamma_1}$ ,  $\gamma_1 = 4$ ,  $K_0 = 0.001 \text{ cm}^{-1}$  ( $k_a h = 0.42$ ).

Similarly good agreement between FEM and the analytic models is seen in Figure 6.6. Here,  $k_a h = 0.42$  and FEM is in good agreement with all three models excepting KA far from specular and PT close to specular. For this case, FEM and SSA are within 2 dB at all scattering angles. In Figure 6.7,  $k_a h = 1.26$  and there is considerable disagreement between FEM and all three analytic models for scattering angles less than  $90^\circ$ , with the disparity between

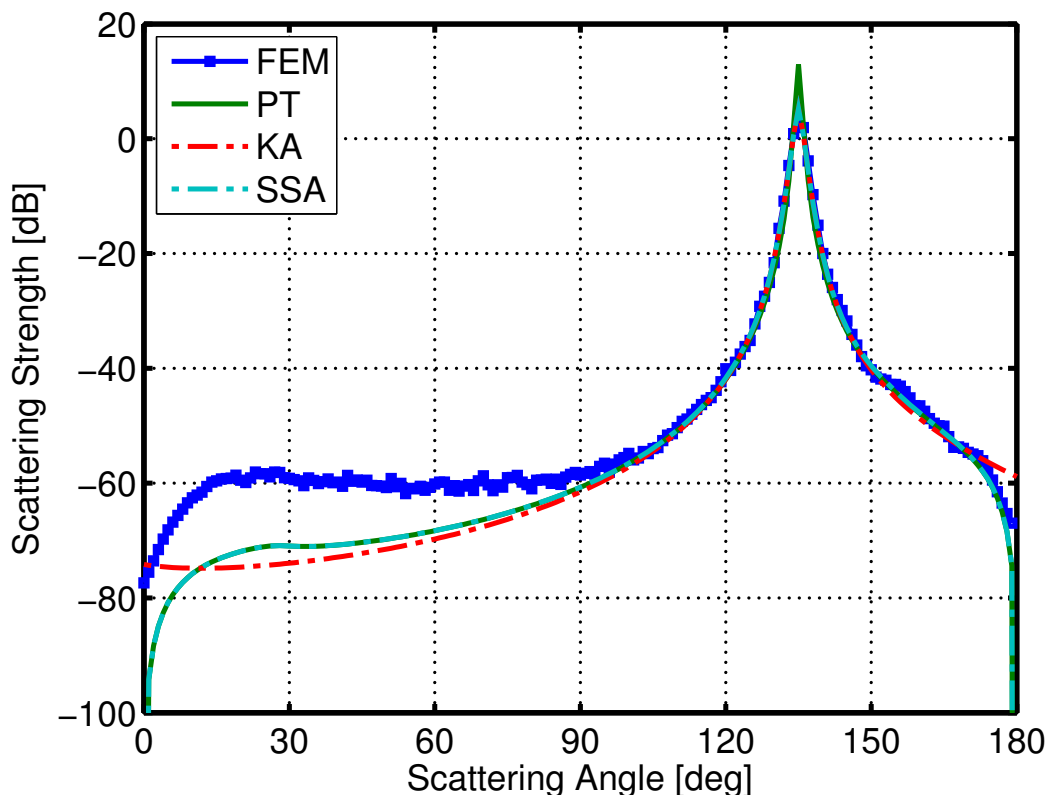


Figure 6.7: Comparison of finite element (FEM) bistatic scattering results with perturbation theory (PT), the Kirchhoff approximation (KA), and the small-slope approximation (SSA) for the following parameters:  $\theta = 45^\circ$ ,  $f = 3$  kHz,  $w_1 = 6.3662 \times 10^{-8} \text{ cm}^{3-\gamma_1}$ ,  $\gamma_1 = 4$ ,  $K_0 = 0.001 \text{ cm}^{-1}$  ( $k_a h = 1.26$ ).

FEM and SSA reaching as much as 20 dB. As in the monostatic case, the reason the disparity is so great for these particular parameters is unknown at this time. In Figure 6.8,  $k_a h = 12.57$  and FEM is in surprisingly good agreement with PT for scattering angles far from specular, KA for scattering angles near specular, and SSA at all scattering angles. While the FEM and SSA results are within 2 dB for most scattering angles, the disparity between



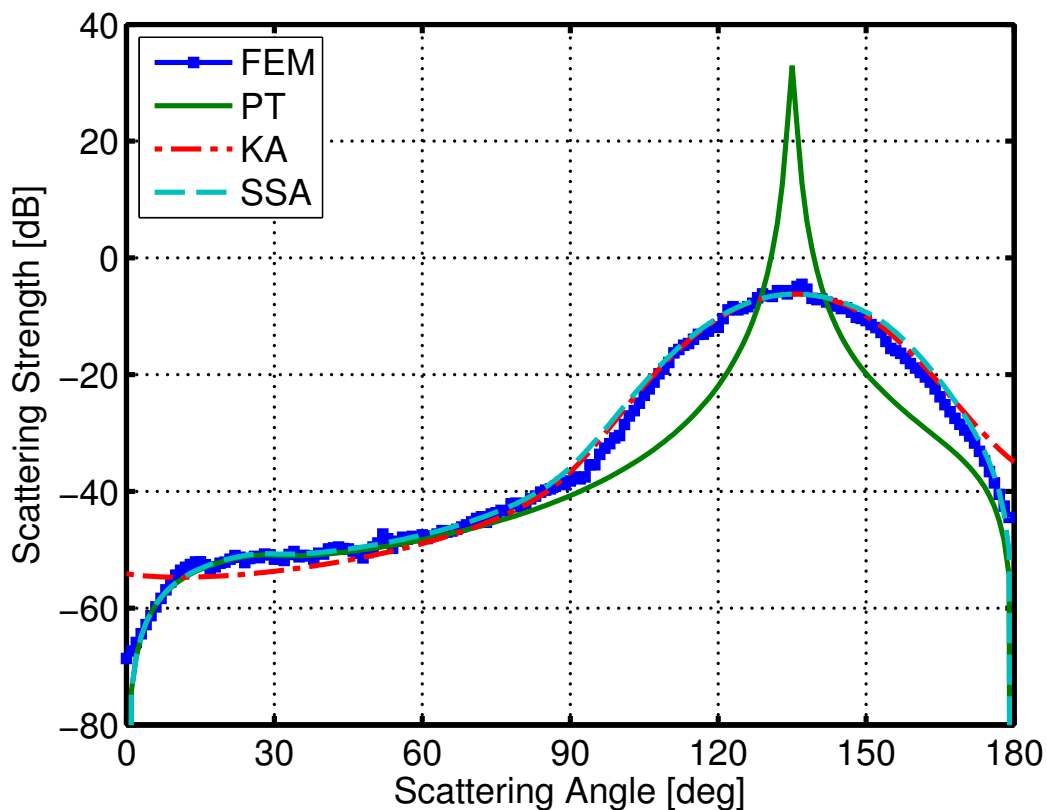


Figure 6.8: Comparison of finite element (FEM) bistatic scattering results with perturbation theory (PT), the Kirchhoff approximation (KA), and the small-slope approximation (SSA) for the following parameters:  $\theta = 45^\circ$ ,  $f = 3$  kHz,  $w_1 = 6.3662 \times 10^{-6} \text{ cm}^{3-\gamma_1}$ ,  $\gamma_1 = 4$ ,  $K_0 = 0.001 \text{ cm}^{-1}$  ( $k_a h = 12.57$ ).

the two models reaches as much as 4 dB for scattering angles between  $90^\circ$  and  $105^\circ$ .

### 6.1.2 Comparison with FEM Fluid Models

The same poroelastic finite element results compared with the three analytic models above are now compared with the scattering strengths found

Table 6.3: Fluid model parameters for study 1

Parameter	Value at 100 Hz	Value at 3 kHz
Simple fluid sound speed ( $c_{sf}$ )	1640.4 m/s	1732.7 m/s
Simple fluid density ( $\rho_{sf}$ )	2056.5 kg/m <sup>3</sup>	2056.5 kg/m <sup>3</sup>
Simple fluid attenuation ( $\alpha_{sf\lambda}$ )	0.28 dB/ $\lambda$	1.63 dB/ $\lambda$
EDFM sound speed ( $c_{EDFM}$ )	1630.6 m/s	1728.3 m/s
EDFM density ( $\rho_{EDFM}$ )	2055.1-20.0 <i>i</i> kg/m <sup>3</sup>	1827.6-112.3 <i>i</i> kg/m <sup>3</sup>
EDFM attenuation ( $\alpha_{EDFM\lambda}$ )	0.27 dB/ $\lambda$	1.68 dB/ $\lambda$

using finite element models where the sediment is considered a fluid. Two fluid models are considered. The first is a simple fluid model where the fluid's sound speed is set equal to the fast wave's speed and the fluid's density is set equal to the average density of the poroelastic material (see Eqs. C.1 and C.4). The second is the so-called effective density fluid model (EDFM) developed by Williams in [5] that is designed to better approximate the behavior of a poroelastic material, as given by Eqs. C.10 and C.11. More information on both of these fluid models can be found in Appendix C. For the present study, the model parameters used are given in Table 6.3.

Figures 6.9 through 6.12 show the comparison of the poroelastic, EDFM, and simple fluid FEM monostatic scattering results. In Figure 6.9,  $k_a h = 0.04$  and all three models agree very closely. For these parameters, the mean disparity between the full poroelastic and EDFM models is found to be only about 0.73 dB with a maximum disparity of about 1.7 dB occurring at  $\theta = 15^\circ$ . The simple fluid model is in similarly good agreement with the poroelastic results, with a mean disparity of only 0.69 dB and a maximum deviation of 2.3 dB at  $\theta = 35^\circ$ . In Figure 6.10,  $k_a h = 0.42$  and all three models are again in great

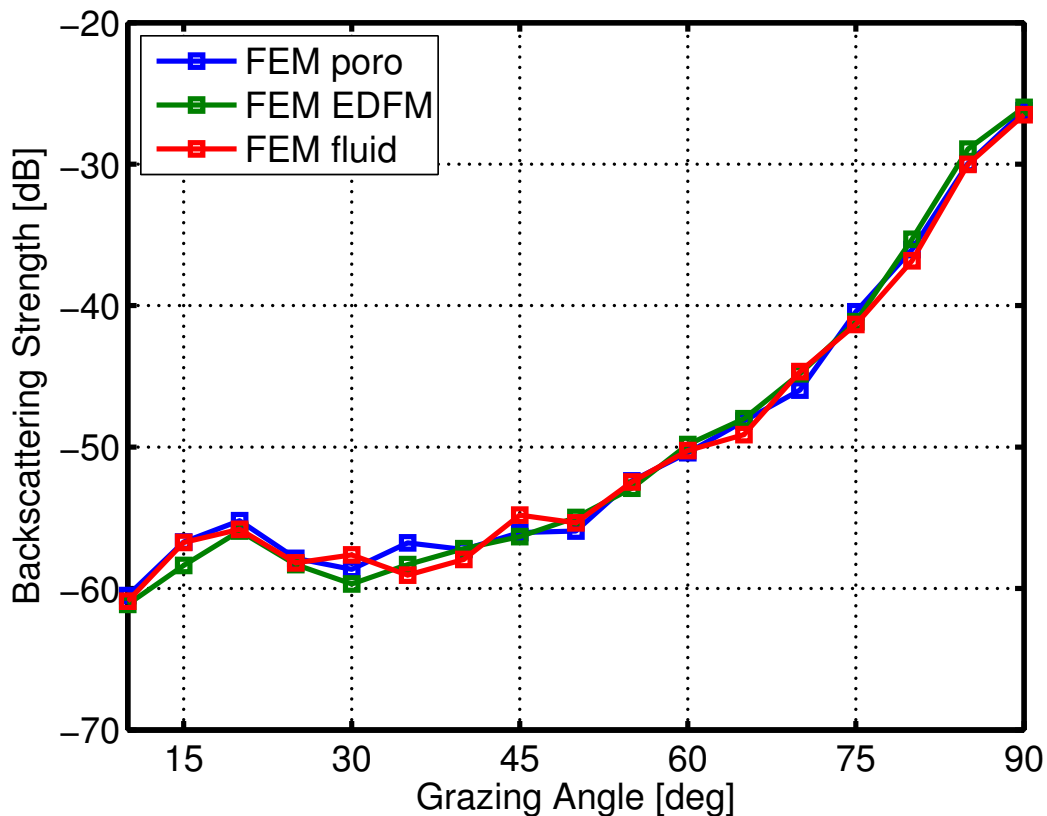


Figure 6.9: Comparison of full poroelastic finite element (FEM poro) monostatic scattering results with those of finite element models that consider the sediment to be an effective density fluid (FEM EDFM) and a simple fluid (FEM fluid) for the following parameters:  $f = 100$  Hz,  $w_1 = 6.3662 \times 10^{-8}$  cm $^{3-\gamma_1}$ ,  $\gamma_1 = 4$ ,  $K_0 = 0.001$  cm $^{-1}$  ( $k_a h = 0.04$ ).

agreement. The mean and maximum disparities between the poroelastic and EDFM results are found to be 0.51 and 1.22 dB, respectively, while the mean and maximum disparities between the poroelastic and simple fluid results are found to be 0.65 and 1.91 dB, respectively. In Figure 6.11,  $k_a h = 1.26$  and all three models are still in good agreement. While the mean disparity between

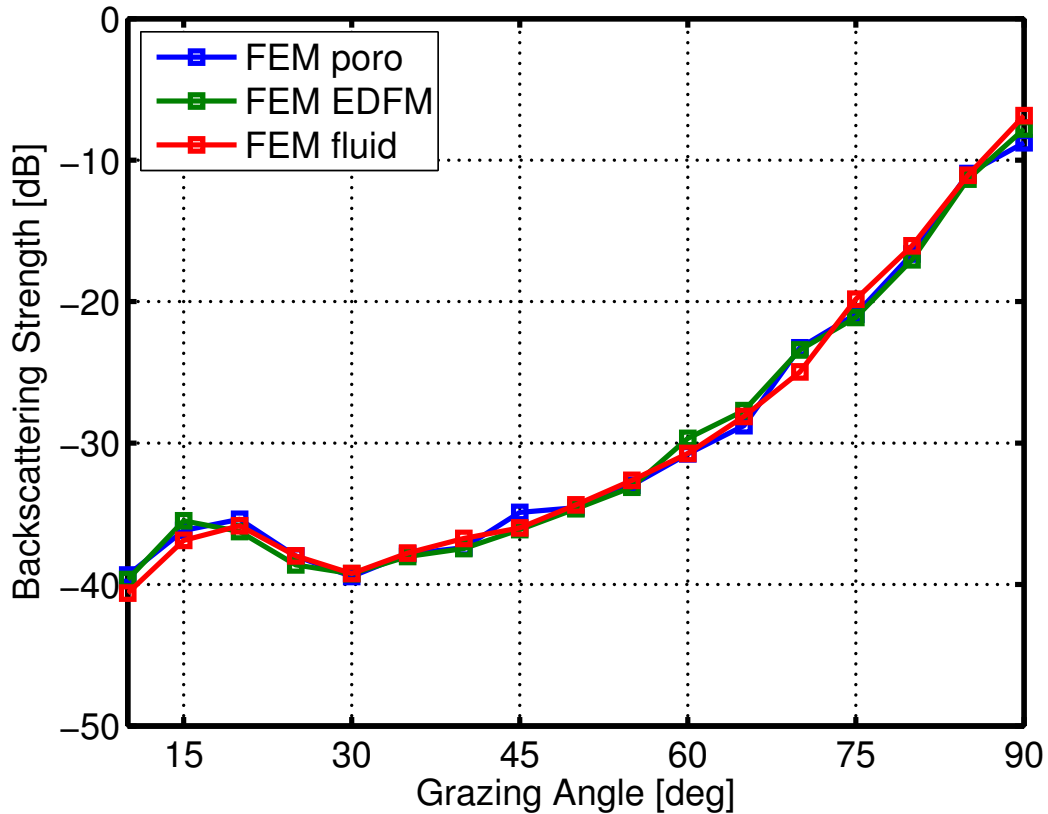


Figure 6.10: Comparison of full poroelastic finite element (FEM poro) monostatic scattering results with those of finite element models that consider the sediment to be an effective density fluid (FEM EDFM) and a simple fluid (FEM fluid) for the following parameters:  $f = 100$  Hz,  $w_1 = 6.3662 \times 10^{-6}$  cm $^{3-\gamma_1}$ ,  $\gamma_1 = 4$ ,  $K_0 = 0.001$  cm $^{-1}$  ( $k_a h = 0.42$ ).

the poroelastic and EDFM results is still below 1 dB, the mean difference between the poroelastic and simple fluid results is now about 1.4 dB. Still both models are within 3 dB of the poroelastic model for all grazing angles. In Figure 6.12,  $k_a h = 12.57$  and, with a mean disparity of 1.22 dB versus 1.27 dB, the simple fluid model is actually in better agreement with the poroelastic

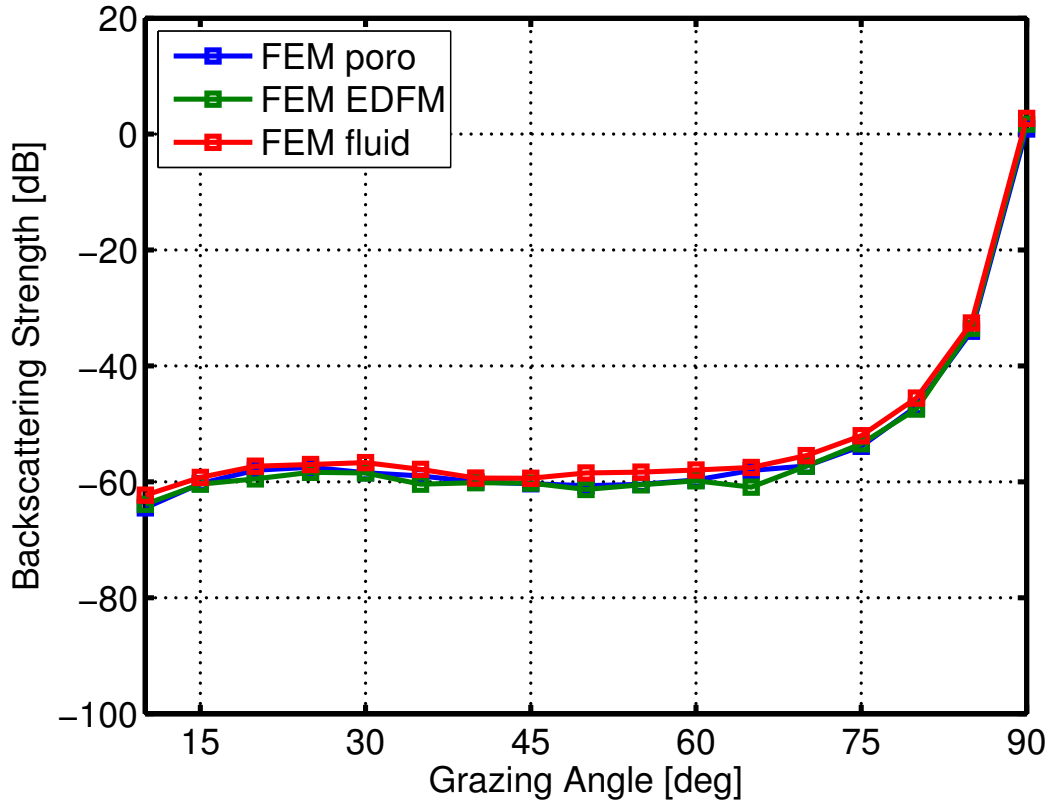


Figure 6.11: Comparison of full poroelastic finite element (FEM poro) monostatic scattering results with those of finite element models that consider the sediment to be an effective density fluid (FEM EDFM) and a simple fluid (FEM fluid) for the following parameters:  $f = 3$  kHz,  $w_1 = 6.3662 \times 10^{-8}$  cm $^{3-\gamma_1}$ ,  $\gamma_1 = 4$ ,  $K_0 = 0.001$  cm $^{-1}$  ( $k_a h = 1.26$ ).

model than the EDFM. However, in actuality, both models probably perform about the same, and the mean disparity of the EDFM and poroelastic results is most likely influenced by the very large disparity of 5.4 dB that occurs at  $\theta = 70^\circ$ .

The comparison of the poroelastic, EDFM, and simple fluid FEM bistatic

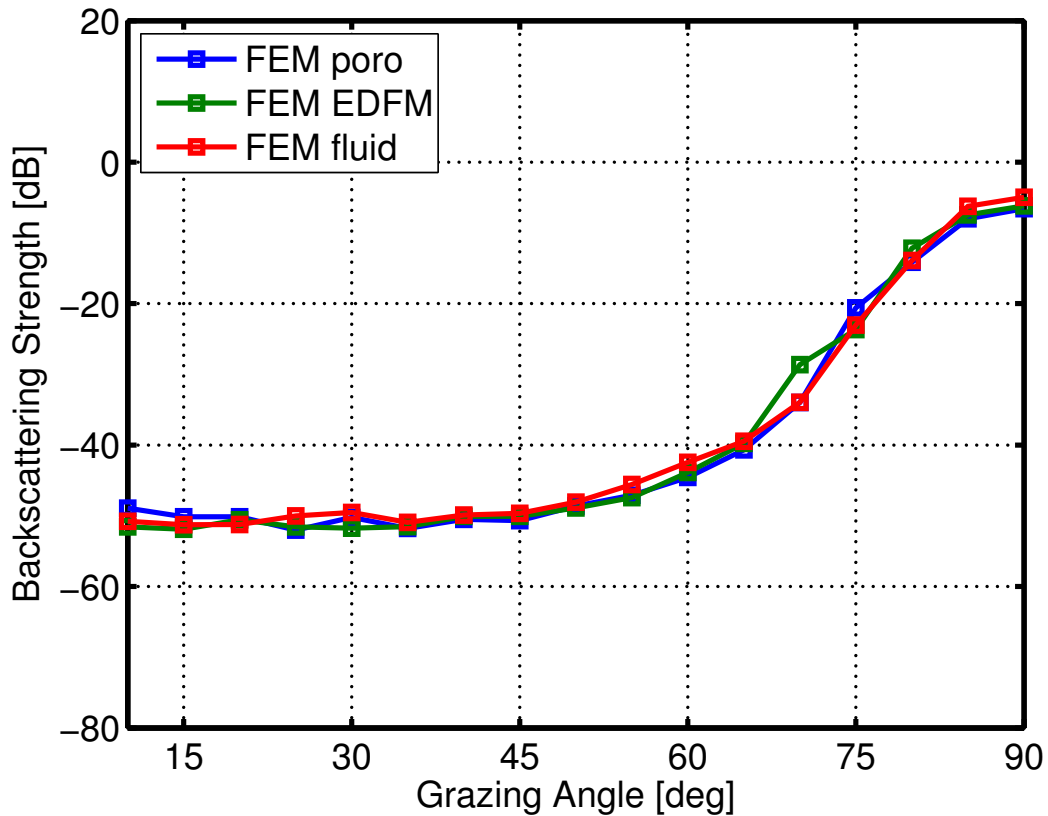


Figure 6.12: Comparison of full poroelastic finite element (FEM poro) monostatic scattering results with those of finite element models that consider the sediment to be an effective density fluid (FEM EDFM) and a simple fluid (FEM fluid) for the following parameters:  $f = 3$  kHz,  $w_1 = 6.3662 \times 10^{-6}$  cm $^{3-\gamma_1}$ ,  $\gamma_1 = 4$ ,  $K_0 = 0.001$  cm $^{-1}$  ( $k_a h = 12.57$ ).

scattering results are shown in Figures 6.13 through 6.16. In Figure 6.13,  $k_a h = 0.04$  and the results of both fluid models differ from the poroelastic results by no more than about 3 dB. The mean disparity of both fluid models from the poroelastic model is about 0.7 dB in both cases. Similar agreement between both fluid models and the poroelastic model is seen in Figure 6.14

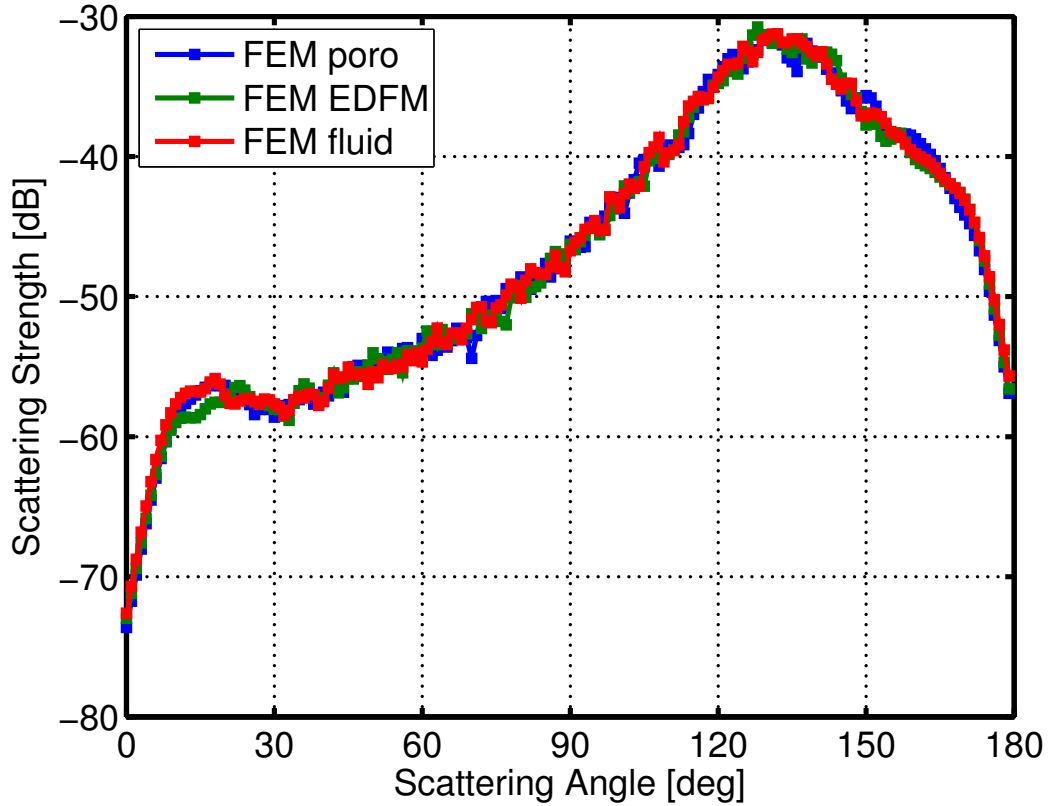


Figure 6.13: Comparison of full poroelastic finite element (FEM poro) bistatic scattering results with those of finite element models that consider the sediment to be an effective density fluid (FEM EDFM) and a simple fluid (FEM fluid) for the following parameters:  $\theta = 45^\circ$ ,  $f = 100$  Hz,  $w_1 = 6.3662 \times 10^{-8}$  cm $^{3-\gamma_1}$ ,  $\gamma_1 = 4$ ,  $K_0 = 0.001$  cm $^{-1}$  ( $k_a h = 0.04$ ).

for the case of  $k_a h = 0.42$ . In Figure 6.15,  $k_a h = 1.26$  and all three models are still in reasonably good agreement. The mean disparity of the EDFM and poroelastic results is still below 1 dB while the average difference between the simple fluid and poroelastic results has grown to about 1.25 dB. In Figure 6.16,  $k_a h = 12.57$  and the fluid models are in reasonable agreement with the poroe-

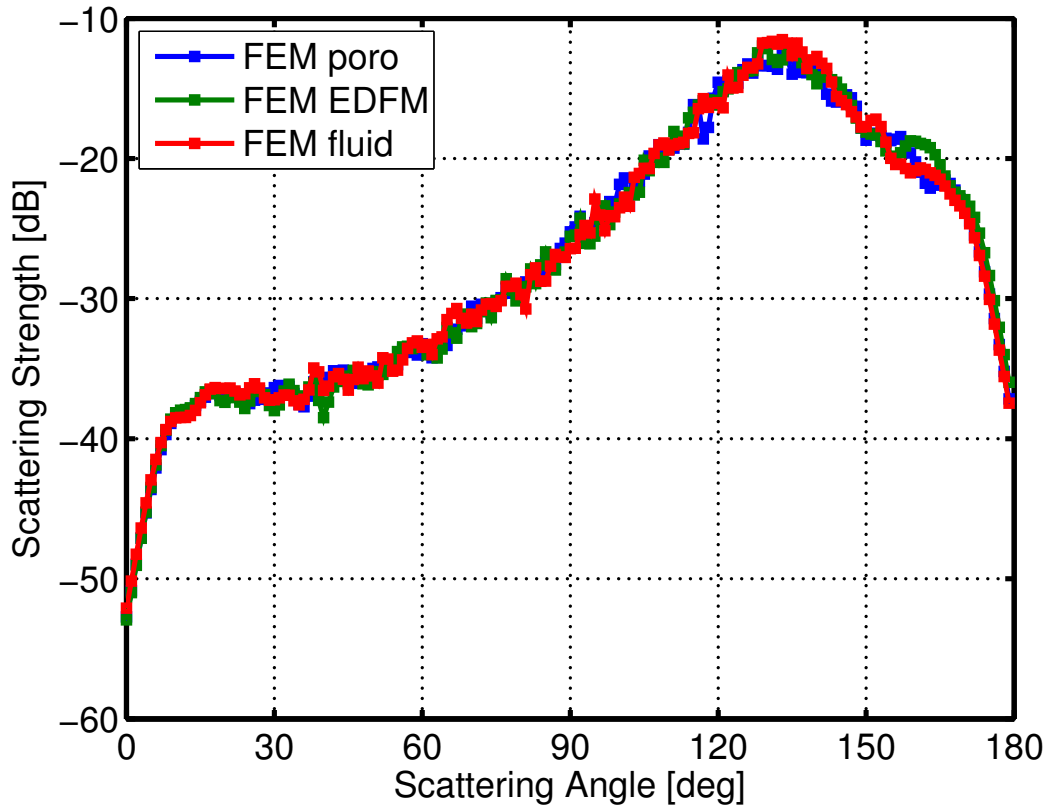


Figure 6.14: Comparison of full poroelastic finite element (FEM poro) bistatic scattering results with those of finite element models that consider the sediment to be an effective density fluid (FEM EDFM) and a simple fluid (FEM fluid) for the following parameters:  $\theta = 45^\circ$ ,  $f = 100$  Hz,  $w_1 = 6.3662 \times 10^{-6}$  cm $^{3-\gamma_1}$ ,  $\gamma_1 = 4$ ,  $K_0 = 0.001$  cm $^{-1}$  ( $k_a h = 0.42$ ).

lastic results, with the difference between the poroelastic and EDFM results not exceeding 4.5 dB and the deviation between the poroelastic and simple fluid results not exceeding 6.13 dB. On average, the disparity between the two fluid models and the poroelastic model is between 1 and 2 dB.



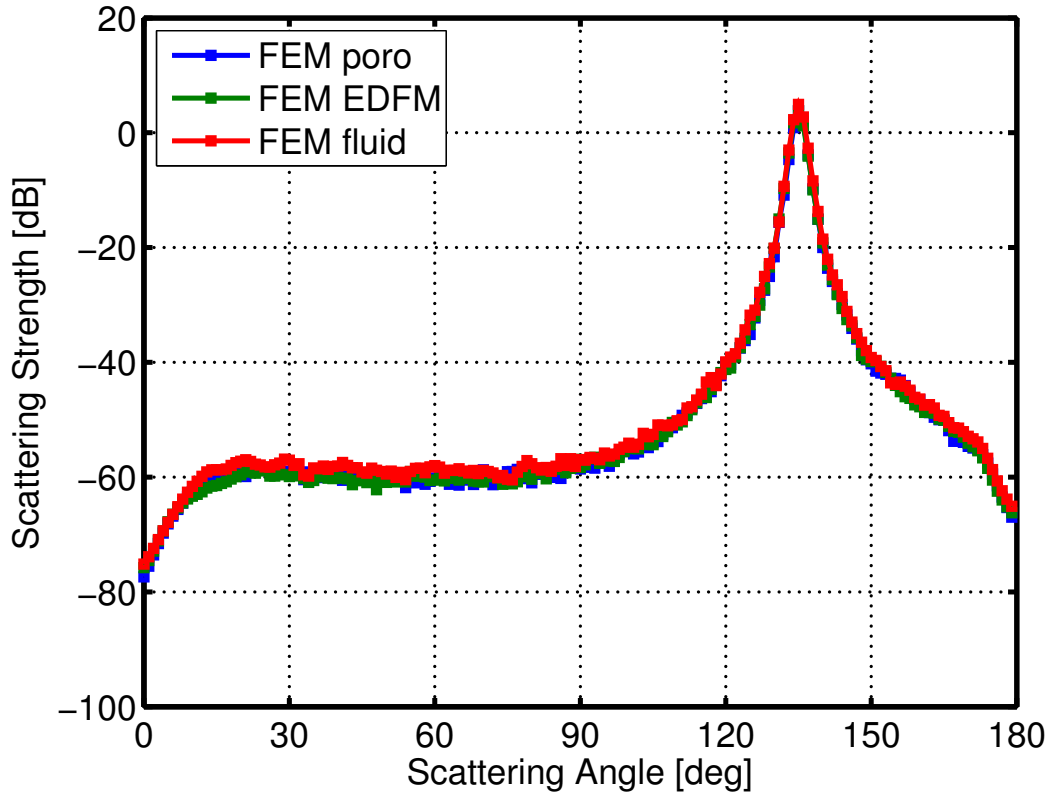


Figure 6.15: Comparison of full poroelastic finite element (FEM poro) bistatic scattering results with those of finite element models that consider the sediment to be an effective density fluid (FEM EDFM) and a simple fluid (FEM fluid) for the following parameters:  $\theta = 45^\circ$ ,  $f = 3$  kHz,  $w_1 = 6.3662 \times 10^{-8}$  cm $^{3-\gamma_1}$ ,  $\gamma_1 = 4$ ,  $K_0 = 0.001$  cm $^{-1}$  ( $k_a h = 1.26$ ).

## 6.2 Study 2: Following Williams et al. (2001)

The parameters used in the second numerical study follow those used by Williams, Grochocinski, and Jackson in [10]. The material properties and roughness parameters are listed in Tables 6.4 and 6.5. It must be noted that, since the rough surfaces considered in [10] are two-dimensional, the equivalent

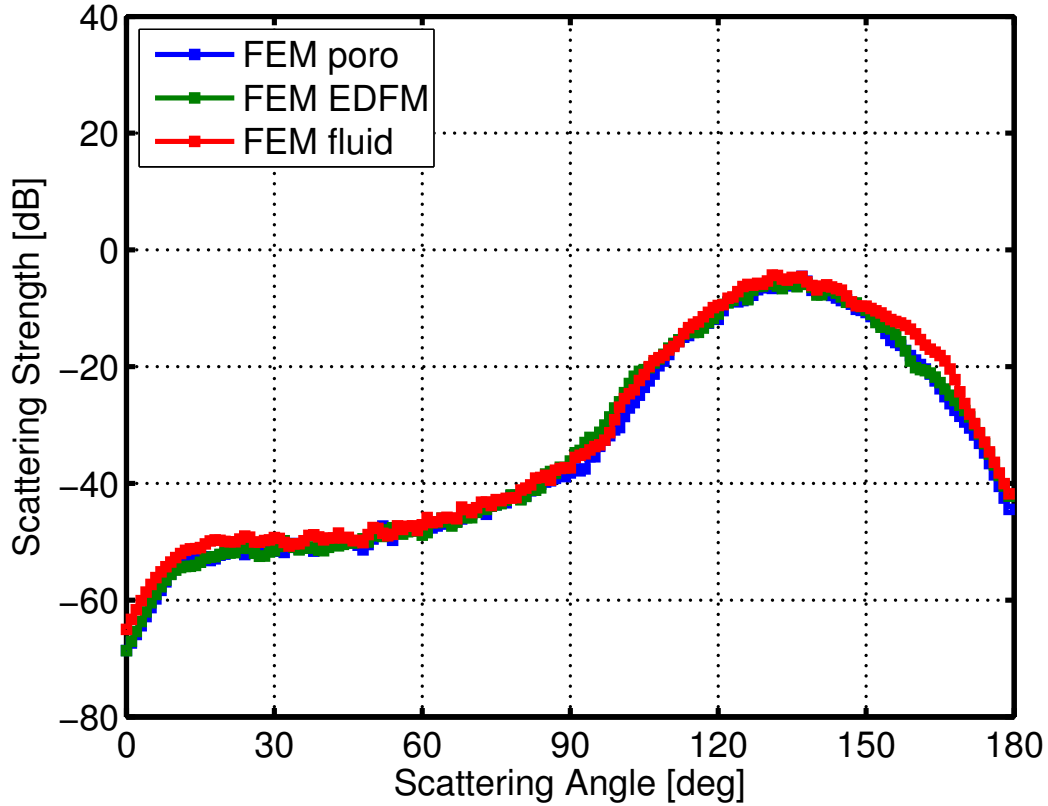


Figure 6.16: Comparison of full poroelastic finite element (FEM poro) bistatic scattering results with those of finite element models that consider the sediment to be an effective density fluid (FEM EDFM) and a simple fluid (FEM fluid) for the following parameters:  $\theta = 45^\circ$ ,  $f = 3$  kHz,  $w_1 = 6.3662 \times 10^{-6}$  cm $^{3-\gamma_1}$ ,  $\gamma_1 = 4$ ,  $K_0 = 0.001$  cm $^{-1}$  ( $k_a h = 12.57$ ).

one-dimensional spectral strength and spectral exponent listed in Table 6.5 must be found using Eqs. 4.23 and 4.24. Also, a true power-law roughness spectrum is used in [10], so the cut-off wavenumber used in the present study was chosen somewhat arbitrarily. For each frequency, finite element models of fifty rough surface realizations are solved. As in [10], only monostatic scat-

Table 6.4: Material properties following [10]

<b>Parameter</b>	<b>Value</b>
Porosity ( $\beta$ )	0.40
Sediment grain density ( $\rho_s$ )	2650 kg/m <sup>3</sup>
Pore fluid density ( $\rho_f$ )	1000 kg/m <sup>3</sup>
Sediment grain bulk modulus ( $K_r$ )	36.6 GPa
Pore fluid bulk modulus ( $K_f$ )	2.25 GPa
Permeability ( $\kappa$ )	100 $\mu\text{m}^2$
Pore fluid viscosity ( $\eta$ )	0.001 kg/m-s
Tortuosity ( $\tau$ )	1.25
Pore size parameter ( $a$ )	50 $\mu\text{m}$
Frame shear modulus ( $\mu$ )	26 MPa
Shear log decrement ( $\delta_\mu$ )	0.151
Frame bulk modulus ( $K_b$ )	44 MPa
Frame log decrement ( $\delta_K$ )	0.143
Acoustic fluid density ( $\rho_a$ )	1000 kg/m <sup>3</sup>
Acoustic fluid sound speed ( $c_a$ )	1500 m/s

Table 6.5: Roughness parameters adapted from [10]

<b>Parameter</b>	<b>Value(s)</b>
Frequencies ( $f$ )	0.1, 1, 10, and 100 kHz
Spectral strength ( $w_1$ )	0.0078 cm <sup>3-<math>\gamma_1</math></sup>
Spectral exponent ( $\gamma_1$ )	2.05
Cutoff wavenumber ( $K_0$ )	0.008 cm <sup>-1</sup>

tering strengths are calculated. As in the monostatic results of the previous study, the finite element backscattering strengths are calculated every 5° for grazing angles ranging from 10° to 90°. For the material properties given in Table 6.4, the characteristic frequency can be calculated to be around 63.7 Hz using Eq. 3.10; this means that the Biot model is in the high-frequency regime for all four frequency values considered.

### 6.2.1 Comparison with Analytic Scattering Models

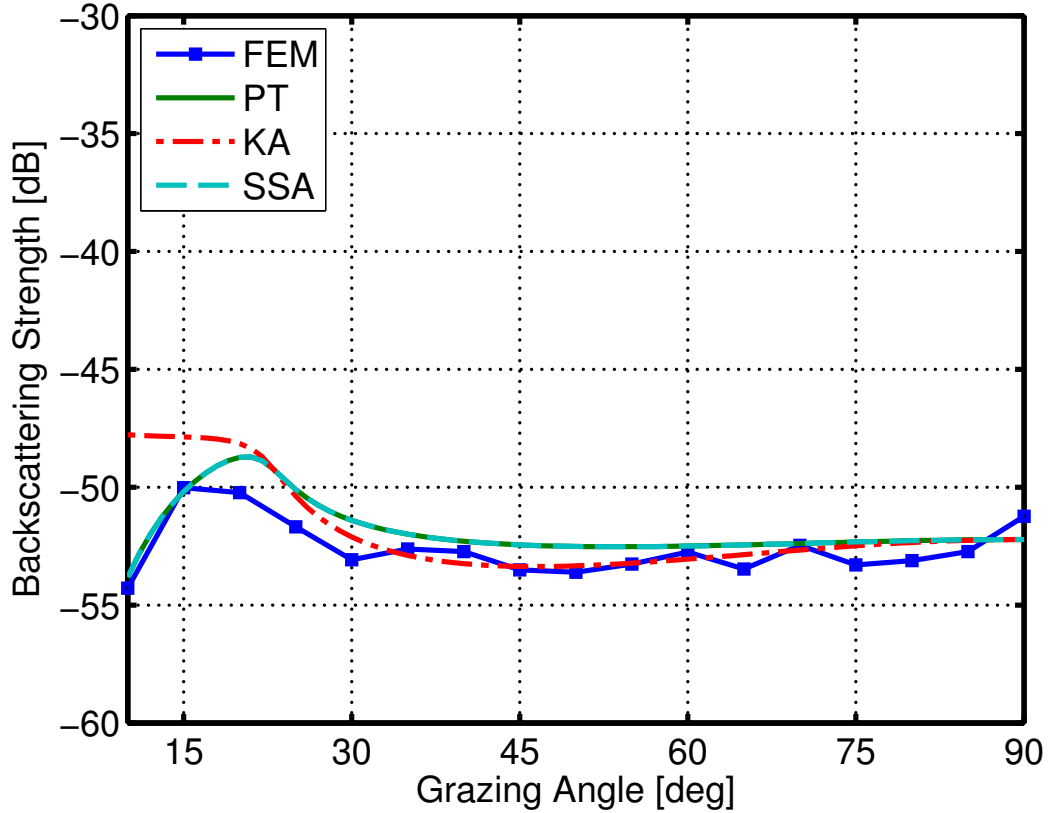


Figure 6.17: Comparison of finite element (FEM) monostatic scattering results with perturbation theory (PT), the Kirchhoff approximation (KA), and the small-slope approximation (SSA) for the following parameters:  $f = 100$  Hz,  $w_1 = 0.0078 \text{ cm}^{3-\gamma_1}$ ,  $\gamma_1 = 2.05$ ,  $K_0 = 0.008 \text{ cm}^{-1}$  ( $k_a h = 0.008$ ).

As in the previous study, the backscattering strengths found using the finite element method are compared with those calculated using perturbation theory, the Kirchhoff approximation, and the small-slope approximation in Figures 6.17 through 6.20. In Figure 6.17,  $k_a h = 0.008$  and the fluid-poroelastic interface is therefore nearly flat. The backscattering strengths pre-

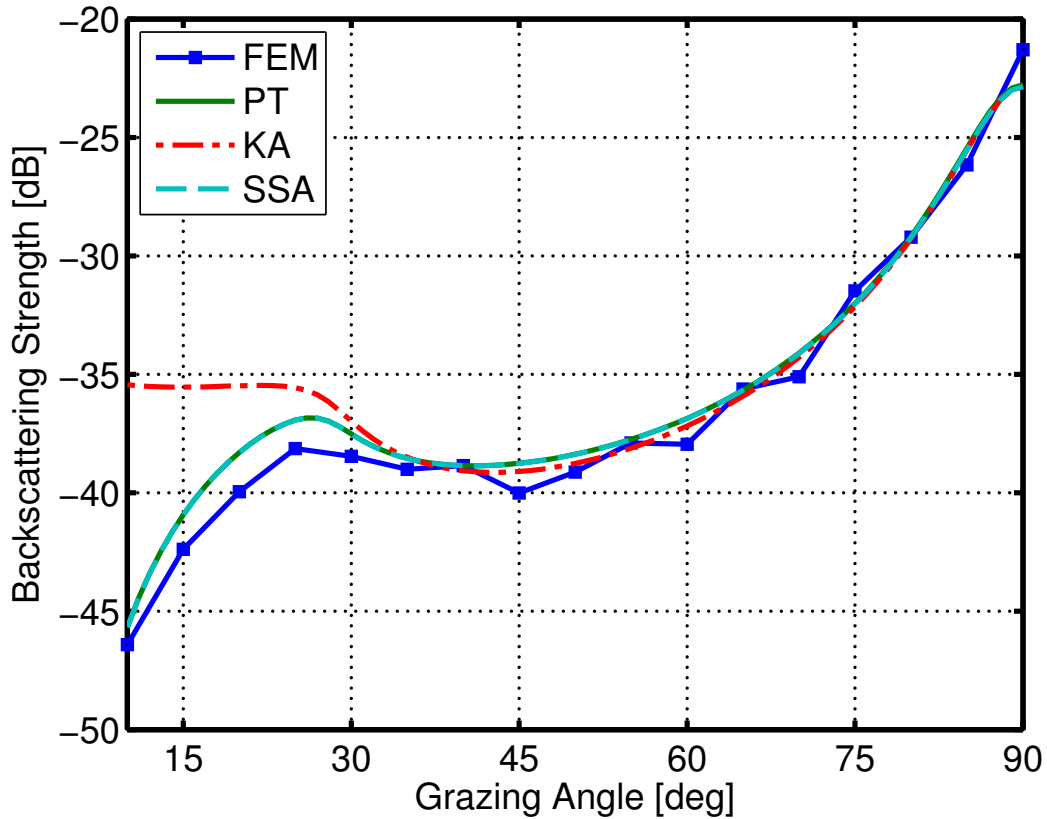


Figure 6.18: Comparison of finite element (FEM) monostatic scattering results with perturbation theory (PT), the Kirchhoff approximation (KA), and the small-slope approximation (SSA) for the following parameters:  $f = 1$  kHz,  $w_1 = 0.0078 \text{ cm}^{3-\gamma_1}$ ,  $\gamma_1 = 2.05$ ,  $K_0 = 0.008 \text{ cm}^{-1}$  ( $k_a h = 0.081$ ).

dicted by all three analytic models are within 2 dB of the FEM results for all grazing angles with the expected exception of KA for shallow grazing angles. For grazing angles greater than  $30^\circ$ , KA is seemingly in better agreement with FEM than PT and SSA, with the deviation between the scattering strengths of KA and FEM not exceeding 1 dB. As expected, PT and SSA agree exactly everywhere and provide a better match with the FEM results for the shal-

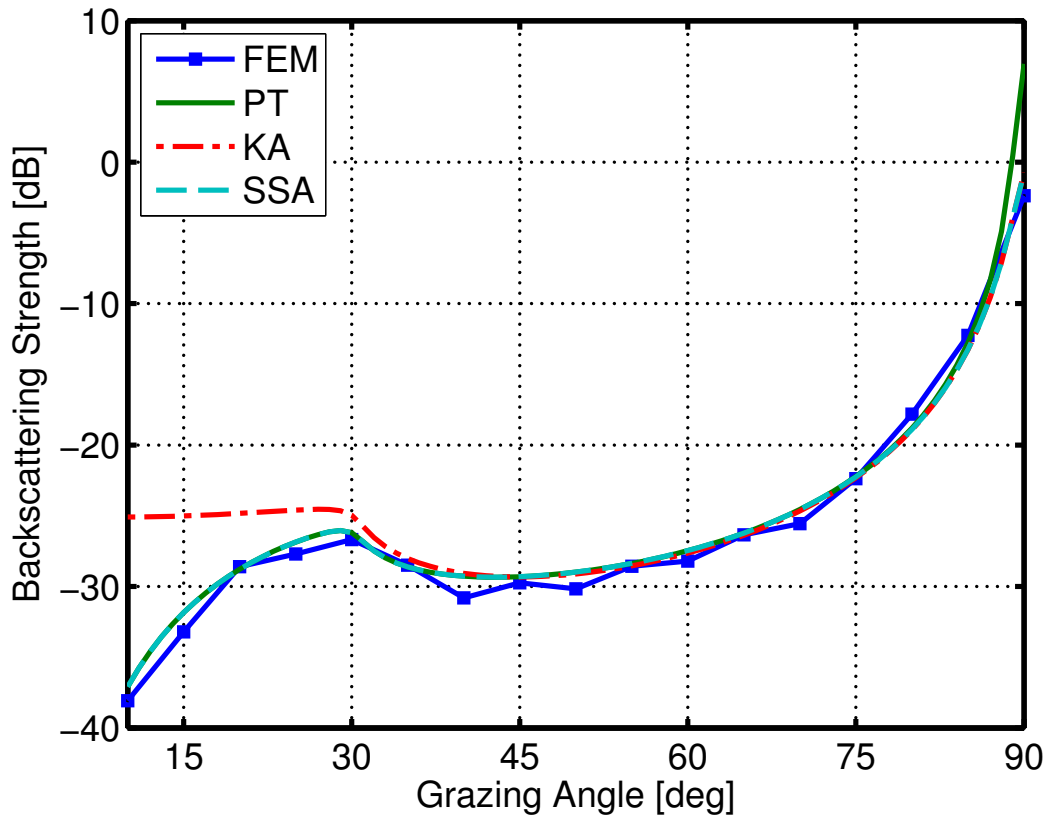


Figure 6.19: Comparison of finite element (FEM) monostatic scattering results with perturbation theory (PT), the Kirchhoff approximation (KA), and the small-slope approximation (SSA) for the following parameters:  $f = 10$  kHz,  $w_1 = 0.0078 \text{ cm}^{3-\gamma_1}$ ,  $\gamma_1 = 2.05$ ,  $K_0 = 0.008 \text{ cm}^{-1}$  ( $k_a h = 0.813$ ).

lowest grazing angles considered. In Figure 6.18,  $k_a h = 0.081$  and all three analytic models are still comfortably within their respective regions of validity. Here, PT and SSA still match exactly and predict scattering strengths within 2 dB of those calculated using FEM at all grazing angles. As expected, KA converges with PT and SSA as the grazing angle approaches normal, and the results all three analytic models are within about 1 dB of the FEM results for

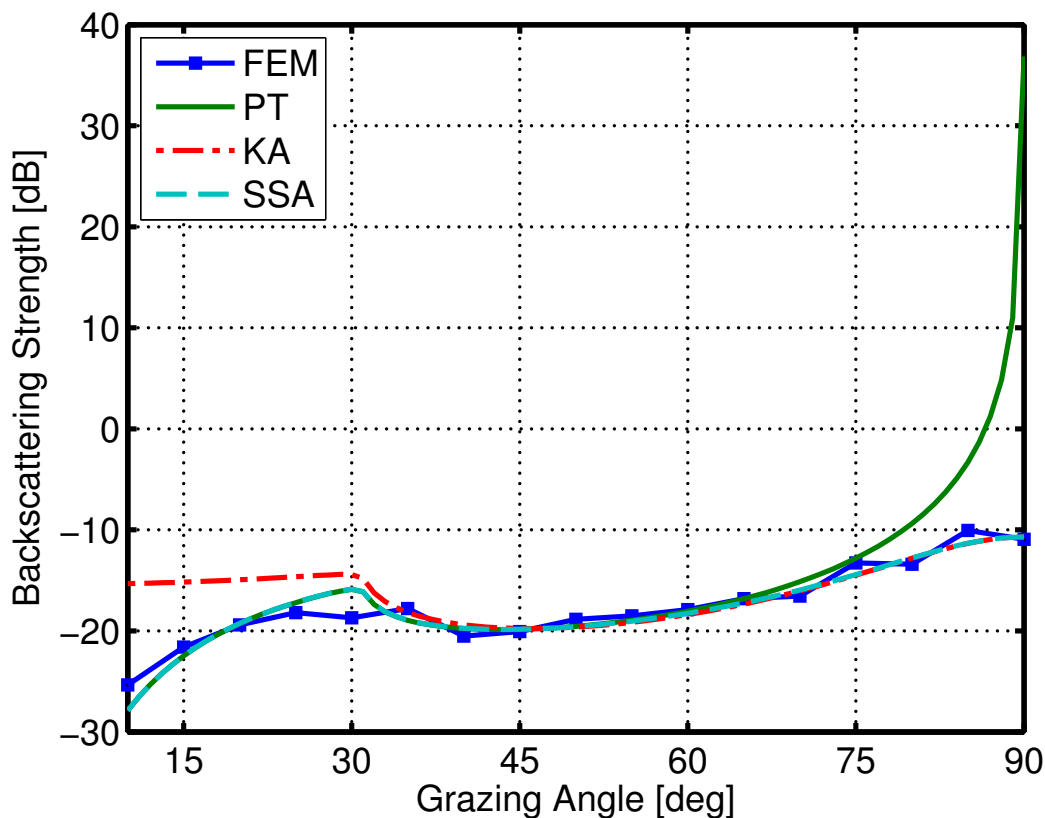


Figure 6.20: Comparison of finite element (FEM) monostatic scattering results with perturbation theory (PT), the Kirchhoff approximation (KA), and the small-slope approximation (SSA) for the following parameters:  $f = 100$  kHz,  $w_1 = 0.0078 \text{ cm}^{3-\gamma_1}$ ,  $\gamma_1 = 2.05$ ,  $K_0 = 0.008 \text{ cm}^{-1}$  ( $k_a h = 8.134$ ).

grazing angles greater than  $30^\circ$  with the exceptions of  $\theta = 45^\circ$  and  $\theta = 90^\circ$ .

In Figure 6.19,  $k_a h = 0.813$  and it is unknown *a priori* how well the analytic models will match FEM. Somewhat surprisingly, the agreement between the analytic results and FEM is similar to the previous case other than the fact that PT now diverges from FEM as the grazing angle approaches normal incidence. For this reason, SSA undoubtedly provides the best match

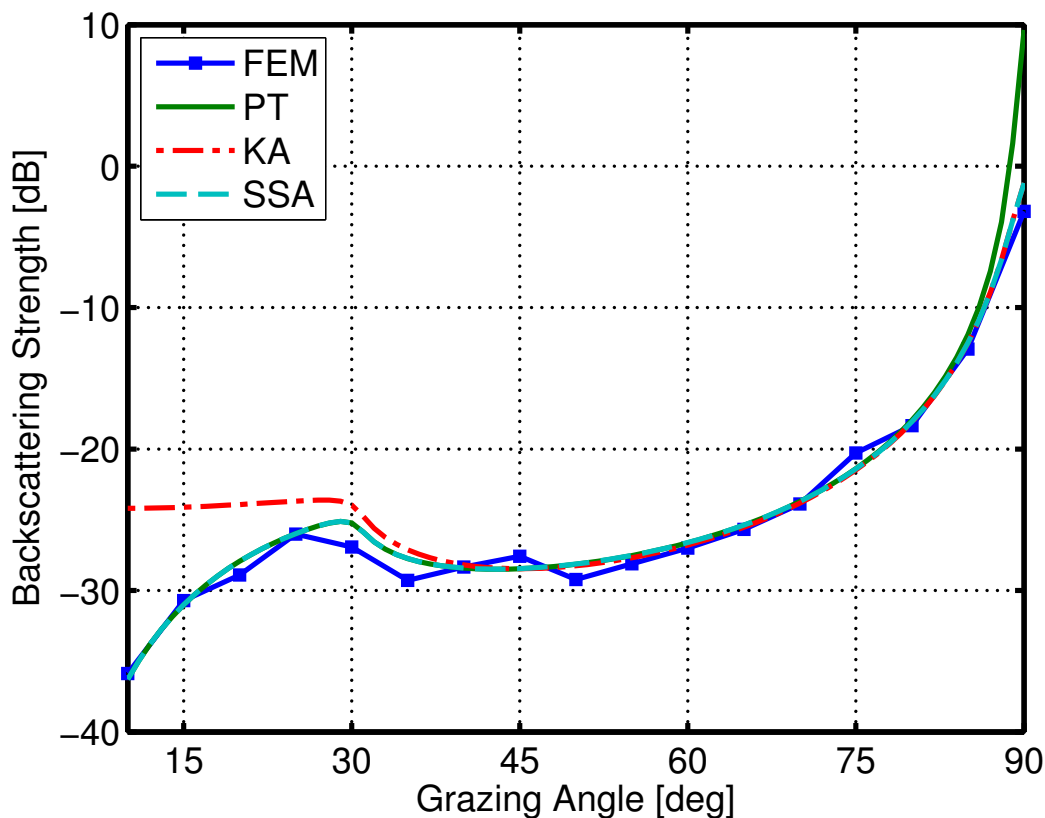


Figure 6.21: Comparison of finite element (FEM) monostatic scattering results with perturbation theory (PT), the Kirchhoff approximation (KA), and the small-slope approximation (SSA) for the following parameters:  $f = 12.295$  kHz,  $w_1 = 0.0078 \text{ cm}^{3-\gamma_1}$ ,  $\gamma_1 = 2.05$ ,  $K_0 = 0.008 \text{ cm}^{-1}$  ( $k_a h = 1$ ).

with FEM, agreeing within 1 dB at all grazing angles except  $\theta = 40^\circ$ , where the disparity is still only around 1.3 dB. In Figure 6.20,  $k_a h$  is considerably greater than 1 at  $k_a h = 8.134$  and none of the analytic models are expected to perform well. Still, the SSA results agree with those of FEM to within 3 dB at all grazing angles, and, in the region where PT, KA, and SSA are all in close agreement, the deviation of any one model from FEM is bounded by 1.5



dB.

In addition to the frequencies listed in Table 6.5, finite element models where  $f = 12.295$  kHz are solved in order to further investigate the great disparity between FEM and the analytic models seen in Figures 6.3 and 6.7. At this frequency,  $k_a h = 1$  and excellent agreement is found between FEM and SSA at all grazing angles, with the disparity between the two models not exceeding 2 dB. It can therefore be concluded that the disparities seen in Figures 6.3 and 6.7 are not due to the  $k_a h$  value being near 1 and an alternate explanation must be sought.

Table 6.6: Fluid model parameters for study 2

<b>Parameter</b>	<b>Value at 100 Hz</b>	<b>Value at 1 kHz</b>
Simple fluid sound speed ( $c_{sf}$ )	1623.3 m/s	1700.5 m/s
Simple fluid density ( $\rho_{sf}$ )	1990 kg/m <sup>3</sup>	1990 kg/m <sup>3</sup>
Simple fluid attenuation ( $\alpha_{sf\lambda}$ )	0.77 dB/ $\lambda$	1.37 dB/ $\lambda$
EDFM sound speed ( $c_{EDFM}$ )	1613.5 m/s	1694.9 m/s
EDFM density ( $\rho_{EDFM}$ )	1975-57.5 <i>i</i> kg/m <sup>3</sup>	1789.1-92.7 <i>i</i> kg/m <sup>3</sup>
EDFM attenuation ( $\alpha_{EDFM\lambda}$ )	0.79 dB/ $\lambda$	1.41 dB/ $\lambda$
<b>Parameter</b>	<b>Value at 10 kHz</b>	<b>Value at 100 kHz</b>
Simple fluid sound speed ( $c_{sf}$ )	1739 m/s	1751.3 m/s
Simple fluid density ( $\rho_{sf}$ )	1990 kg/m <sup>3</sup>	1990 kg/m <sup>3</sup>
Simple fluid attenuation ( $\alpha_{sf\lambda}$ )	0.53 dB/ $\lambda$	0.18 dB/ $\lambda$
EDFM sound speed ( $c_{EDFM}$ )	1733.6 m/s	1746.2 m/s
EDFM density ( $\rho_{EDFM}$ )	1711-33.6 <i>i</i> kg/m <sup>3</sup>	1686.6-11.0 <i>i</i> kg/m <sup>3</sup>
EDFM attenuation ( $\alpha_{EDFM\lambda}$ )	0.54 dB/ $\lambda$	0.18 dB/ $\lambda$

### 6.2.2 Comparison with FEM Fluid Models

In Figures 6.22 through 6.25, the poroelastic finite element results compared with the three analytic models above are compared with finite element

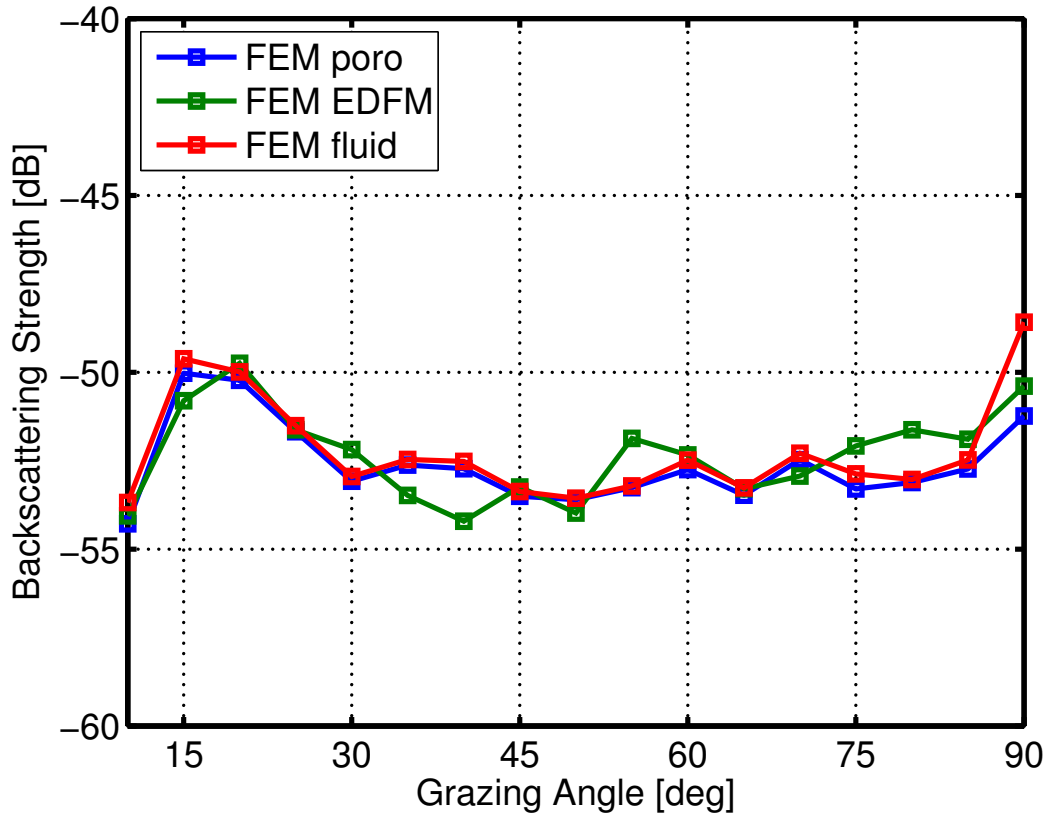


Figure 6.22: Comparison of full poroelastic finite element (FEM poro) monostatic scattering results with those of finite element models that consider the sediment to be an effective density fluid (FEM EDFM) and a simple fluid (FEM fluid) for the following parameters:  $f = 100$  Hz,  $w_1 = 0.0078 \text{ cm}^{3-\gamma_1}$ ,  $\gamma_1 = 2.05$ ,  $K_0 = 0.008 \text{ cm}^{-1}$  ( $k_a h = 0.008$ ).

results where the sediment is modeled as a simple fluid and using the EDFM. The fluid model parameters used in this study are given in Table 6.6. In Figure 6.22,  $k_a h = 0.008$  and the results of both fluid models agree with those of the poroelastic model within 1.5 dB at all grazing angles other than  $90^\circ$ . In fact, it can be concluded that the simple fluid model outperforms the EDFM for

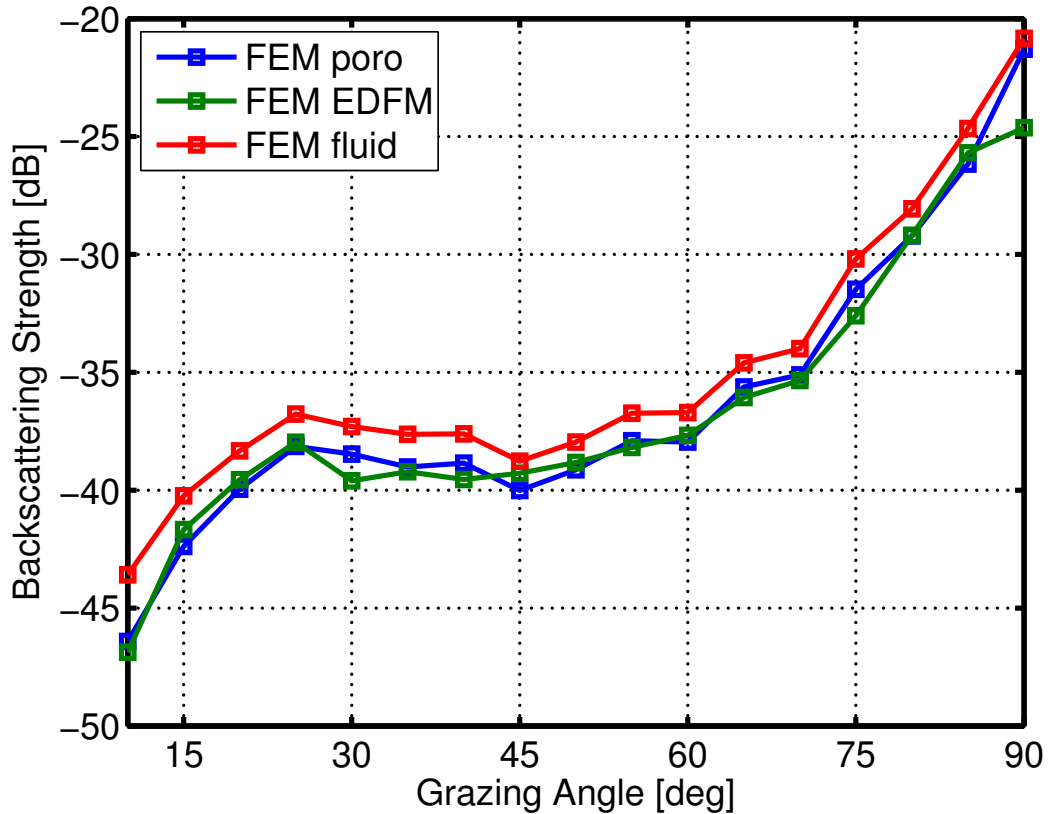


Figure 6.23: Comparison of full poroelastic finite element (FEM poro) monostatic scattering results with those of finite element models that consider the sediment to be an effective density fluid (FEM EDFM) and a simple fluid (FEM fluid) for the following parameters:  $f = 1$  kHz,  $w_1 = 0.0078$  cm $^{3-\gamma_1}$ ,  $\gamma_1 = 2.05$ ,  $K_0 = 0.008$  cm $^{-1}$  ( $k_a h = 0.081$ ).

this case.

In Figure 6.23,  $k_a h = 0.081$  and, for the first time, major discrepancies are seen between the simple fluid and poroelastic results. While the average disparity between the EDFM and poroelastic results is only 0.65 dB, the simple fluid results differ from those of the poroelastic model by more than 1 dB at all

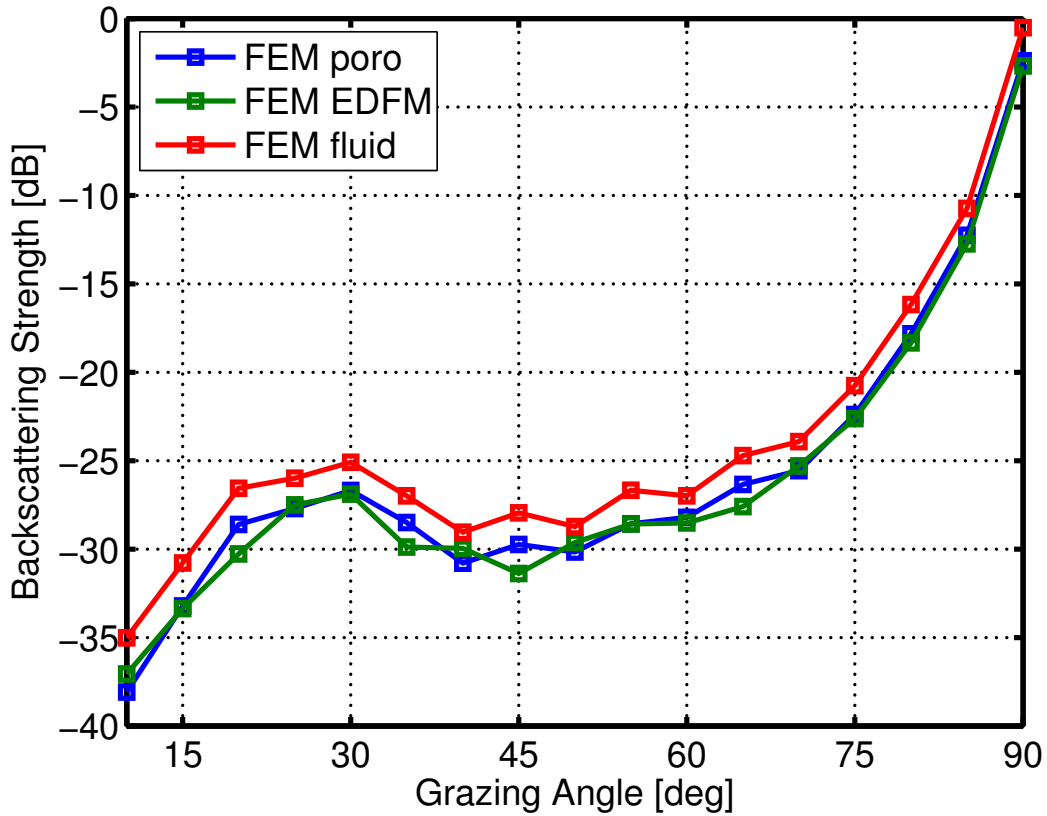


Figure 6.24: Comparison of full poroelastic finite element (FEM poro) monostatic scattering results with those of finite element models that consider the sediment to be an effective density fluid (FEM EDFM) and a simple fluid (FEM fluid) for the following parameters:  $f = 10$  kHz,  $w_1 = 0.0078$  cm<sup>3- $\gamma_1$</sup> ,  $\gamma_1 = 2.05$ ,  $K_0 = 0.008$  cm<sup>-1</sup> ( $k_a h = 0.813$ ).

grazing angles other than 90°. A similar discrepancy between the performance of the EDFM and simple fluid model is seen in Figure 6.24, where  $k_a h = 0.813$ . Here, the mean disparity between the EDFM and poroelastic model is still around 0.65 dB while that of the simple fluid and poroelastic models has grown to 1.8 dB. The EDFM continues to outperform the simple fluid

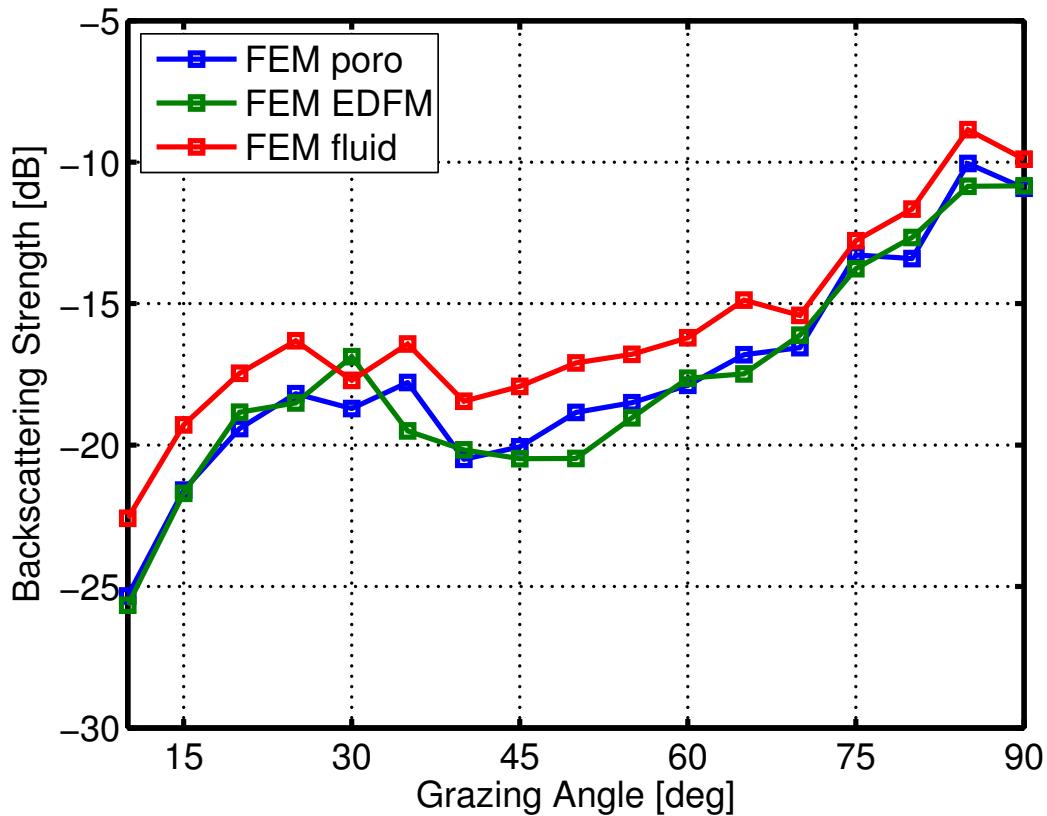


Figure 6.25: Comparison of full poroelastic finite element (FEM poro) monostatic scattering results with those of finite element models that consider the sediment to be an effective density fluid (FEM EDFM) and a simple fluid (FEM fluid) for the following parameters:  $f = 100$  kHz,  $w_1 = 0.0078$  cm $^{3-\gamma_1}$ ,  $\gamma_1 = 2.05$ ,  $K_0 = 0.008$  cm $^{-1}$  ( $k_a h = 8.134$ ).

model in Figure 6.25. In this case,  $k_a h = 8.134$  and the EDFM agrees with the poroelastic results everywhere within around 1.8 dB while the difference between the simple fluid and poroelastic results reaches as much as 2.7 dB.

From the results of this study, it can be concluded that the EDFM vastly outperforms the simple fluid model for the parameters used. In the first

study, there appeared to be no discernible difference between the performance of the EDFM and simple fluid model; the reason why the results of the simple fluid matched those of the poroelastic model well regardless of  $k_a h$  for the first parameter set and not for the second warrants further study.

## Chapter 7

### Conclusions and Future Work

#### 7.1 Conclusions

Quantifying acoustic scattering from the seafloor is a topic of particular importance in many scientific fields. For this reason, models that accurately describe both the physics of the sediment and the interaction of acoustic waves with the ocean bottom are needed. Recently, sediment models based on Biot's theory of poroelasticity have been shown to provide the best fit with experimental data [3, 4]. Seafloor roughness can be a dominant contributor to sound scattering at higher acoustic frequencies; many models have been developed to quantify this effect [2]. While the extant literature on the separate problems of the development of Biot's theory of poroelasticity and the study of acoustic scattering from rough surfaces is vast, only a very limited subset of this work deals with the combined problem of acoustic scattering from rough poroelastic surfaces [10, 11]. This thesis is an attempt to study the combined problem using the finite element method. To accomplish this, a poroelastic finite element formulation developed to model porous sound absorbing material used in noise control applications [8] is adapted to the problem of acoustic scattering from one-dimensional rough water-porous sediment interfaces.

In Chapter 1, a number of research questions are posed to guide the present work. Each of these questions will now be directly addressed in turn.

**1. How should the poroelastic finite element formulations be adapted to the problem of acoustic scattering from the seabed?**

As discussed in some detail in Section 2.4.1, many finite element formulations of Biot's equations have been derived for the modeling of porous sound absorbers and several of these formulations are general enough to be directly applied to the problem at hand. The majority of these formulations are based on the classical form of Biot's equations where the displacement fields of the frame and the pore fluid (or the pore fluid relative to the frame) are the dependent variables. While effective, these formulations require six degrees of freedom per node in three dimensions and do not couple naturally with acoustic media. An alternative formulation cast in terms of the frame displacement and the pore fluid pressure is developed by Atalla, Panneton, and Debergue in [8]. Referred to as the mixed formulation, this form of Biot's equations only requires four degrees of freedom per node in three dimensions and has the added benefit of coupling naturally with acoustic media. While a slightly more complicated mixed formulation has since been put forth by many of these same authors that affords easier coupling with elastic media [169], the original mixed formulation of [8] is sufficient for the present work. In fact, the mixed formulation of [8] can be directly adapted to exactly solve the problem of acoustic scattering from one-dimensional rough fluid-poroelastic interfaces without modification.



It should be noted that there is actually an advantage to using the mixed formulation of [8] to study the present problem rather than the one for which it was intended. As examined in [45], there is much weaker coupling into the slow wave for water-saturated porous materials than for air-saturated porous materials. For this reason, the mesh criteria used by Atalla and coworkers can be relaxed and meshing with respect to the wavelength of the slow wave is only needed at the fluid-poroelastic interface, as discussed in Section 4.2.4.

## **2. What are the effects of roughness on the acoustic scattering from poroelastic interfaces?**

Prior to the completion of this work, it was strongly suspected by the author that the roughness of the interface would cause greater coupling into the slow wave, thus causing more energy to be transmitted into the sediment and less scattered back into the water. Based on the results outlined in Sections 6.1.2 and 6.2.2, where the scattering strengths calculated using the full poroelastic finite element formulation are compared with those found using two formulations where the sediment is modeled as a fluid, the effects of increased coupling are not apparent for the parameter sets studied. In fact, the effective density fluid model developed in [5] matches the results of the full poroelastic model for all the cases studied; if coupling into the slow wave did become more prominent for rougher interfaces, one would have expected to see greater deviation between the EDFM and full poroelastic models as  $k_a h$  increases. More on the agreement between the EDFM and full poroelastic model is discussed below.

Also related to the coupling into the slow wave is the concern by Williams, Grochocinski, and Jackson in [10] that, since the roughness relief may not be small compared to the wavelengths of the slow and shear waves, the analytic scattering models may be inaccurate. However, as discussed in Sections 6.1.1 and 6.2.1, in general, all three analytic models considered do an admirable job matching the finite element results, even outside their expected regions of validity; this agreement further bolsters the conclusion that the interface roughness is not leading to substantially increased mode conversion.

**3. Do the three most widely used analytic scattering models—perturbation theory, the Kirchhoff approximation, and the small-slope approximation—perform well when applied to scattering from rough poroelastic surfaces and, if so, what are their regions of validity?**

In order to assess the accuracy of perturbation theory (PT), the Kirchhoff approximation (KA) and the small-slope approximation (SSA) when applied to scattering from rough poroelastic surfaces, the formally averaged scattering strengths obtained using these models are compared with the ensemble averaged scattering strengths calculated using the finite element method (FEM). This comparison is performed for sets of parameters following the papers of Yang, Broschat, and Galea [11] and Williams, Grochocinski, and Jackson [10]. For the parameters following [11], both monostatic and bistatic scattering is considered; only monostatic scattering is considered for the parameters adapted from [10]. The analytic models qualitatively match the FEM results for all but one of the parameter sets discussed in Sections 6.1.1 and

Table 7.1: Roughness parameters and analytic models that provided the best fit with the FEM monostatic scattering results for those parameters.

$\gamma_1$	$k_a h$	$k_a/K_0$	$s$	$k_a l$	<b>Best fit</b>	<b>Max diff.</b>	<b>Mean diff.</b>
4	0.04	4.19	0.01	5.92	PT/SSA	1.8 dB	0.6 dB
4	0.42	4.19	0.10	5.92	SSA	2.3 dB	0.9 dB
4	1.26	125.66	0.01	177.71	none	15+ dB	8+ dB
4	12.57	125.66	0.10	177.71	KA	1.5 dB	0.7 dB
2.05	0.01	0.52	0.01	0.92	PT/SSA	1.5 dB	0.8 dB
2.05	0.08	5.23	0.01	9.96	PT/SSA	1.6 dB	0.8 dB
2.05	0.81	52.36	0.01	99.61	SSA	1.5 dB	0.8 dB
2.05	1.00	64.38	0.01	122.47	SSA	2.0 dB	0.7 dB
2.05	8.13	523.60	0.01	996.08	SSA	2.8 dB	0.9 dB

6.2.1. However, to better quantify the performance of these models, Tables 7.1 and 7.2 have been generated to put forth the roughness parameters considered and which model performed best for those parameters. In addition to the roughness parameters previously defined, the *rms* slope  $s$  and the effective correlation length  $l$  as defined in Chapter 13 of [2] are included in these tables. All roughness quantities are non-dimensionalized.

Table 7.1 deals with the monostatic results. While determining the region of validity for a given roughness scattering model is much more difficult in the case of a von Karman roughness spectrum than for the well-studied, yet nonphysical Gaussian roughness spectrum, a few conclusions can be drawn. First, as speculated in [11], the results of perturbation theory are accurate when they coincide with those of the small-slope approximation; it appears that this region of agreement is when  $k_a h \ll 1$ . This result is not surprising, as  $k_a h \ll 1$  has long been considered a needed condition for the validity of

Table 7.2: Roughness parameters and analytic models that provided the best fit with the FEM bistatic scattering results for those parameters.

$\gamma_1$	$k_a h$	$k_a/K_0$	$s$	$k_a l$	<b>Best fit</b>	<b>Max diff.</b>	<b>Mean diff.</b>
4	0.04	4.19	0.01	5.92	PT/SSA	2.9 dB	0.7 dB
4	0.42	4.19	0.1	5.92	SSA	2.2 dB	0.6 dB
4	1.26	125.66	0.01	177.71	none	15+ dB	5+ dB
4	12.57	125.66	0.1	177.71	SSA	4.2 dB	1.2 dB

perturbation theory [80, 194]. Also, the small-slope approximation is seen to be the model that provides the best fit when  $k_a h \leq 1$  and  $s \ll 1$ ; the only case studied for which a model performs better than it is the sole case when  $k_a h \gg 1$  and the condition  $s \ll 1$  is not met. Furthermore, the reason for the great disparity between all three analytic models and the finite element results for the case of  $k_a h = 1.26$  is not clear. As seen in Figure 6.11, the poroelastic finite element results are in good agreement with both fluid models, so the reason for the disparity is not exclusive to poroelastic sediments. Finally, it is not at all clear if the quantities  $\gamma_1$ ,  $k_a/K_0$ , and  $k_a l$  are related to analytic model performance; they are simply included in the table for completeness.

Table 7.2 deals with the bistatic results and the conclusions are largely the same. Again, perturbation theory is found to be accurate when the condition  $k_a h \ll 1$  is met. Unlike in the monostatic case, there are no conditions for which any model outperforms the small-slope approximation. At  $\theta = 45^\circ$ , the monostatic results of the small-slope approximation and the Kirchhoff approximation coincide for the sole case where the Kirchhoff approximation outperforms the small-slope approximation in Table 7.1; perhaps the Kirch-

hoff approximation would provide better bistatic results for shallower grazing angles, where the monostatic results of the two models do not agree. Also, it is quite unusual that there is a great disparity between the finite element and analytic model results for both monostatic and bistatic scattering for the particular case when  $k_a h = 1.26$ ; unfortunately, the reason for these disparities remains unknown. Finally, there is again seemingly no correlation between the quantities  $\gamma_1$ ,  $k_a/K_0$ , and  $k_a l$  and the performance of the scattering models.

In summary, except for one case where the Kirchhoff approximation is better and another where no analytic scattering model matches the finite element results, the small-slope approximation is in agreement with the finite element results within 4.2 dB for the cases studied and within 3 dB when  $k_a h \leq 1$  and  $s \ll 1$ . On average, the small-slope results differ from those of the finite element method by 1.2 dB or less for every case where it provides the best fit. For this reason, one could make the claim that there would be no need for the computationally expensive finite element approach in the region where the small-slope approximation is valid should this region of validity be rigorously determined in the future.

#### **4. How does the scattering from media assumed to follow the effective density fluid model compare to the results obtained for the full poroelastic formulation?**

In Sections 6.1.2 and 6.2.2, the scattering strengths calculated using the full poroelastic formulation are compared to those found using two finite element formulations where the sediment is modeled as a fluid. The first is

a simple fluid where the sound speed is set equal to the fast wave speed and the fluid density is set equal to the average density. The second follows the effective density fluid model of Williams [5] referred to in the question above. For the parameters following [11], the results of both fluid models are within 3 dB with an average deviation of around 1 dB for all monostatic and bistatic cases considered with the exception of the parametric case where  $k_a h = 12.57$ . In fact, while the accuracy of the simple fluid model does seem to decrease as  $k_a h$  is increased, it is rather hard to distinguish between the performance of the two fluid models for these parameters.

For the second study, the parameters used are adapted from [10]. While the performance of the EDFM is similar to the first study, it is very clear from this study that the simple fluid model can deviate from the full poroelastic results quite a bit more than the EDFM as  $k_a h$  is increased. To quantify this point, the average deviation of the EDFM from the poroelastic model is less than 0.1 dB for all cases while the average deviation of the simple fluid model from the poroelastic model is nearly 2 dB for the cases where the condition  $k_a h \ll 1$  is no longer satisfied. It should be noted that the EDFM results at all angles are within 2 dB of those of the full poroelastic formulation for all cases considered during the second study.

From the results of the two studies outlined in Chapter 6, it can be concluded that, for the half-space scattering problem considered in this thesis, the scattering strengths found using the EDFM formulation are exceptionally close to those found using the full poroelastic formulation despite the EDFM

formulation being both much simpler to implement and considerably less computationally intensive. It is therefore the author's recommendation that the EDFM be used instead of the full poroelastic model for problems described by Figure 1.1 provided it is known that the shear wave speed is low and the coupling into the shear wave is minimal.

## 7.2 Future Work

While this thesis has successfully shown how the poroelastic finite element formulation of [8] can be applied to study the combined problem of acoustic scattering from a one-dimensional rough fluid-poroelastic interface, many issues raised remain unresolved. First, it is unclear why none of the three analytic models considered compare well with the scattering strengths found using the finite element method for the monostatic and bistatic cases depicted in Figures 6.3 and 6.7, respectively. A rigorous parametric study of the validity of the small-slope approximation as compared to the finite element results is needed to determine the reason behind the anomalous disparity seen in these cases. Second, it is also unclear why the simple fluid model performs as well as the EDFM for the parameters of the first study and not of the second; further research into this issue may help shed light on the physical reasons behind the shortcoming of conventional fluid sediment models. Third, while the EDFM seems to be a suitable alternative to the full poroelastic model for the half-space scattering problem considered here, it is likely that the full poroelastic formulation is needed to properly capture the physics of

the related problem of scattering from a layered seabed. Future work that seeks to show whether the EDFM is a suitable replacement for the poroelastic model for all circumstances or just for the problem studied here is therefore recommended. Lastly, for problems that require poroelastic-elastic coupling, the modified poroelastic finite element formulation of [169] should be used instead of [8]; it is worth exploring whether that formulation is as easy to adapt to seabed scattering problems as the simpler one used here.



## Appendices

## Appendix A

### Analytical Reflection Coefficient Calculation

Appendix B of Stoll's monograph [14] deals with the details of calculating the fluid-poroelastic plane wave reflection coefficient analytically. However, due to technological constraints at the time of publishing, the expressions provided are not as succinct as they could be as Stoll is forced to calculate the real and imaginary components of the wave amplitudes separately. This appendix presents a simpler formulation presented to the author by Dr. Marcia Isakson.

In order to properly calculate the reflection coefficient, one must know the wavenumbers of the waves propagating in the poroelastic medium. Following Chapter 1 of [14], these can be obtained by finding the roots of two equations. The roots of the first equation give the wavenumbers of the fast and slow waves  $l_1$  and  $l_2$  and can be written in determinant form as

$$\begin{vmatrix} \tilde{H}l^2 - \rho\omega^2 & \rho_f\omega^2 - \tilde{C}l^2 \\ \tilde{C}l^2 - \rho_f\omega^2 & m\omega^2 - \tilde{M}l^2 - i\omega F(\Theta)\eta/\kappa \end{vmatrix} = 0, \quad (\text{A.1})$$

where

$$\tilde{H} = \frac{(K_r - \tilde{K}_b)^2}{D - \tilde{K}_b} + \tilde{K}_b + \frac{4}{3}\tilde{\mu}, \quad (\text{A.2})$$

$$\tilde{C} = \frac{K_r(K_r - \tilde{K}_b)}{D - \tilde{K}_b}, \quad (\text{A.3})$$

$$\widetilde{M} = \frac{K_r^2}{D - \widetilde{K}_b}, \quad (\text{A.4})$$

$$D = K_r \left[ 1 + \beta \left( \frac{K_r}{K_f} - 1 \right) \right], \quad (\text{A.5})$$

and

$$m = \frac{\tau \rho_f}{\beta}. \quad (\text{A.6})$$

The second equation gives the wavenumber of the shear wave  $l_s$  and can be written as

$$\begin{vmatrix} \rho\omega^2 - \widetilde{\mu}l^2 & \rho_f\omega^2 \\ \rho_f\omega^2 & m\omega^2 - i\omega F(\Theta)\eta/\kappa \end{vmatrix} = 0. \quad (\text{A.7})$$

Next, the following quantities are needed to determine the reflection coefficient:

$$k_c = k_a \cos \theta \quad (\text{A.8})$$

$$m_1 = \frac{\widetilde{H}l_1^2 - \rho\omega^2}{\widetilde{C}l_1^2 - \rho_f\omega^2} \quad (\text{A.9})$$

$$k_1 = \sqrt{l_1^2 - k_c^2} \quad (\text{A.10})$$

$$m_2 = \frac{\widetilde{H}l_2^2 - \rho\omega^2}{\widetilde{C}l_2^2 - \rho_f\omega^2} \quad (\text{A.11})$$

$$k_2 = \sqrt{l_2^2 - k_c^2} \quad (\text{A.12})$$

$$q = \frac{\rho\omega^2 - \widetilde{\mu}l_s^2}{\widetilde{C}l_s^2 - \rho_f\omega^2} \quad (\text{A.13})$$

$$k_s = \sqrt{l_s^2 - k_c^2} \quad (\text{A.14})$$

As discussed in Appendix B of [14], the following matrix equation can be solved to determine the complex wave amplitudes:

$$[B] \{A\} = \{b\}, \quad (\text{A.15})$$

where the vector  $\{A\}$  contains the complex wave amplitudes. The terms of the matrix  $[B]$  and the vector  $\{b\}$  are defined below:

$$\begin{aligned}
B_{11} &= k_a \\
B_{12} &= (1 - m_1) \frac{k_1}{\sin \theta} \\
B_{13} &= (1 - m_2) \frac{k_2}{\sin \theta} \\
B_{14} &= (1 - q) \frac{k_c}{\sin \theta} \\
b_1 &= k_a \\
B_{21} &= -\frac{\rho_a \omega^2}{\sin \theta} \\
B_{22} &= \frac{(\tilde{H} - 2\tilde{\mu} - \tilde{C}m_1) l_1^2 + 2\tilde{\mu}k_1^2}{\sin \theta} \\
B_{23} &= \frac{(\tilde{H} - 2\tilde{\mu} - \tilde{C}m_2) l_2^2 + 2\tilde{\mu}k_2^2}{\sin \theta} \\
B_{24} &= \frac{2\tilde{\mu}k_c k_s}{\sin \theta} \\
b_2 &= \frac{\rho_a \omega^2}{\sin \theta} \\
B_{31} &= \frac{\rho_a \omega^2}{\sin \theta} \\
B_{32} &= -\left(\tilde{C} - m_1 \tilde{M}\right) \frac{l_1^2}{\sin \theta} \\
B_{33} &= -\left(\tilde{C} - m_2 \tilde{M}\right) \frac{l_2^2}{\sin \theta} \\
B_{34} &= 0 \\
b_3 &= -\frac{\rho_a \omega^2}{\sin \theta}
\end{aligned}$$

$$\begin{aligned}B_{41} &= 0 \\B_{42} &= \frac{2k_c k_1}{\sin \theta} \\B_{43} &= \frac{2k_c k_2}{\sin \theta} \\B_{44} &= \frac{k_c^2 - k_s^2}{\sin \theta} \\b_4 &= 0\end{aligned}$$

The reflection coefficient  $RC(\Theta)$  is  $A_1$ , the first component of the complex amplitude vector  $\{A\}$ .

# Appendix B

## Analytic Scattering Models

A brief overview of the three analytic scattering models compared with the finite element method in this thesis is presented below. Note that for the form of all three models shown, the assumed time convention is  $e^{-i\omega t}$ , not the convention  $e^{i\omega t}$  used in the rest of this thesis. Also, incident angles are used here instead of grazing angles; that is to say,  $\theta_i = \pi/2 - \theta$ .

### B.1 Perturbation Theory

Perturbation theory (PT) was first applied to scattering from poroelastic surfaces in [10] and was adapted to the case of scattering from one-dimensional interfaces in [11]. The bistatic scattering cross section is given by

$$\sigma^{PT}(k_{sx}, k_{ix}) = \frac{k_{sz}^2}{k} |G_{1,1}(k_{sx}, k_{ix})|^2 W(k_{ix} - k_{sx}), \quad (\text{B.1})$$

where  $k$  is the acoustic wavenumber,  $k_{ix} = k \sin \theta_i$ ,  $k_{sx} = k \sin \theta_s$ ,  $k_{sz} = k \cos \theta_s$ ,  $\theta_i$  is the incident angle,  $\theta_s$  is the scattered angle, and  $G_{1,1}(k_{sx}, k_{ix})$  is given in the Appendix of [11]. The monostatic scattering cross section can be calculated by setting  $k_{sx} = -k_{ix}$ . PT is considered a suitable approximation far from specular for small  $kh$  values and small surface slopes.

## B.2 Kirchhoff Approximation

The Kirchhoff approximation (KA) is adapted to the given problem by modifying the formulation given in Chapter 13 of [2] to include the effects of the poroelastic sediment. The bistatic cross section is as follows:

$$\sigma^{KA}(k_{sx}, k_{ix}) = \frac{(k_{ix}v_x/v_z + k_{iz})^2}{2\pi k} |V_{ww}(\theta_{is})|^2 e^{-v_z^2 h^2} \int dx e^{iv_x x} \left[ e^{v_z^2 h^2 C(x)} - 1 \right], \quad (\text{B.2})$$

where  $k_{iz} = k \cos \theta_i$ ,  $v_x = k_{ix} - k_{sx}$ ,  $v_z = k_{iz} + k_{sz}$ ,  $h$  is the surface *rms* height,  $C(x)$  is the surface correlation function, and  $V_{ww}$  is the reflection coefficient for flat fluid-poroelastic interfaces. The angle  $\theta_{is}$  is calculated using the following expression:

$$\theta_{is} = \arcsin \left( \frac{\sqrt{v_x^2 + v_z^2}}{2k} \right). \quad (\text{B.3})$$

For one-dimensional interfaces, the surface correlation function can be found using

$$C(x) = \frac{1}{h^2} \int_{-\infty}^{\infty} W(K) e^{iKx} dK. \quad (\text{B.4})$$

KA is generally found to be more accurate than PT for approximating scattering near the specular direction and less accurate for regions away from specular.

## B.3 Small-Slope Approximation

From the above discussion, it can be concluded that PT and KA have complimentary regions of validity. Another model, the small-slope approximation (SSA), is found to be the best of both, converging to PT far away from

specular and to KA near specular. For this reason, SSA is considered the most robust model of the three presented in this appendix. SSA was first extended to scattering from one-dimensional poroelastic surfaces in [11]. The bistatic scattering cross section can be found using the following expression:

$$\sigma^{SSA}(k_{sx}, k_{ix}) = \frac{k_{sz}^2}{2\pi k v_z^2} |G_{1,1}(k_{sx}, k_{ix})|^2 e^{-v_z^2 h^2} \int dx e^{iv_x x} \left[ e^{v_z^2 h^2 C(x)} - 1 \right]. \quad (\text{B.5})$$



# Appendix C

## FEM Fluid Models

In Sections 6.1.2 and 6.2.2, the results of two finite element formulations based on fluid models are compared with those of the full poroelastic formulation given in Chapters 3 and 4. This appendix is intended to provide more detail on these fluid models.

### C.1 Simple Fluid Model

The model referred to as the simple fluid model is called thus as it is obtained by simply setting the acoustic sound speed equal to the fast wave speed and the fluid density equal to the average density of the poroelastic medium. As described in Appendix A, the wavenumbers of the fast, slow, and shear waves,  $l_1$ ,  $l_2$ , and  $l_s$ , are obtained by finding the roots of Eqs. A.1 and A.7. Using the wavenumber of the fast wave, the acoustic sound speed  $c_{sf}$  and attenuation  $\alpha_{sf\lambda}$  needed as inputs to the simple fluid model can be obtained using the expressions [14]

$$c_{sf} = \frac{\omega}{\text{Re}(l_1)}, \quad (\text{C.1})$$

and [2]

$$\alpha_{sf\lambda} = \frac{40\pi\delta_p}{\ln(10)}, \quad (\text{C.2})$$

where  $\alpha_{sf\lambda}$  has units dB/ $\lambda$  and

$$\delta_p = \frac{\text{Im}(l_1)}{\text{Re}(l_1)}. \quad (\text{C.3})$$

The fluid density is found by

$$\rho_{sf} = \rho = (1 - \beta) \rho_s + \beta \rho_f. \quad (\text{C.4})$$

## C.2 EDFM

The effective density fluid model (or EDFM) is an equivalent fluid model developed by Williams in [5] that is designed to provide a better approximation of sediments governed by Biot theory than the simple fluid model described above. It is derived by taking the limits  $K_b \rightarrow 0$  and  $\mu \rightarrow 0$ . Taking this limit causes the stress tensor of the frame *in vacuo*  $\hat{\sigma}_s$  to vanish and Eq. 3.32 can be rewritten

$$\omega^2 \rho_{\text{eff}}(\omega) \mathbf{u} + \boldsymbol{\Psi}_c(\omega) \nabla p_f = 0, \quad (\text{C.5})$$

where the poroelastic coupling factor  $\boldsymbol{\Psi}_c$  is now

$$\boldsymbol{\Psi}_c = \frac{\rho_f}{\rho_c(\omega)} - 1. \quad (\text{C.6})$$

Eq. 3.33 is unaltered other than the fact that the Biot modulus  $M$  is now

$$M = \frac{K_r}{1 + \beta (K_r/K_f - 1)}. \quad (\text{C.7})$$

In order to obtain a single equation of motion analogous to the Helmholtz equation, the term  $\rho_c(\omega) \boldsymbol{\Psi}_c(\omega) / \rho_{\text{eff}}$  is multiplied to the divergence of Eq. C.5

and the resulting equation is added to Eq. 3.33 to obtain

$$\nabla^2 p_f + k_{\text{EDFM}}^2(\omega) p_f = 0, \quad (\text{C.8})$$

where

$$k_{\text{EDFM}}^2(\omega) = \frac{\omega^2 \rho_{\text{EDFM}}(\omega)}{M}, \quad (\text{C.9})$$

and

$$\rho_{\text{EDFM}}(\omega) = \frac{\rho_c(\omega) \rho_{\text{eff}}(\omega)}{\rho_{\text{eff}}(\omega) + \mathfrak{W}_c^2(\omega) \rho_c(\omega)}. \quad (\text{C.10})$$

Eq. C.10 gives the density of the effective fluid. The acoustic sound speed  $c_{\text{EDFM}}$  and attenuation  $\alpha_{\text{EDFM}\lambda}$  can then be found using expressions

$$c_{\text{EDFM}} = \frac{\omega}{\text{Re} [k_{\text{EDFM}}(\omega)]}, \quad (\text{C.11})$$

and

$$\alpha_{\text{EDFM}\lambda} = \frac{40\pi \delta_{pe}}{\ln(10)}, \quad (\text{C.12})$$

where  $\alpha_{\text{EDFM}\lambda}$  has units dB/ $\lambda$  and

$$\delta_{pe} = \frac{\text{Im} [k_{\text{EDFM}}(\omega)]}{\text{Re} [k_{\text{EDFM}}(\omega)]}. \quad (\text{C.13})$$

# Appendix D

## COMSOL Implementation

As of version 4.4, COMSOL Multiphysics has a poroelastic finite element formulation equivalent to the one presented in Chapter 4 as part of the Poroelastic Waves Interface within the Acoustics Module. A given realization of the model problem can be generated by creating two domains in COMSOL separated by a rough interface and surrounded by PMLs set to rational coordinate stretching. The fluid domain is modeled using the Pressure Acoustics, Frequency Domain Interface and the entire domain and associated PMLs are defined as a Pressure Acoustics Model. Similarly, the poroelastic domain and associated PMLs are modeled using the Poroelastic Waves Interface and defined as a Poroelastic Material. The rough interface can be created by using LiveLink with MATLAB and connecting the points given by Eq. 4.22 using a series of Bezier polygons.

In order for the created COMSOL models to be physically accurate, the fluid and poroelastic domains must be coupled using the conditions described in Eqs. 3.39 through 3.41. The continuity of normal stresses and the continuity of pressure are both enforced through a Porous, Pressure node in the Poroelastic Waves Interface. This node is assigned to the rough interface, and the

pressure  $p_0$  is set to the total acoustic pressure acting on the interface. A Normal Acceleration node in the Pressure Acoustics, Frequency Domain Interface is used to ensure continuity of normal displacements on the interface. Within the Normal Acceleration node, Inward Acceleration is selected as the type and  $a_n$  is set to  $-\omega^2 (u_x n_x + u_z n_z)$ , where  $u_x$  and  $u_z$  are the x- and z-components of the frame displacement field and  $n_x$  and  $n_z$  are the x- and z-components of the normal vector pointing out from the poroelastic domain and into the fluid domain.

Two more node assignments are needed in the Pressure Acoustics, Frequency Domain Interface to complete the model. A Far-Field Calculation node is assigned to the rough interface since the far-field scattered pressure is needed to calculate the scattering strength (see Section 4.2.5). Finally, a Background Pressure Field node is assigned to the fluid domain (excluding PMLs) and a custom background pressure field is prescribed following Section 4.2.3.

## Bibliography

- [1] J.-T. Wang, F. Jin, and C.-H. Zang, “Reflection and transmission of plane waves at an interface of water/porous sediment with underlying solid substrate,” *Ocean Engineering*, vol. 63, pp. 8–16, 2013.
- [2] D. Jackson and M. Richardson, *High-Frequency Seafloor Acoustics*. Springer Verlag, New York, 2007.
- [3] M. Isakson, N. Chotiros, R. Yarbrough, and J. Piper, “Quantifying the effects of roughness scattering on reflection loss measurements,” *J. Acoust. Soc. Am.*, vol. 132, no. 6, pp. 3687–3697, 2012.
- [4] K. L. Williams, D. R. Jackson, E. I. Thorsos, D. Tang, and K. B. Briggs, “Acoustic backscattering experiments in a well characterized sand sediment: data/model comparisons using sediment fluid and Biot models,” *IEEE J. Ocean Eng.*, vol. 27, no. 3, pp. 376–387, 2002.
- [5] K. Williams, “An effective density fluid model for acoustic propagation in sediments derived from Biot theory,” *J. Acoust. Soc. Am.*, vol. 110, no. 5, pp. 2276–2281, 2001.
- [6] H. J. Camin and M. J. Isakson, “A comparison of sediment reflection coefficient measurements to elastic and poro-elastic models,” *J. Acoust. Soc. Am.*, vol. 120, no. 5, pp. 2437–2449, 2006.

- [7] K. L. Williams, D. R. Jackson, E. I. Thorsos, D. Tang, and S. G. Schock, “Comparison of sound speed and attenuation measured in a sandy sediment to prediction based on the Biot theory of porous media,” *IEEE J. Ocean Eng.*, vol. 27, no. 3, pp. 413–428, 2002.
- [8] N. Atalla, R. Panneton, and P. Debergue, “A mixed displacement-pressure formulation for poroelastic materials,” *J. Acoust. Soc. Am.*, vol. 104, no. 3, pp. 1444–1452, 1998.
- [9] E. I. Thorsos, D. R. Jackson, and K. L. Williams, “Modeling of subcritical penetration into sediments due to interface roughness,” *J. Acoust. Soc. Am.*, vol. 107, no. 1, pp. 263–277, 2000.
- [10] K. Williams, J. Grochocinski, and D. Jackson, “Interface scattering by poroelastic seafloors: First-order theory,” *J. Acoust. Soc. Am.*, vol. 110, no. 6, pp. 2956–2963, 2001.
- [11] T. Yang, S. Broschat, and C. Galea, “A comparison of perturbation theory and the small-slope approximation for acoustic scattering from a rough interface for a Biot medium,” *IEEE J. Ocean Eng.*, vol. 27, no. 3, pp. 403–412, 2002.
- [12] I. Tolstoy, “Introduction,” in *Acoustics, Elasticity, and Thermodynamics of Porous Media: Twenty-One Papers by M.A. Biot* (I. Tolstoy, ed.), Acoustical Society of America, Woodbury, NY, 1992.

- [13] M. Schanz, *Wave Propagation in Viscoelastic and Poroelastic Continua: A Boundary Element Approach*. Springer Verlag, Berlin, 2001.
- [14] R. Stoll, *Lecture Notes in Earth Sciences, Vol. 26: Sediment Acoustics*. Springer-Verlag, New York, 1989.
- [15] M. Biot, “General theory of three dimensional consolidation,” *J. Appl. Phys.*, vol. 12, no. 2, pp. 155–164, 1941.
- [16] M. Biot, “Consolidation settlement under a rectangular load distribution,” *J. Appl. Phys.*, vol. 12, no. 5, pp. 426–430, 1941.
- [17] M. Biot, “Consolidation settlement of a soil with an impervious top surface,” *J. Appl. Phys.*, vol. 12, no. 7, p. 578.
- [18] M. Biot, “Bending settlement of a slab resting on a consolidating foundation,” *J. Appl. Phys.*, vol. 13, no. 1, pp. 35–40, 1942.
- [19] M. Biot, “Theory of elasticity and consolidation for a porous anisotropic solid,” *J. Appl. Phys.*, vol. 26, no. 2, pp. 182–185, 1955.
- [20] M. Biot, “General solutions of the equations of elasticity and consolidation for a porous material,” *J. Appl. Mech.*, vol. 78, pp. 91–96, 1956.
- [21] M. Biot, “Theory of propagation of elastic waves in a fluid saturated porous solid. I. Low frequency range,” *J. Acoust. Soc. Am.*, vol. 28, no. 2, pp. 168–178, 1956.



- [22] M. Biot, “Theory of propagation of elastic waves in a fluid saturated porous solid. II. High frequency range,” *J. Acoust. Soc. Am.*, vol. 28, no. 2, pp. 179–191, 1956.
- [23] M. Biot, “Theory of deformation of a porous viscoelastic anisotropic solid,” *J. Appl. Phys.*, vol. 27, no. 5, pp. 459–467, 1956.
- [24] M. Biot and D. Willis, “The elastic coefficients of the theory of consolidation,” *J. App Mech.*, vol. 24, pp. 594–601, 1957.
- [25] M. Biot, “Mechanics of deformation and acoustic propagation in porous media,” *J. Appl. Phys.*, vol. 33, no. 4, pp. 1482–1498, 1962.
- [26] M. Biot, “Generalized theory of acoustic propagation in porous dissipative media,” *J. Acoust. Soc. Am.*, vol. 34, no. 5, pp. 1254–1264, 1962.
- [27] R. Stoll and G. Bryan, “Wave attenuation in saturated sediments,” *J. Acoust. Soc. Am.*, vol. 47, no. 5, pp. 1440–1447, 1970.
- [28] R. Stoll, “Acoustic waves in saturated sediments,” in *Physics of Sound in Marine Sediments* (L. Hampton, ed.), pp. 19–40.
- [29] R. Stoll, “Acoustic waves in ocean sediments,” *Geophysics*, vol. 42, no. 4, pp. 715–725, 1977.
- [30] R. Stoll and T.-K. Kan, “Reflection of acoustic waves at a water-sediment interface,” *J. Acoust. Soc. Am.*, vol. 70, no. 1, pp. 149–156, 1981.

- [31] H. Deresiewicz and R. Skalak, “On uniqueness in dynamic poroelasticity,” *Bulletin of the Seismological Society of America*, vol. 53, no. 4, pp. 783–788, 1963.
- [32] O. Lovera, “Boundary conditions for a fluid-saturated porous solid,” *Geophysics*, vol. 52, no. 2, pp. 174–178, 1987.
- [33] V. de la Cruz and T. Spanos, “Seismic boundary conditions for porous media,” *J. Geophys. Res.*, vol. 94, no. B3, pp. 3025–3029, 1989.
- [34] B. Gurevich and M. Schoenberg, “Interface conditions for Biot’s equation of poroelasticity,” *J. Acoust. Soc. Am.*, vol. 105, no. 5, pp. 2585–2589, 1999.
- [35] M. Sharma, “Wave propagation across the boundary between two dissimilar poroelastic solids,” *J. Sound Vib.*, vol. 314, pp. 657–671, 2008.
- [36] H. Deresiewicz, “The effect of boundaries on wave propagation in a liquid-filled porous solid: I. Reflection of plane waves at a free plane boundary (non-dissipative case),” *Bull. Seis. Am.*, vol. 50, no. 4, pp. 599–607, 1960.
- [37] H. Deresiewicz and J. Rice, “The effect of boundaries on wave propagation in a liquid-filled porous solid: III. Reflection of plane waves at a free plane boundary (general case),” *Bull. Seis. Am.*, vol. 52, no. 3, pp. 595–625, 1962.

- [38] H. Deresiewicz and J. Rice, “The effect of boundaries on wave propagation in a liquid-filled porous solid: V. Transmission across a plane interface,” *Bull. Seis. Am.*, vol. 54, no. 1, pp. 409–416, 1964.
- [39] H. Deresiewicz and A. Levy, “The effect of boundaries on wave propagation in a liquid-filled porous solid: X. Transmission through a stratified medium,” *Bull. Seis. Am.*, vol. 57, no. 3, pp. 381–391, 1967.
- [40] S. Hajra and A. Mukhopadhyay, “Reflection and refraction of seismic waves incident obliquely at the boundary of a liquid-saturated porous solid,” *Bull. Seis. Am.*, vol. 72, no. 5, pp. 1509–1533, 1982.
- [41] N. Dutta and H. Odé, “Seismic reflections from a gas-water contact,” *Geophysics*, vol. 48, no. 2, pp. 148–162, 1983.
- [42] J. Allard, C. Depollier, P. Rebillard, W. Lauriks, and A. Cops, “Inhomogeneous Biot waves in layered media,” *J. Appl. Phys.*, vol. 66, no. 6, pp. 2278–2284, 1989.
- [43] K. Wu, Q. Xue, and L. Adler, “Reflection and transmission of elastic waves from a fluid-saturated porous solid boundary,” *J. Acoust. Soc. Am.*, vol. 87, no. 6, pp. 2349–2358, 1990.
- [44] J. Santos, J. Corbero, C. Ravazzoli, and J. Hensley, “Reflection and transmission coefficients in fluid-saturated porous media,” *J. Acoust. Soc. Am.*, vol. 91, no. 4, pp. 1911–1923, 1992.

- [45] D. Albert, “A comparison between wave propagation in water-saturated and air-saturated porous materials,” *J. Appl. Phys.*, vol. 73, no. 1, pp. 28–36, 1993.
- [46] A. Denneman, G. Drijkoningen, D. Smeulders, and K. Wapenaar, “Reflection and transmission of waves at a fluid/porous-medium interface,” *Geophysics*, vol. 67, no. 1, pp. 282–291, 2002.
- [47] M. Sharma, “3-D wave propagation in a general anisotropic poroelastic medium: reflection and refraction at an interface with fluid,” *Geophys. J. Int.*, vol. 157, pp. 947–958, 2004.
- [48] J. Nandal and T. Saini, “Reflection and refraction at an imperfectly bonded interface between poroelastic solid and cracked elastic solid,” *J. Seismol.*, vol. 17, pp. 239–253, 2013.
- [49] J. Berryman, “Elastic wave propagation in fluid-saturated porous media,” *J. Acoust. Soc. Am.*, vol. 69, no. 2, pp. 416–424, 1981.
- [50] T. Yamamoto, “Acoustic propagation in the ocean with a poro-elastic bottom,” *J. Acoust. Soc. Am.*, vol. 73, no. 5, pp. 1587–1596, 1983.
- [51] K. Attenborough, “On the acoustic slow wave in air-filled granular media,” *J. Acoust. Soc. Am.*, vol. 81, no. 1, pp. 93–102, 1987.
- [52] J. Allard and N. Atalla, *Propagation of Sound in Porous Media*. West Sussex, England, 2nd ed., 2009.

- [53] T. Plona, “Observation of a second bulk compressional wave in a porous medium at ultrasonic frequencies,” *Appl. Phys. Lett.*, vol. 36, no. 4, pp. 259–261, 1980.
- [54] J. Berryman, “Confirmation of Biot’s theory,” *Appl. Phys. Lett.*, vol. 37, no. 4, pp. 382–384, 1980.
- [55] D. Johnson and T. Plona, “Acoustic slow waves and the consolidation transition,” *J. Acoust. Soc. Am.*, vol. 72, no. 2, pp. 556–565, 1982.
- [56] P. Nagy, L. Adler, and B. Bonner, “Slow wave propagation in air-filled porous materials and natural rocks,” *Appl. Phys. Lett.*, vol. 56, no. 25, pp. 2504–2506, 1990.
- [57] F. Boyle and N. Chotiros, “Experimental detection of a slow acoustic wave in sediment at shallow grazing angles,” *J. Acoust. Soc. Am.*, vol. 91, no. 5, pp. 2615–2619, 1992.
- [58] K. Nakagawa, K. Soga, and J. Mitchell, “Observation of Biot compressional wave of the second kind in granular soils,” *Géotechnique*, vol. 47, no. 1, pp. 133–147, 1997.
- [59] O. Kelder and D. Smeulders, “Observation of the Biot slow wave in water-saturated nivelsteiner sandstone,” *Geophysics*, vol. 62, no. 6, pp. 1794–1796, 1997.

- [60] Y. Bouzidi and D. Schmitt, “Measurement of the speed and attenuation of the Biot slow wave using a large ultrasonic transmitter,” *J. Geophys. Res.*, vol. 114, p. B08201, 2009.
- [61] A. Turgut and T. Yamamoto, “Measurements of acoustic wave velocities and attenuation in marine sediments,” *J. Acoust. Soc. Am.*, vol. 87, no. 6, pp. 2376–2383, 1990.
- [62] M. King, J. Mardsen, and J. Dennis, “Biot dispersion for P- and S-wave velocities in partially and fully saturated sandstones,” *Geophys. Prospect.*, vol. 48, pp. 1075–1089, 2000.
- [63] R. Stoll, “Velocity dispersion in water-saturated granular sediment,” *J. Acoust. Soc. Am.*, vol. 111, no. 2, pp. 785–793, 2002.
- [64] K. Ohkawa, “Confirmation of the Biot theory for water-saturated sands at high frequencies and effects of scattering on the attenuation of sound waves,” *J. Acoust. Soc. Am.*, vol. 119, no. 2, pp. 709–711, 2006.
- [65] N. Chotiros, A. Lyons, J. Osler, and N. Pace, “Normal incidence reflection loss from a sandy sediment,” *J. Acoust. Soc. Am.*, vol. 112, no. 5, pp. 1831–1841, 2002.
- [66] M. Buckingham, “Wave propagation, stress relaxation, and grain-to-grain shearing in saturated, unconsolidated marine sediments,” *J. Acoust. Soc. Am.*, vol. 108, no. 6, pp. 2796–2815, 2000.

- [67] J.-X. Zhou, X.-Z. Zhang, and D. Knobles, “Low-frequency geoacoustic model for the effective properties of sandy seabottoms,” *J. Acoust. Soc. Am.*, vol. 125, no. 5, pp. 2847–2866, 2009.
- [68] R. Burridge and J. Keller, “Poroelasticity equations derived from microstructure,” *J. Acoust. Soc. Am.*, vol. 70, no. 4, pp. 1140–1146, 1981.
- [69] G. Mavko, T. Mukerji, and J. Dvorkin, *The Rock Physics Handbook*. Cambridge University Press, Cambridge, UK, 2nd ed., 2009.
- [70] J. Dvorkin and A. Nur, “Dynamic poroelasticity: A unified model with the squirt and the Biot mechanisms,” *Geophysics*, vol. 58, no. 4, pp. 524–533, 1993.
- [71] M. Jakobsen and M. Chapman, “Unified theory of global flow and squirt flow in cracked porous media,” *Geophysics*, vol. 74, no. 2, pp. WA65–WA76, 2009.
- [72] N. Chotiros and M. Isakson, “A broadband model of sandy ocean sediments: Biot-Stoll with contact squirt flow and shear drag,” *J. Acoust. Soc. Am.*, vol. 116, no. 4, pp. 2011–2022, 2004.
- [73] J. Berryman and H. Wang, “Elastic wave propagation and attenuation in a double-porosity dual-permeability medium,” *Int. J. Rock. Mech. Min.*, vol. 37, pp. 63–78, 2000.

- [74] T. XiaoMing, “A unified theory for elastic wave propagation through porous media containing cracks—An extension of Biot’s poroelastic wave theory,” *Sci. China Earth Sci.*, vol. 54, no. 9, pp. 1441–1452, 2011.
- [75] W.-C. Lo, G. Sposito, and E. Majer, “Wave propagation through elastic porous media containing two immiscible fluids,” *Water Resour. Res.*, vol. 41, p. W02025, 2005.
- [76] M. Buckingham, “On pore-fluid viscosity and the wave properties of saturated granular materials including marine sediments,” *J. Acoust. Soc. Am.*, vol. 122, no. 3, pp. 1486–1501, 2007.
- [77] N. Chotiros and M. Isakson, “Comments on ‘On pore fluid viscosity and the wave properties of saturated granular materials including marine sediments’,” *J. Acoust. Soc. Am.*, vol. 127, no. 4, pp. 2095–2098, 2010.
- [78] M. Prasad and R. Meissner, “Attenuation mechanisms in sands: Laboratory versus theoretical (Biot) data,” *Geophysics*, vol. 57, no. 5, pp. 710–719, 1992.
- [79] M. Buckingham, “Response to: Comments on ‘On pore fluid viscosity and the wave properties of saturated granular materials including marine sediments’,” *J. Acoust. Soc. Am.*, vol. 127, no. 4, pp. 2099–2102, 2010.
- [80] J. Ogilvy, *Theory of Wave Scattering from Random Rough Surfaces*. IOP Publishing, Bristol, England, 1991.



- [81] K. Warnick and W. Chew, “Numerical simulation methods for rough surface scattering,” *Waves Random Media*, vol. 11, pp. R1–R30, 2001.
- [82] T. Elfouhaily and C.-A. Guérin, “A critical survey of approximate scattering wave theories from random rough surfaces,” *Waves Random Media*, vol. 14, pp. R1–R40, 2004.
- [83] J. Strutt (Lord Rayleigh), *The Theory of Sound: Volume Two*. Dover Publications, New York, second revised ed., 1945.
- [84] S. Rice, “Reflection of electromagnetic waves from slightly rough surfaces,” *Commun. Pure Appl. Math.*, vol. 4, no. 2-3, pp. 351–378, 1951.
- [85] P. Waterman, “Scattering by periodic surfaces,” *J. Acoust. Soc. Am.*, vol. 57, no. 4, pp. 791–802, 1975.
- [86] G. Agarwal, “Interaction of electromagnetic waves at rough dielectric surfaces,” *Phys. Rev. B*, vol. 15, no. 4, pp. 2371–2383, 1977.
- [87] C. Lopez, F. Yndurian, and N. García, “Iterative series for calculating the scattering of waves from a hard corrugated surface,” *Phys. Rev. B*, vol. 18, no. 2, pp. 970–972, 1978.
- [88] M. Nieto-Vesperinas and N. García, “A detailed study of the scattering of scalar waves from random rough surfaces,” *Opt. Acta*, vol. 28, no. 12, pp. 1651–1672, 1981.

- [89] D. Jackson, D. Winebrenner, and A. Ishimaru, “Comparison of perturbation theories for rough-surface scattering,” *J. Acoust. Soc. Am.*, vol. 83, no. 3, pp. 961–969, 1988.
- [90] E. Thorsos and D. Jackson, “The validity of the perturbation approximation for rough surface scattering using a Gaussian roughness spectrum,” *J. Acoust. Soc. Am.*, vol. 86, no. 1, pp. 261–277, 1989.
- [91] L. Brekhovskikh, “The diffraction of waves by a rough surface (in Russian),” *Zh. ekspl. teor. Fiz.*, vol. 23, pp. 275–304, 1952.
- [92] M. Isakovich, “Wave scattering from a stastically rough surface (in Russian),” *Zh. ekspl. teor. Fiz.*, vol. 23, pp. 305–314, 1952.
- [93] C. Eckart, “The scattering of sound from the sea surface,” *J. Acoust. Soc. Am.*, vol. 25, no. 3, pp. 566–570, 1953.
- [94] W. Meecham, “On the use of the Kirchhoff approximation for the solution of reflection problems,” *J. Rational Mech. Anal.*, vol. 5, no. 2, pp. 323–334, 1956.
- [95] E. Liska and J. McCoy, “Scattering at a rough boundary—Extensions of the Kirchhoff approximation,” *J. Acoust. Soc. Am.*, vol. 71, no. 5, pp. 1093–1100, 1982.
- [96] P. Beckmann, “Scattering by non-Gaussian surfaces,” *IEEE Trans. Antennas Propag.*, vol. AP-21, no. 2, pp. 169–175, 1973.

- [97] F. Henyey and D. Wurmser, “Acoustic scattering from a non-Gaussian ocean surface,” *J. Acoust. Soc. Am.*, vol. 87, no. 6, pp. 2477–2480, 1990.
- [98] D. Barrick, “Rough surface scattering based on the specular point theory,” *IEEE Trans. Antennas Propag.*, vol. AP-16, no. 4, pp. 449–454, 1968.
- [99] R. Wagner, “Shadowing of randomly rough surfaces,” *J. Acoust. Soc. Am.*, vol. 41, no. 1, pp. 138–147, 1967.
- [100] P. Lynch, “Curvature corrections to rough-surface scattering at high frequencies,” *J. Acoust. Soc. Am.*, vol. 47, no. 3, pp. 804–815, 1970.
- [101] E. Thorsos, “The validity of the Kirchhoff approximation for rough surface scattering using a Gaussian roughness spectrum,” *J. Acoust. Soc. Am.*, vol. 83, no. 1, pp. 78–92, 1988.
- [102] B. Kur’yanov, “The scattering of sound at a rough surface with two types of irregularity,” *Sov. Phys. Acoust.*, vol. 8, pp. 252–257, 1963.
- [103] S. McDaniel and A. Gorman, “An examination of the composite-roughness scattering model,” *J. Acoust. Soc. Am.*, vol. 73, no. 5, pp. 1476–1486, 1983.
- [104] A. Voronovich, “Small-slope approximation in wave scattering by rough surfaces,” *Sov. Phys. JETP*, vol. 62, no. 1, pp. 65–70, 1985.

- [105] A. Voronovich, *Wave Scattering from Rough Surfaces*. Springer-Verlag, Berlin, second ed., 1999.
- [106] E. Thorsos and S. Broschat, “An investigation of the small slope approximation for scattering from rough surfaces. Part I. Theory,” *J. Acoust. Soc. Am.*, vol. 97, no. 4, pp. 2082–2093, 1995.
- [107] S. Broschat and E. Thorsos, “An investigation of the small slope approximation for scattering from rough surfaces. Part II. Numerical studies,” *J. Acoust. Soc. Am.*, vol. 101, no. 5, pp. 2615–2625, 1997.
- [108] J. Miles, “On nonspecular reflection at a rough surface,” *J. Acoust. Soc. Am.*, vol. 26, no. 2, pp. 191–199, 1954.
- [109] E. Kuo, “Wave scattering and transmission at irregular surfaces,” *J. Acoust. Soc. Am.*, vol. 36, no. 11, pp. 2135–2142, 1964.
- [110] C. Clay, “Coherent reflection of sound from the ocean bottom,” *J. Geophys. Res.*, vol. 71, no. 8, pp. 2037–2046, 1966.
- [111] C. Clay, H. Medwin, and W. Wright, “Specularly scattered sound and the probability density function of a rough surface,” *J. Acoust. Soc. Am.*, vol. 53, no. 6, pp. 1677–1682, 1973.
- [112] W. Kuperman, “Specularly scattered sound and the probability density function of a rough surface,” *J. Acoust. Soc. Am.*, vol. 58, no. 2, pp. 365–370, 1975.

- [113] D. Jackson, D. Winebrenner, and A. Ishimaru, "Application of the composite roughness model to high-frequency bottom backscattering," *J. Acoust. Soc. Am.*, vol. 79, no. 5, pp. 1410–1422, 1986.
- [114] P. Mourad and D. Jackson, "High frequency sonar equation models for bottom backscatter and forward loss," *Proceedings OCEANS*, vol. 4, pp. 1168–1175, 1989.
- [115] K. Williams and D. Jackson, "Bistatic bottom scattering: Model, experiments and model/data comparison," *J. Acoust. Soc. Am.*, vol. 103, no. 1, pp. 169–181, 1998.
- [116] D. Dacol and D. Berman, "Sound scattering from a randomly rough fluid-solid interface," *J. Acoust. Soc. Am.*, vol. 84, no. 1, pp. 292–302, 1988.
- [117] D. Jackson and A. Ivakin, "Scattering from elastic sea beds: First-order theory," *J. Acoust. Soc. Am.*, vol. 103, no. 1, pp. 336–345, 1998.
- [118] D. Dacol, "The Kirchhoff approximation for acoustic scattering from a rough fluid-elastic solid interface," *J. Acoust. Soc. Am.*, vol. 88, no. 2, pp. 978–983, 1990.
- [119] D. Berman, "Simulations of rough interface scattering," *J. Acoust. Soc. Am.*, vol. 89, no. 2, pp. 623–636, 1991.

- [120] T. Yang and S. Broschat, “Acoustic scattering from a fluid-elastic solid interface using the small slope approximation,” *J. Acoust. Soc. Am.*, vol. 96, no. 3, pp. 1796–1804, 1994.
- [121] R. Gragg, D. Wurmser, and R. Gauss, “Small-slope scattering from rough elastic ocean floors: General theory and computational algorithm,” *J. Acoust. Soc. Am.*, vol. 110, no. 6, pp. 2878–2901, 2001.
- [122] E. Kuo, “Acoustic wave scattering from two solid boundaries at the ocean bottom: Reflection loss,” *IEEE J. Ocean Eng.*, vol. 17, no. 1, pp. 159–170, 1992.
- [123] S. McDaniel, “Effect of surficial sediment layering on high-frequency seafloor reverberation,” *J. Acoust. Soc. Am.*, vol. 91, no. 3, pp. 1353–1356, 1992.
- [124] H.-H. Essen, “Scattering from a rough sedimental seafloor containing shear and layering,” *J. Acoust. Soc. Am.*, vol. 95, no. 3, pp. 1299–1310, 1994.
- [125] A. Lyons, A. Anderson, and F. Dwan, “Acoustic scattering from the seafloor: Modeling and data comparison,” *J. Acoust. Soc. Am.*, vol. 95, no. 5, pp. 2441–2451, 1994.
- [126] J. Moe and D. Jackson, “First-order perturbation solution for rough surface scattering cross section including the effects of gradients,” *J. Acoust. Soc. Am.*, vol. 96, no. 3, pp. 1748–1754, 1994.

- [127] W. Kuperman and H. Schmidt, “Rough surface elastic wave scattering in a horizontally stratified ocean,” *J. Acoust. Soc. Am.*, vol. 79, no. 6, pp. 1767–1777, 1986.
- [128] D. Tang, “A note on scattering by a stack of rough interfaces,” *J. Acoust. Soc. Am.*, vol. 99, no. 3, pp. 1414–1418, 1996.
- [129] A. Ivakin, “A unified approach to volume and roughness scattering,” *J. Acoust. Soc. Am.*, vol. 103, no. 2, pp. 827–837, 1998.
- [130] D. Jackson, R. Odom, M. Boyd, and A. Ivakin, “A geacoustic bottom interaction model (GABIM),” *IEEE J. Ocean Eng.*, vol. 35, no. 3, pp. 603–617, 2010.
- [131] D. Jackson, “The small-slope approximation for layered seabeds,” *Proceedings of Meetings on Acoustics*, vol. 19, p. 070001, 2013.
- [132] S. Stanic, K. Briggs, P. Fleischer, R. Ray, and W. Sawyer, “Shallow-water high-frequency bottom scattering off Panama City, Florida,” *J. Acoust. Soc. Am.*, vol. 83, no. 6, pp. 2134–2144, 1988.
- [133] S. Stanic, K. Briggs, P. Fleischer, W. Sawyer, and R. Ray, “High-frequency acoustic backscattering from a coarse shell ocean bottom,” *J. Acoust. Soc. Am.*, vol. 85, no. 1, pp. 125–136, 1989.
- [134] E. Pouliquen and A. Lyons, “Backscattering from bioturbated sediments at very high frequency,” *IEEE J. Ocean Eng.*, vol. 27, no. 3, pp. 388–402, 2002.

- [135] D. Jackson and K. Briggs, “High-frequency bottom backscattering: Roughness versus sediment volume scattering,” *J. Acoust. Soc. Am.*, vol. 92, no. 2, pp. 962–977, 1992.
- [136] D. Jackson, K. Briggs, K. Williams, and M. Richardson, “Tests of models for high-frequency seafloor backscatter,” *IEEE J. Ocean Eng.*, vol. 21, no. 4, pp. 458–470, 1996.
- [137] K. Briggs, K. Williams, D. Jackson, C. Jones, A. Ivakin, and T. Orsi, “Fine-scale sedimentary structure: implications for acoustic remote sensing,” *Marine Geology*, vol. 182, pp. 141–159, 2002.
- [138] P. Thorne and N. Pace, “Acoustic studies of broadband scattering from a model rough surface,” *J. Acoust. Soc. Am.*, vol. 75, no. 1, pp. 133–144, 1984.
- [139] P. Thorne, N. Pace, and Z. Al-Hamdani, “Laboratory measurements of backscattering from marine sediments,” *J. Acoust. Soc. Am.*, vol. 84, no. 1, pp. 303–309, 1988.
- [140] C. de Moustier and D. Alexandrou, “Angular dependence of 12-kHz seafloor acoustic backscatter,” *J. Acoust. Soc. Am.*, vol. 90, no. 1, pp. 522–531, 1991.
- [141] R. Soukup and R. Gragg, “Backscatter from a limestone seafloor at 2-3.5 kHz: Measurements and modeling,” *J. Acoust. Soc. Am.*, vol. 113, no. 5, pp. 2501–2514, 2003.



- [142] R. Altenburg, N. Chotiros, and C. Faulkner, “Plane-wave analysis of acoustic signals in a sandy sediment,” *J. Acoust. Soc. Am.*, vol. 89, no. 1, pp. 165–170, 1991.
- [143] N. Chotiros, A. Mautner, A. Løvik, Å. Kristensen, and O. Bergem, “Acoustic penetration of a silty sand sediment in the 1-10-kHz band,” *IEEE J. Ocean Eng.*, vol. 2, no. 4, pp. 604–615, 1997.
- [144] N. Chotiros, “Biot model of sound propagation in water-saturated sand,” *J. Acoust. Soc. Am.*, vol. 97, no. 1, pp. 199–214, 1995.
- [145] R. Stoll, “Comments on ‘Biot model of sound propagation in water-saturated sand’,” *J. Acoust. Soc. Am.*, vol. 103, no. 5, pp. 2723–2725, 1998.
- [146] E. Pouliquen, A. Lyons, and N. Pace, “Penetration of acoustic waves into rippled sandy seafloors,” *J. Acoust. Soc. Am.*, vol. 108, no. 5, pp. 2071–2081, 2000.
- [147] A. Maguer, W. Fox, H. Schmidt, E. Pouliquen, and E. Bovio, “Mechanisms for subcritical penetration into a sandy bottom: Experimental and modeling results,” *J. Acoust. Soc. Am.*, vol. 107, no. 3, pp. 1215–1225, 2000.
- [148] H. Simpson and B. Houston, “Synthetic array measurements of acoustical waves propagating into a water-saturated sandy bottom for a smoothed

- and roughened surface,” *J. Acoust. Soc. Am.*, vol. 107, no. 5, pp. 2329–2337, 2000.
- [149] R. Lim, I. Paustian, and J. Lopes, “Acoustic transmission across a roughened fluid-fluid interface,” *J. Acoust. Soc. Am.*, vol. 109, no. 4, pp. 1367–1382, 2001.
- [150] E. Thorsos, K. Williams, N. Chotiros, J. Christoff, K. Commander, C. Greenlaw, D. Holliday, D. Jackson, J. Lopes, D. McGehee, J. Piper, M. Richardson, and D. Tang, “An overview of SAX99: Acoustic measurements,” *IEEE J. Ocean Eng.*, vol. 26, no. 1, pp. 4–25, 2001.
- [151] D. Jackson, K. Williams, E. Thorsos, and S. Kargl, “High-frequency subcritical acoustic penetration into a sandy sediment,” *IEEE J. Ocean Eng.*, vol. 27, no. 3, pp. 346–361, 2002.
- [152] N. Chotiros, D. Smith, and J. Piper, “Refraction and scattering into a sandy ocean sediment in the 30-40-kHz band,” *IEEE J. Ocean Eng.*, vol. 27, no. 3, pp. 362–375, 2002.
- [153] H. Deresiewicz and B. Wolf, “The effect of boundaries on wave propagation in a liquid-filled porous solid: VIII. Reflection of planewaves at an irregular boundary,” *Bull. Seis. Am.*, vol. 54, no. 5A, pp. 1537–1561, 1964.
- [154] A. Ivakin, “Sound scattering by inhomogeneities of an elastic half-space,” *Sov. Phys. Acoust.*, vol. 36, no. 4, pp. 377–380, 1990.

- [155] S. Stanic, R. Goodman, K. Briggs, N. Chotiros, and E. Kennedy, “Shallow-water bottom reverberation measurements,” *IEEE J. Ocean Eng.*, vol. 23, no. 3, pp. 203–210, 1998.
- [156] F. Boyle and N. Chotiros, “A model for high-frequency acoustic backscatter from gas bubbles in sandy sediments at shallow grazing angles,” *J. Acoust. Soc. Am.*, vol. 98, no. 1, pp. 531–541, 1995.
- [157] F. Boyle and N. Chotiros, “Bottom Grain Gas and Roughness Technique (BOGGART) Version 3.0: Bottom Backscatter Model User’s Guide,” Tech. Rep. ARL-TR-96-10, Applied Research Laboratories, The University of Texas at Austin, 1996.
- [158] N. Chotiros, “High frequency bottom backscattering strength at shallow grazing angles,” in *Underwater Acoustic Measurements: Technologies and Results, 4th International Conference*, pp. 1699–1676, 2011.
- [159] K. Briggs, A. Reed, D. Jackson, and D. Tang, “File-scale volume heterogeneity in a mixed sand/mud sediment off Fort Walton Beach, FL,” *IEEE J. Ocean Eng.*, vol. 35, no. 3, pp. 471–487, 2010.
- [160] K. Williams, D. Jackson, D. Tang, K. Briggs, and E. Thorsos, “Acoustic backscattering from a sand and a sand/mud environment: Experiments and data/model comparisons,” *IEEE J. Ocean Eng.*, vol. 34, no. 4, pp. 388–398, 2009.

- [161] A. Ivakin, “Scattering from Inclusions in Marine Sediments: SAX04 Data/Model Comparisons,” Tech. Rep., Applied Physics Laboratory, University of Washington, 2008.
- [162] K. Williams, “Forward scattering from a rippled sand/water interface: modeling, measurements, and determination of the plane wave, flat surface reflection coefficient,” *IEEE J. Ocean Eng.*, vol. 34, no. 4, pp. 399–406, 2009.
- [163] E. Becker, G. Carey, and J. Oden, *Finite Elements: An Introduction, Volume I*. Prentice-Hall, Englewood Cliffs, NJ, 1981.
- [164] Y. Kang and J. Bolton, “Finite element modeling of isotropic elastic porous materials coupled with acoustical finite elements,” *J. Acoust. Soc. Am.*, vol. 98, no. 1, pp. 635–643, 1995.
- [165] R. Panneton and N. Atalla, “An efficient finite element scheme for solving the three-dimensional poroelasticity problem in acoustics,” *J. Acoust. Soc. Am.*, vol. 101, no. 6, pp. 2387–2398, 1997.
- [166] Y. Kang, B. Gardner, and J. Bolton, “An axisymmetric poroelastic finite element formulation,” *J. Acoust. Soc. Am.*, vol. 106, no. 2, pp. 565–574, 1999.
- [167] D. Dauchez, S. Sahraoui, and N. Atalla, “Convergence of poroelastic finite elements based on Biot displacement formulation,” *J. Acoust. Soc. Am.*, vol. 109, no. 1, pp. 33–40, 2001.

- [168] P. Debergue, R. Panneton, and N. Atalla, “Boundary conditions for the weak formulation of the mixed (u,p) poroelasticity problem,” *J. Acoust. Soc. Am.*, vol. 106, no. 5, pp. 2383–2390, 1999.
- [169] N. Atalla, M. Hamdi, and R. Panneton, “Enhanced weak integral formulation for the mixed (u,p) poroelastic equations,” *J. Acoust. Soc. Am.*, vol. 109, no. 6, pp. 3065–3068, 2001.
- [170] S. Lou, L. Tsang, C. Chan, and A. Ishimaru, “Monte Carlo simulation of scattering of waves by a random rough surface with the finite element method and the finite difference method,” *Microw. Opt. Techn. Let.*, vol. 3, no. 5, pp. 150–154, 1990.
- [171] K. Krause, S. Lou, L. Tsang, and C. Chan, “Application of the finite element method to Monte Carlo simulation of random rough surface scattering with Neumann boundary conditions,” *Microw. Opt. Techn. Let.*, vol. 4, no. 7, pp. 255–258, 1991.
- [172] S. Lou, L. Tsang, and C. Chan, “Application of the finite element method to Monte Carlo simulations of scattering of waves by random rough surfaces: penetrable case,” *Wave Random Media*, vol. 1, no. 4, pp. 287–307, 1991.
- [173] M. Isakson, R. Yarbrough, and N. Chotiros, “A finite element model for seafloor roughness scattering,” in *Proceeding of the International Symposium on Underwater Reverberation and Clutter*, pp. 173–180, 2008.

- [174] J.-P. Bérenger, “A perfectly matched layer for the absorption of electromagnetic waves,” *J. Comp. Phys.*, vol. 114, pp. 185–200, 1994.
- [175] S. Joshi, “Quantifying three dimensional effects in acoustic rough surface scattering,” Master’s thesis, The University of Texas at Austin, 2011.
- [176] B. Tran, “Three transdimensional factors for the conversion of 2D acoustic rough surface scattering model results for comparison with 3D scattering,” Master’s thesis, The University of Texas at Austin, 2013.
- [177] M. Isakson and N. Chotiros, “Finite element modeling of acoustic scattering from fluid and elastic rough interfaces (accepted for publication),” *IEEE J. Ocean Eng.*, 2014.
- [178] J. Carcione, *Wave Fields in Real Media: Wave Propagation in Anisotropic Anelastic, Porous and Electromagnetic Media*. Elsevier, Oxford, England, 2007.
- [179] M. Abramowitz and I. Stegun, eds., *Handbook of Mathematical Functions*. Dover, New York, 1965.
- [180] COMSOL AB, *COMSOL v4.3b Acoustics Module: User’s Guide*, May 2013.
- [181] K. Graff, *Wave Motion in Elastic Solids*. Dover, New York, 1975.
- [182] D. Blackstock, *Fundamentals of Physical Acoustics*. John Wiley & Sons, New York, 2000.

- [183] J. Reddy, *Applied Functional Analysis and Variational Methods in Engineering*. McGraw-Hill, New York, 1986.
- [184] F. Ihlenburg, *Finite Element Analysis of Acoustic Scattering*. Springer-Verlag, New York, 1998.
- [185] O. Zienkiewicz and Y. Cheung, *The Finite Element Method in Structural and Continuum Mechanics*. McGraw-Hill, London, 1967.
- [186] A. Bermúdez, L. Hervella-Nieto, A. Prieto, and R. Rodríguez, “An optimal perfectly matched layer with unbounded absorbing function for time-harmonic acoustic scattering problems,” *J. Comp. Phys.*, vol. 223, pp. 469–488, 2006.
- [187] M. Zampolli, A. Tesei, F. Jensen, N. Malm, and J. B. III, “A computationally efficient finite element model with perfectly matched layers applied to scattering from axially symmetric objects,” *J. Acoust. Soc. Am.*, vol. 122, no. 3, pp. 1472–1485, 2007.
- [188] W. Chew and Q. Liu, “Perfectly matched layers for elastodynamics: A new absorbing boundary condition,” *J. Comp. Acoust.*, vol. 4, no. 4, pp. 341–359, 1996.
- [189] Y. Zeng, J. He, and Q. Liu, “The application of the perfectly matched layer in numerical modeling of wave propagation in poroelastic media,” *Geophysics*, vol. 66, no. 4, pp. 1258–1266, 2001.

- [190] J. Toporkov, R. Awadallah, and G. Brown, “Issues related to the use of a Gaussian-like incident field for low-grazing-angle scattering,” *J. Opt. Soc. Am. A*, vol. 16, no. 1, pp. 176–187, 1999.
- [191] F. Jensen, W. Kuperman, M. Porter, and H. Schmidt, *Computational Ocean Acoustics*. AIP Press, Woodbury, NY, 1994.
- [192] L. Brekhovskikh, *Waves in Layered Media*. Academic Press, New York, 2nd ed., 1980.
- [193] D. Ross, *Mechanics of Underwater Noise*. Pergamon Press, New York, 1976.
- [194] A. Ishimaru, *Wave Propagation and Scattering in Random Media, Volume 2*. Academic Press, New York, 1978.
- [195] A. Ishimaru, *Wave Propagation and Scattering in Random Media, Volume 1*. Academic Press, New York, 1978.
- [196] H. Haslach, Jr. and R. Armstrong, *Deformable Bodies and Their Material Behavior*. John Wiley & Sons, Hoboken, NJ, 2004.
- [197] E. Skudrzyk, *The Foundation of Acoustics*. Springer-Verlag, Wien, 1971.
- [198] L. Beranek, *Acoustics*. Acoustical Society of America, Woodbury, NY, 1993 ed. ed., 1996.



- [199] P. Morse and K. U. Ingard, *Theoretical Acoustics*. Princeton University Press, Princeton, NJ, 1986.
- [200] A. Pierce, *Acoustics*. Acoustical Society of America, Melville, NY, 1989.

## Vita

Anthony Lucas Bonomo is originally from Hamilton Square, NJ, where he graduated salutatorian from Steinert High School in 2007. He went on to complete his undergraduate education at the University of Maryland, College Park, graduating Cum Laude with bachelor's degrees in both Mechanical Engineering and Jazz Studies in 2012. While at UMCP, Anthony also participated in the Gemstone program, a multidisciplinary four-year research program for selected undergraduate honors students of all majors. Anthony is now a graduate student at The University of Texas at Austin, where he just completed a Master's of Science in Mechanical Engineering. He is also a graduate research assistant at the Applied Research Laboratories studying underwater acoustics. His master's degree was partially funded by the SMART scholarship program, a fellowship program sponsored by the American Society for Engineering Education and the Department of Defense.

Permanent address: 2211 W North Loop Blvd, Apt 124  
Austin, Texas 78756

This thesis was typeset with L<sup>A</sup>T<sub>E</sub>X<sup>†</sup> by the author.

---

<sup>†</sup>L<sup>A</sup>T<sub>E</sub>X is a document preparation system developed by Leslie Lamport as a special version of Donald Knuth's T<sub>E</sub>X Program.